

Andreas Windischbacher, BSc

**Application of Density-Functional-Theory  
for the Simulation of Structural and Electronic Properties  
of Metal Organic Frameworks**

**MASTER'S THESIS**

to achieve the university degree of

Master of Science

Master's degree programme: Chemistry

submitted to

**Graz University of Technology**

Supervisor

Ao.Univ.-Prof. Dipl.-Ing. Dr.techn. Anne-Marie Kelterer

Institute of Physical and Theoretical Chemistry

Second supervisor: Ao.Univ.-Prof. Dipl.-Ing. Dr.techn. Egbert Zojer  
Institute of Solid State Physics

## **AFFIDAVIT**

I declare that I have authored this thesis independently, that I have not used other than the declared sources/resources, and that I have explicitly indicated all material which has been quoted either literally or by content from the sources used. The text document uploaded to TUGRAZonline is identical to the present master's thesis.

---

Date

---

Signature

## Abstract

Over the past decade metal organic frameworks (MOFs) found numerous applications ranging from classical catalysis to biomedical drug delivery systems. Their common structural elements are metal clusters, so called secondary building units, connected by organic linkers forming a 3D framework. In the wide variety of metal organic frameworks, this thesis deals with a copper-MOF and a zinc-MOF consisting of similar paddle-wheel like secondary building units.

The aim of the thesis is to provide first computational insight into newly synthesized MOFs by applying Density Functional Theory (DFT). Despite their structural relation, the assemblies were investigated for very different reasons.

The first part of the thesis covers periodic DFT calculations of a Cu-MOF to explain its heteroepitaxial growth on a  $\text{Cu}(\text{OH})_2$  substrate. For this, the bulk structure as well as the interface to the substrate was simulated. The description of the antiferromagnetic singlet state of the Cu-MOF as a triplet was validated with molecular calculations.

The fully relaxed bulk structure of the MOF deviates significantly from the experimental unit cell implying strong influences during synthesis, which enforce epitaxial growth. A possible cause of such forces could be the formation of a rigid self-assembling monolayer. However, a deeper explanation is subject to further studies.

In the second part of the thesis, the direction-dependency of Förster resonance energy transfer between anthracene-dibenzoic acid linkers (ADB) of a Zn-MOF was investigated. For a better understanding of the hopping between single ADB units, an approach was chosen combining periodic and molecular DFT calculations. Oligomers were built modelling the periodic arrangement. It could be shown that the central monomer of a trimer resembles the periodic geometry, hence, trimers were optimized in the ground and first excited state. The central unit was extracted and the transition density for absorption and emission of a monomer was obtained by time-dependent DFT calculations. Applying the Transition-density Cube method, the Coulomb coupling between two monomers was calculated along different directions in the periodic structure as a measure for the Förster rate.

The Coulomb coupling was found to have significant anisotropic behaviour along the inter-sheet direction. Experimentally, two distinct transfer rates are found. Therefore, several explanations beyond Förster theory are presented based on excimer formation or two different MOF phases.

## Kurzfassung

Im letzten Jahrzehnt haben sich die Anwendungen von metallorganischen Gerüstverbindungen (engl. kurz: MOFs) über die klassische Katalyse bis hin zu medizinischen Wirkstoffspeichern ausgebreitet. Die Gemeinsamkeit aller Strukturen sind Metallcluster, sogenannte sekundäre Baueinheiten, die durch organische Moleküle zu einem dreidimensionalen Netzwerk verbunden sind. Aus der großen Anzahl von MOFs wurden in dieser Arbeit eine Kupfer-Verbindung und eine Zink-Verbindung näher untersucht, die beide aus Schaufelrad-ähnlichen, sekundären Baueinheiten bestehen.

Das Ziel dieser Arbeit ist die theoretische Beschreibung von kürzlich synthetisierten MOF-Strukturen und deren elektronischen Eigenschaften. Dabei wurden zwei unterschiedliche Fragestellungen mittels Dichtefunktionaltheorie (DFT) behandelt.

Der erste Teil der Arbeit beschäftigt sich mit periodischen DFT-Berechnungen eines Cu-MOFs zur Erklärung seines heteroepitaktischen Wachstums auf einem  $\text{Cu}(\text{OH})_2$  Substrat. Hierzu wurde die periodische Grundstruktur als auch die Grenzfläche zum Substrat simuliert. Die Beschreibung des antiferromagnetischen Singulett Zustands der Cu-Baueinheit als Triplett wird anhand von quantenchemischen Molekülrechnungen gezeigt.

Die optimierte, periodische Struktur des Cu-MOFs unterscheidet sich signifikant von der experimentell vorgeschlagenen Einheitszelle. Dies deutet auf starke Einflüsse während der Synthese hin, die eine Epitaxie erzwingen. Eben solche Kräfte könnten beispielsweise durch die Bildung einer selbstorganisierenden Monoschicht zustande kommen. Tiefere Einblicke in diese Epitaxie bedürfen weiterer Untersuchungen.

Im zweiten Teil der Arbeit wird der richtungsabhängige Förster-Resonanz-Energie-Transfer zwischen den Anthrazen-Dibenzoesäure-Einheiten (ADB) eines Zn-MOF untersucht. Für ein besseres Verständnis des Energie-Transfers zwischen einzelnen Molekülen werden periodische und quantenchemische DFT Rechnungen kombiniert. Gemäß der periodischen Anordnung werden Oligomere aus organischen Molekülen und Zn-Clustern gebaut. Es zeigt sich, dass das zentrale Monomer einer Trimereinheit die periodische Geometrie annimmt. Aus diesem Grund wurden Trimere für die Optimierung des Grundzustandes und des ersten angeregten Zustandes verwendet. Die mittlere Einheit wurde ausgeschnitten und die Übergangsdichte von einem Monomer für Absorption und Emission mit zeitabhängiger DFT berechnet. Mithilfe der Transition-Density Cube Methode wurde die Coulomb-Kopplung in verschiedene Richtungen als Maß für die Förster Rate bestimmt.

Die Coulomb-Kopplung zeigt eine signifikante Anisotropie. Experimentell wurden zwei unterschiedliche Förster-Raten gemessen. Aus diesem Grund werden Möglichkeiten diskutiert, die das Auftreten zweier Raten erklären, wie zum Beispiel Excimer-Bildung oder Ausbildung zweier MOF-Phasen.

## **Acknowledgments**

First and foremost, I want to thank my supervisor Anne-Marie Kelterer for the opportunity to write this thesis and for her guidance along the way. Her scientific competence and patience made this work possible, and her down-to-earth nature created an enjoyable work environment.

I would also like to express my deepest gratitude to Egbert Zojer, who introduced me to a new world of scientific working and powerpoint presentations. His experience and knowledge were crucial for this work.

Many thanks to the members of the Advanced Materials Modelling group. I admire their passion and dedication to their work, and their conscientiousness made a strong impact on me. At this point I have to especially thank Giulia for all the unproductive discussions about baroque music and other, somewhat less baroque, topics.

Special thanks to all those who leave the office early.

## Content

<b>Abstract</b>	<b>i</b>
<b>Kurzfassung</b>	<b>ii</b>
<b>Acknowledgments</b>	<b>iii</b>
<b>Content</b>	<b>iv</b>
<b>1 Introduction</b>	<b>1</b>
<b>2 Metal-Organic Frameworks</b>	<b>2</b>
<b>3 Förster Theory</b>	<b>6</b>
3.1 Transition Density .....	8
3.2 Ideal Dipole Approximation (IDA) .....	9
3.3 Transition Density Cube Method (TDC).....	10
<b>4 Theoretical Methods</b>	<b>11</b>
4.1 Density Functional Theory .....	11
4.2 Exchange-correlation Approximations .....	13
4.3 Time-dependent Density Functional Theory .....	14
4.4 Basis Set.....	15
4.5 Van der Waals Correction.....	16
<b>5 Epitaxial Growth of a Cu-MOF</b>	<b>17</b>
5.1 Background and Motivation.....	17
5.2 Computational Details .....	19
5.2.1 Molecular calculations.....	19
5.2.2 Benchmarking of the spin state .....	19
5.2.3 Periodic calculations .....	21
5.3 Results and Discussion.....	23
5.3.1 MOF bulk.....	23
5.3.2 The substrate .....	25
5.3.3 Substrate and MOF.....	26

<b>6</b>	<b>FRET in a Zn-SURMOF</b>	<b>30</b>
6.1	Background and Motivation.....	30
6.2	Computational Details .....	32
6.2.1	Molecular calculations.....	32
6.2.2	Workflow for the calculation of FRET in MOFs.....	32
6.2.3	Periodic calculations .....	34
6.2.4	Oligomer calculations .....	34
6.2.5	Monomer calculations .....	34
6.2.6	Benchmarking of the functional .....	35
6.2.7	Benchmarking of the basis set .....	35
6.3	Results and Discussion.....	39
6.3.1	Molecular simulations.....	39
6.3.2	Absorption and emission of ADB molecule.....	40
6.3.3	Periodic simulations .....	43
6.3.4	Importance of adjacent linkers .....	46
6.3.5	Cluster approach.....	47
6.3.6	Monomer hopping .....	54
6.3.7	Model system anthracene .....	56
6.3.8	Beyond simple hopping.....	58
<b>7</b>	<b>Conclusion</b>	<b>75</b>
<b>8</b>	<b>Appendix</b>	<b>77</b>
A1	Excitation Analysis .....	77
A1.1	Benchmarking .....	77
A1.2	Molecular excitation properties.....	79
A1.3	Quinoid structure.....	81
A2	FRET Code.....	82
A2.1	The input file.....	82
A2.2	Convergence testing .....	83
A2.3	TDC vs. IDA .....	86
A3	FHI-Aims basis set.....	87
	<b>Bibliography</b>	<b>88</b>

# 1 Introduction

The star of metal-organic frameworks rose in the 1990s and experienced an exponential increase of interest since then. Their structural diversity opens the door to a variety of properties, ranging from absorption and transport of small molecules to light harvesting and catalysis. Oriented towards industry, scientists strive for high-end applications easy to make. These can already be found ranging from alternative fuel storage to biomedical technology and represent the first step into a new era of more sophisticated materials.

Profound knowledge of the behaviour of the individual components is the key to successful development. Computational modelling may serve as a useful tool here. Designing structures virtually provides insight into existing materials while at the same time also allows for predictions about new ones.

The goal of this thesis is to combine quantum chemistry and solid-state knowledge to investigate different properties of metal organic frameworks. For clarity, this thesis is divided into two parts. Each part can be understood as an independent topic and is based upon a research publication from our collaborators.

The first part is particularly dedicated to the structure and formation of a recently synthesised Cu-MOF. It is grown heteroepitaxially by consuming its  $\text{Cu}(\text{OH})_2$  substrate. The thesis aims to contribute to the better understanding of this specific epitaxial synthesis approach.

The second part is mainly about the electronic properties of a light-harvesting Zn-MOF system. MOFs make up an interesting group for examining energy transport as their 3D structure keeps the organic chromophores in defined positions. In experiment, this shows itself in an anisotropic energy transfer. The calculations try to provide deeper insight into Förster resonance energy transfer between the organic linkers.

The thesis is structured as follows: After the general introduction (chapter 1) follows the introduction into the main topics of this thesis. Chapter 2 covers the coordination chemistry of copper and zinc containing metal-organic frameworks and chapter 3 the basic ideas of Förster theory. A short overview of density functional theory is given in the theoretical methods (chapter 4). Chapter 5 shows the results of the calculations on epitaxial growth of a Cu-MOF. In chapter 6, the results about Förster resonance energy transfer in a Zn-SURMOF are summarized. A general conclusion about both research projects is given in chapter 7.



## 2 Metal-Organic Frameworks

Metal-organic frameworks (MOFs) are porous materials extending in one to three dimensions, which derive their name from their main components: metal ions and organic molecules. The inorganic ions form polynuclear clusters named secondary building units (SBUs), which are linked together by their organic ligands.<sup>1</sup> In contrast to the commonly known weakly coordinated bond of Lewis acid-base character, the bonding in MOFs usually involves negatively charged organic molecules, such as carboxylates or imidazolates together with the positively charged metal ions. A salt-like interaction between the linkers and the metal ions plays an important role in the permanent stability of the network also without guest molecules.<sup>2</sup> Depending on the type of the metal and its ligands, a great variety of geometries can be synthesized, allowing for numerous applications. Due to the porosity of the network, the obvious choice of application is to make use of the high surface area. Guest molecules can be directly incorporated during synthesis or diffuse into the bulk structure depending selectively on the pore size of the MOF.<sup>3</sup> Thus, these materials are predestined for gas absorption,<sup>4,5</sup> drug delivery<sup>6,7</sup> or catalysis.<sup>8,9</sup> But also the chemical properties of the building blocks themselves led to promising results in light-harvesting<sup>10,11,12</sup> or sensing applications.<sup>13,14</sup> Postsynthetic modification of the linkers enhances the possible research fields even further.<sup>15</sup> However, despite the scientific euphoria, it should be noted that resounding industrial success is currently limited by the chemical long-term instability of many MOF-structures.<sup>15</sup>

A prominent SBU is the so-called square paddle-wheel which consists of two metal ions bridged by four carboxylates in syn-syn mode as shown in Figure 1. The paddle-wheel has proven to be an interesting building block, most commonly used in copper or zinc clusters.<sup>2,16</sup>

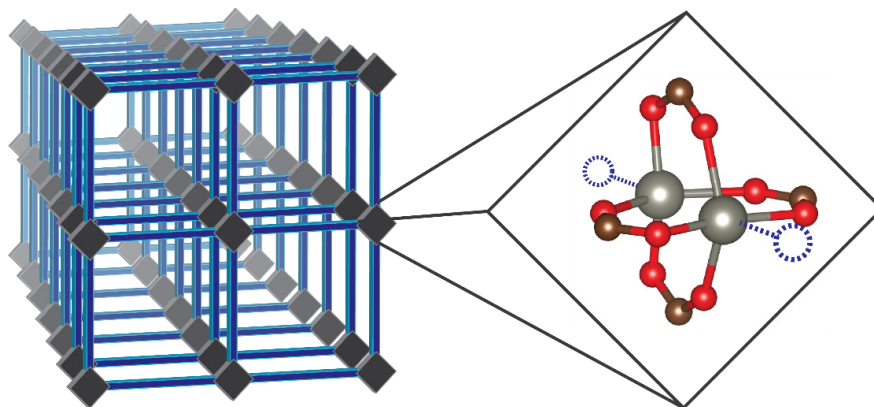


Figure 1: Schematic representation of a MOF with a square paddle-wheel SBU with four carboxylates in basal position, the apical positions are shown with dotted balls.

As can be seen in Figure 1, two coordination positions (basal and apical) can be distinguished in this SBU. Acting as four-connecting structural fragment with carboxylates in basal position, it forms two-dimensional layered structures. Additionally, the apical position can be occupied either by pillaring ligands or solvent molecules, both influencing the framework. For instance, experiments suggest that solvents with suitable heteroatoms favour the coordination to apical positions in paddle-wheel units substantially stabilizing the MOF.<sup>17</sup>

To get a better structural understanding of SBUs, the  $\text{Cu}^{2+}$  and  $\text{Zn}^{2+}$  clusters are described from the simplified point of view of Crystal Field Theory (CFT). In CFT, the ligands surrounding the central ion are considered as point charges fixed on defined spatial positions.<sup>18</sup> The interaction of the negative point charges with the d-orbitals of the central transition metal ion leads to orbital splitting characteristic for specific coordination polyhedra. In the first instance, the arrangement of four ligands may correspond to an electric field with tetrahedral or square-planar symmetry.

In a tetrahedral coordination sphere, it is evident that orbitals which extend into the space between the axis ( $d_{xy}$ ,  $d_{xz}$ ,  $d_{yz}$ ) are less favourable as they point directly towards the negatively charged ligands. On the other hand, orbitals which extend along the axis ( $d_{x^2-y^2}$ ,  $d_{z^2}$ ) are favoured. The square-planar splitting is somewhat more complex to derive from scratch but can best be imagined by elongation of an octahedra along the z-axis. This distortion results in an energy-lowering of orbitals pointing in the z-axis and an increase for the rest. Figure 2 shows the tetrahedral and the square planar splitting in reference to the five-fold degenerated d-orbitals of an ion placed into an isotropic space without external field. The energy of the free ion is set to zero, the relative energy is given in units of  $\Delta_0$ .<sup>18</sup>

In the case of  $\text{Cu}^{2+}$ , nine electrons have to be filled into the five d-orbitals. According to Figure 2, it is energetically more stable for the complex to adopt a square-planar arrangement than a tetrahedral one. However, as seen in Werner-complexes like  $[\text{Cu}(\text{NH}_3)_4]^{2+}$ , the apical positions are often coordinated to solvent molecules resulting in a Jahn-Teller distorted octahedral or square pyramidal symmetry.<sup>19</sup> In both cases the orbital splitting looks the same, similar to the square-planar case, except a less pronounced splitting as depicted in Figure 2. Square pyramidal is therefore even more favourable than square-planar as less energy is required to take the single electron into the  $d_{x^2-y^2}$  orbital. In the world of SBUs, this expresses itself in a widespread arrangement, in which the oxygen atoms of the carboxylate on a paddle-wheel bridge to a metal ion of the other paddle-

wheel like a cap.<sup>16,20,21</sup> Moreover, we can now also understand the stabilization of the paddle-wheel upon increasing its connectivity as mentioned earlier.

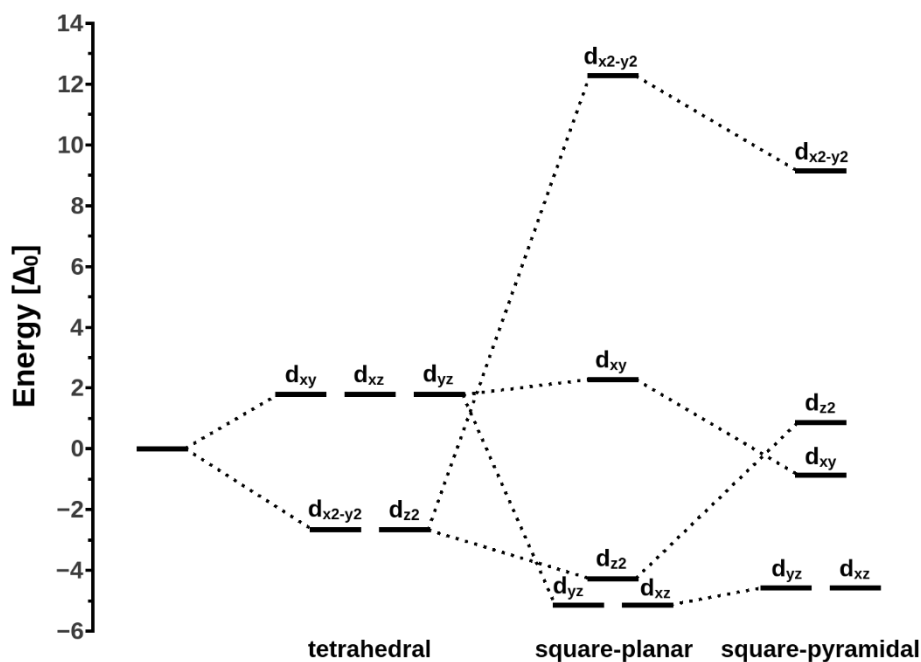


Figure 2: Splitting of the five d-orbitals in a field of tetrahedral (left), square-planar (middle) and square pyramidal (right) symmetry in reference to the unperturbed system, relative energies in units of  $\Delta_0$ .

In the case of  $Zn^{2+}$ , the d-orbitals are fully occupied by ten electrons leading to no stabilization energy of either geometry as energy conservation has to be fulfilled upon the splitting. Instead, interligands steric and electrostatic effects, which are not considered in CFT, lead to a tetrahedral geometry as the interaction between the ligands is minimized.<sup>22</sup> Similar to  $Cu^{2+}$ , solvent molecules tend to occupy the apical positions of a  $Zn^{2+}$  paddle-wheel and enforce a square pyramidal coordination providing rigidity to the framework.

Bureekaew et al.<sup>23</sup> have successfully investigated the considerations mentioned above by computations of copper and zinc paddle-wheels.

While the diamagnetic case of  $Zn^{2+}$  is trivial, complexes of dimeric  $d^9$  Cu are known to have interesting electronic properties. Antiferromagnetic coupling between the two metal ions form an open-shell broken-symmetry singlet making the ground state of such systems famously difficult to compute.<sup>24</sup>

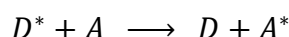
However, electronic effects do not solely govern the growth of MOFs. Different synthesis techniques have been developed to overcome the CFT driven architecture described above. A common method is anchoring the framework on the surface of a substrate, creating so-called SURMOFs.<sup>25</sup> The surface is often covered with a rigid self-assembled

monolayer acting as starting point for the metal nodes and thus enforcing a specific structure on the MOF. The framework is then constructed by alternately immersing the substrate into solutions of metal ions and organic linkers. This enables a controlled step-by-step growth of the structure and is the so-called liquid-phase epitaxy (LPE) approach.<sup>26</sup> The Zn-SURMOF of the second part of this thesis is of such type. The Cu-MOF in the first part is made via a novel approach of simultaneously mixing the substrate and the solutions. Further synthetic details are given in the chapter 5 (Cu-MOF) and chapter 6 (Zn-SURMOF).

### 3 Förster Theory

The following introduction into electronic coupling is mostly based on a review on the subject by Scholes<sup>27</sup> as well as the general overview on excitation energy transfer in a book by May and Kühn.<sup>28</sup> The theoretical derivation of the coupling has been presented in detail in the aforementioned references. This section, however, does not claim to be a full description of the theoretical details, but rather gives insight into the two most common techniques to compute electronic coupling.

Let us consider the general reaction scheme:



After excitation a donor molecule  $D$ , it returns to its ground state and the surplus energy is used to excite an acceptor molecule  $A$ . Deexcitation of the donor may include photon emission and uptake of the energy by the acceptor. However, electronic coupling between both molecules is responsible for radiationless transfer of the energy from the donor to the acceptor.

The most prominent example of such transfer in nature is photosynthesis. Chromophores in light-harvesting proteins absorb sunlight and the excitation energy is transmitted over several nanometres<sup>29</sup> to a reaction centre to ultimately synthesize energy-rich molecules. Inspired by nature, current research is focused on applications of energy transfer including structure determination of biomolecules,<sup>30,31</sup> analysis of polymeric interfaces<sup>32,33</sup> and synthetic light-harvesting.<sup>10,11</sup>

If the energy transfer does not involve the simultaneous transfer of electrons between donor and acceptor, it is called Förster Resonance Energy Transfer (FRET). To be more precise the term is used assuming that only the first excited singlet state contributes to the transfer. As the donor and acceptor are able to form delocalized states, i.e. that they are close together, energy transfer may proceed by exchange of electrons via a Dexter mechanism or Charge Transfer (CT). Figure 3 gives a visualisation of the three energy transfers mentioned.

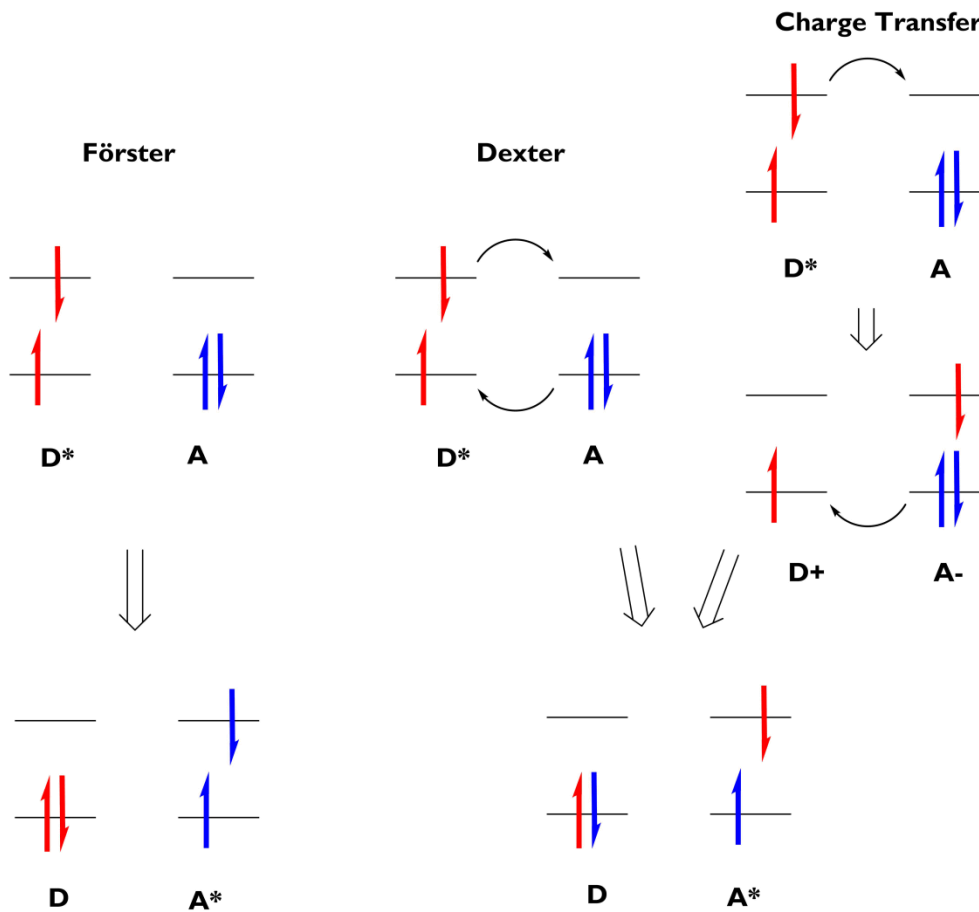


Figure 3: Schematic representation of three different energy transfer mechanisms from donor  $D$  to acceptor  $A$ : Förster (left), Dexter (middle) and charge transfer (right).

Förster<sup>34</sup> was the first one to derive a theory for the rate of such energy transfer. Choosing the Fermi Golden Rule approach, he derived Eq.1 for the rate constant  $k$

$$k = \frac{1}{\hbar^2 c} V^2 J \quad \text{Eq.1}$$

where  $V$  is the electronic coupling and  $J$  is the spectral overlap between the donor fluorescence spectrum and the acceptor absorption spectrum, which have been area-normalized on an energy scale.

The spectral overlap ensures energy conservation and accounts for the temperature dependency of the rate in form of the spectral line shapes. The electronic coupling can generally be expressed as a sum of a Coulombic contribution  $V^{Coul}$ , and a short-range contribution  $V^{short}$  (Eq.2). While the first one is active at all distances, the latter includes the couplings requiring an overlap of orbitals of donor and acceptor mainly occurring at small separation distances (Dexter and CT).

$$V = V^{Coul} + V^{short} \quad \text{Eq.2}$$

A more well-known form of Eq.1 introduced by Förster is formulated in terms of the distance  $R_0$ , the so called Förster radius, at which the Förster resonance energy transfer efficiency is 50%.

$$k^{Förster} = \frac{1}{\tau_D} \left( \frac{R_0}{R} \right)^6 \quad \text{Eq.3}$$

where  $\tau_D$  is the lifetime of the donor and  $R$  the center-to-center separation of donor and acceptor. Eq.3 illustrates best the dependency of FRET on the 6<sup>th</sup>-power of the distance. For comparison, energy transfer based on orbital overlap according to Dexter decreases exponentially.

Förster's theory is limited to a weak coupling regime, where intramolecular relaxation is faster than the intermolecular energy transfer. This results in the incoherent jump model, meaning the excitation moves localized from molecule to molecule. The absence of wavefunction overlap of donor and acceptor, reduces Eq.2 to the Coulomb coupling, which ensures energy transfer without transfer of electrons. Thus, it is contrary to Dexter or Charge-Transfer electronic couplings, where  $V^{short}$  plays a dominant role. Within Förster theory and also within this thesis, the Coulomb coupling is taken as a direct measure for the rate of the energy transfer.

### 3.1 Transition Density

Before further analysing the Coulomb coupling, a key factor in excitation needs to be introduced. The transition density,  $M_n$ , as shown in Eq.4 connects the ground and excited state of a molecule

$$M_n(\vec{r}) = \int_s \Psi_g(\vec{r}) \Psi_e^*(\vec{r}) ds dr \quad \text{Eq.4}$$

The evolution of quantum chemical codes and the possibility to calculate excited-state wavefunctions enable the representation of the transition density in the so-called cube file. This file format generally stores volumetric data, in the present case by integration of the transition density in finite-sized elements with the volume  $V = \delta x \delta y \delta z$ .

$$M_n(x, y, z) = V \int_z^{z+\delta z} \int_y^{y+\delta y} \int_x^{x+\delta x} \int_s \Psi_g \Psi_e^* ds dx dy dz \quad \text{Eq.5}$$

More figuratively speaking, the molecule gets divided into cuboidal segments – hence the name “cube file” – with a part of the transition density assigned to each segment. Information on the electronic transition dipole moment,  $\mu_{tr,n}$ , of molecule  $n$ , which is proportional to the oscillator strength of the excitation, is present via Eq.6.

$$\mu_{tr,n} = \sum_i r_{0i} M_n(i) \quad \text{Eq.6}$$

where  $M_n(i)$  denotes the  $i^{th}$  (x,y,z)-element of molecule  $n$  and  $r_{0i}$  is its distance to the previously appointed centre of the dipole, most often the centre of mass of the molecule.

### 3.2 Ideal Dipole Approximation (IDA)

If the distance between donor and acceptor is large compared to their sizes, the Coulomb coupling can be approximated by a multipolar expansion up to the second-order term. This results in the Ideal Dipole Approximation (IDA) in Eq.7, which corresponds to a Coulomb interaction,  $V^{d-d}$ , between the transition dipole of the donor,  $\mu_D$ , and the acceptor,  $\mu_A$ , with a center-to-center distance  $R$ .

$$V^{d-d} = \frac{1}{4\pi\epsilon_0} \kappa \frac{|\mu_D| |\mu_A|}{R^3} \quad \text{Eq.7}$$

The relative orientation of the dipoles is accounted for in the orientation factor  $\kappa$  (Eq.8).

$$\kappa = \vec{\mu}_D \vec{\mu}_A - 3(\vec{\mu}_D R)(\vec{\mu}_A R) \quad \text{Eq.8}$$

At great distances, the approximation is justified as the molecules do not see each other's transition densities in detailed shape but rather as a point dipole. Combining Eq.7 with Eq.6 leads to the computation of the Coulomb coupling  $V^{d-d}$  according to the ideal dipole approximation:

$$V^{d-d} = \frac{1}{4\pi\epsilon_0} \kappa \frac{|\sum_i r_{Di} M_D(i)| |\sum_j r_{Aj} M_n(j)|}{R^3} \quad \text{Eq.9}$$



### 3.3 Transition Density Cube Method (TDC)

A more evolved description of  $V^{Coul}$  can be derived from quantum mechanics. The intermolecular Coulomb interaction of a dimeric system can be written as the spatial integration with respect to the transition densities of donor D and acceptor A.

$$V^{Coul} = \frac{1}{4\pi\epsilon_0} \int \frac{M_D(\vec{r}_i)M_A(\vec{r}_j)}{|\vec{r}_i - \vec{r}_j|} d\vec{r}_i d\vec{r}_j \quad \text{Eq.10}$$

Making use of the cube files of donor and acceptor in form of Eq.5, Krueger et al.<sup>35</sup> introduced the transition density cube (TDC) method replacing the integration in Eq.10 by a summation over all cube elements (Eq.11).

$$V^{Coul} = \frac{1}{4\pi\epsilon_0} \sum_{ij} \frac{M_D(i)M_A(j)}{r_{ij}} \quad \text{Eq.11}$$

with  $M_D(i)$  and  $M_A(j)$  being the  $i^{th}$  and  $j^{th}$  (x,y,z)-elements of the donor D and the acceptor A transition density  $M_n$ , respectively, and  $r_{ij}$  the distance between those elements.

In contrast to the dipole-dipole approximation, the TDC method accounts for the shape of the transition densities and holds true at any distance between donor and acceptor. It therefore represents an improvement over the IDA, providing an accurate description of the Coulomb coupling in theory and was the method of choice in this work. The *Appendix A2* describes further details about the actual computation including problems, which may arise during the computation and how to avoid them.

## 4 Theoretical Methods

### 4.1 Density Functional Theory

The following chapter serves to outline the basic concepts of Computational Chemistry, in particular, density functional theory (DFT), which has shown to be well suited for the accurate description of many-atom systems. This introduction is based on books by Szabo and Ostlund,<sup>36</sup> Levine<sup>37</sup> and Cramer<sup>38</sup> as well as the references specified in the text.

The central problem in most computational approaches to explain the world of quantum chemistry is to find solutions to the time-independent Schrödinger equation. In its eigenvalue form of  $\hat{H}|\Psi\rangle = E|\Psi\rangle$  the Hamiltonian,  $\hat{H}$ , of the system is applied on the many-body wave function,  $\Psi$ , of the system to yield its total energy  $E$ . For a many-atom system the Hamiltonian is defined as Eq.12

$$\hat{H} = \hat{T}_n + \hat{T}_e + \hat{V}_{nn} + \hat{V}_{ne} + \hat{V}_{ee} \quad \text{Eq.12}$$

with  $\hat{T}_n$  and  $\hat{T}_e$  being the kinetic energy operators of the nuclei and electrons and  $\hat{V}_{nn}$ ,  $\hat{V}_{ne}$ ,  $\hat{V}_{ee}$  being the operators for the nucleus-nucleus, nucleus-electron and electron-electron interaction, respectively.

Due to the huge mass difference between electrons and nuclei, the much lighter electrons can be considered moving in the field of fixed nuclei. This is taken into account in the well-known Born-Oppenheimer approximation and greatly simplifies Eq.12 as the kinetic energy of the nuclei becomes zero and the nucleus-nucleus interaction a constant term. The electronic Hamiltonian can then be written as Eq.13 consisting of the kinetic energy of the electrons, the electron-nucleus interaction and the electron-electron interaction.

$$\hat{H} = -\frac{\hbar^2}{2m_e} \sum_i^N \nabla_i^2 - \sum_i^N \sum_I^M \frac{Z_I e^2}{|r_i - R_I|} + \sum_i^N \sum_{j \neq i}^N \frac{e^2}{|r_i - r_j|} \quad \text{Eq.13}$$

At this point the work of Hohenberg und Kohn<sup>39</sup> laid the foundation of density functional theory by showing that all properties of a system can be described by its ground state density. Together with Eq.13 the electronic ground state energy of a system can then be formulated as a functional of the electron density  $n(r)$  (Eq.14).

$$E[n(r)] = T_e[n(r)] + \int d^3r v(r)n(r) + E_{ee}[n(r)] \quad \text{Eq.14}$$

where  $T_e$  and  $E_{ee}$  are the kinetic energy of the electrons and the electron-electron interaction, respectively, and  $v(r)$  is an external potential describing the interaction of the electrons with the nuclei. However, the exact functional for a many-electron system is not known.

A practicable solution useful for the computation of chemical systems came from Kohn and Sham<sup>40</sup> by introducing an auxiliary system of non-interacting electrons, which have the same ground state density as the real system. This means,  $E_{ee}[n(r)]$  equals 0 and the Hamiltonian of the new system,  $\hat{H}_S$ , can be written as the sum of single particle Hamiltonians,  $\hat{h}_{S,i}$ , of non-interacting electrons moving in a fictitious external potential  $v_{KS}$  (Eq.15).

$$\hat{H}_S = \hat{T}_{S,e} + \int d^3r v_{KS}(r)n(r) = \sum_{i=1}^N \hat{h}_{S,i} \quad \text{Eq.15}$$

with

$$v_{KS}(r) = v(r) + v_H(r) + v_{xc}(r) \quad \text{Eq.16}$$

In Eq.16 the KS potential includes the external potential  $v(r)$ , the classical Coulomb interaction of the electron density with itself  $v_H(r)$ , and the exchange-correlation potential  $v_{xc}(r)$  for all non-classical many body effects. Such are the non-classical two-electron interactions, caused by self-interaction, exchange and correlation effects as well as the difference in kinetic energy between the non-interacting system and the interacting one.

This description enables the construction of  $N$  one-electron Schrödinger equations, the so-called Kohn-Sham equations (Eq.17), which can be solved in a self-consistent manner.

$$\hat{h}_{S,i}\varphi_i(r) = \left( -\frac{\hbar^2}{2m_e} \nabla^2 + v_{KS}(r) \right) \varphi_i(r) = \varepsilon_i \varphi_i(r) \quad \text{Eq.17}$$

At this point it has to be noted, that the KS-wavefunctions,  $\varphi_i(r)$ , alone have in general no physical meaning. The ground state density of the  $N$ -particle system, however, is related to the Kohn-Sham orbitals by Eq.18.

$$n(r) = \sum_{i=1}^N |\varphi_i(r)|^2 \quad \text{Eq.18}$$

Within the Kohn-Sham approach the electronic ground state energy of Eq.14 can then be rewritten as Eq.19

$$E_{KS} = T_{S,e}[n(r)] + \int d^3r v(r)n(r) + E_H[n(r)] + E_{xc}[n(r)] \quad \text{Eq.19}$$

where  $T_S$  is the kinetic energy of the non-interacting electrons,  $v(r)$  the external potential,  $E_H$  the Coulomb interaction of the electrons and  $E_{xc}$  the exchange correlation energy.

## 4.2 Exchange-correlation Approximations

Knowing the exact exchange-correlation functional is still a major goal in theoretical chemistry, as this would yield the exact ground state energy. Meanwhile approximations are used in calculations, one of which is the Generalised Gradient Approximation (GGA). As shown in Eq.20  $E_{xc}^{GGA}$  is not only expressed as a functional of the density, but also involves the gradient of the density.

$$E_{xc}^{GGA} = \int d^3r n(r) e_{xc}[n(r), \nabla n(r)] \quad \text{Eq.20}$$

The Perdew-Burke-Ernzerhof<sup>41</sup> functional (PBE), which is used in this thesis for all periodic calculations, is of such form. The Perdew-Wang correlation functional is combined with the exchange functional  $E_x^{PBE}$  shown in Eq.21

$$E_x^{PBE} = \frac{bx^2}{1+ax^2} \quad \text{Eq.21}$$

where  $a = 0.00449$ ,  $b = 0.00336$  and  $x = |\nabla n(r)|/n(r)^{4/3}$ . It is chosen due to its good performance in periodic calculations with a deviation of the lattice constant by 1.3 %<sup>42</sup> and the accuracy of bond lengths within 0.01 Å to experiment.<sup>43</sup>

Adamo and Barone extended the functional by including a fraction of exact Hartree Fock exchange,  $E_x^{HF}$ , creating the hybrid-functional PBE0<sup>44</sup> (Eq.22), which is used for all molecular calculations. PBE0 has particularly proven to be a good choice for the calculation of excitation energies with an average error of 0.25 eV.<sup>45</sup>

$$E_{xc}^{PBE0} = \frac{1}{4} E_x^{HF} + \frac{3}{4} E_x^{PBE} + E_c^{PBE} \quad \text{Eq.22}$$

Hybrid-functionals are usually considered the more sophisticated methods. However, their increased computational cost makes them of limited use for larger periodic systems.

### 4.3 Time-dependent Density Functional Theory

As it is already apparent from the name, time-dependent density functional theory (TD-DFT) is an extension to the theory described above to solve the time-dependent Schrödinger equation  $\hat{H}(t)\Psi(t) = i\frac{\partial}{\partial t}\Psi(t)$ . Applying the Born-Oppenheimer approximation the electronic Hamiltonian from Eq.13 can be written in its time-dependent form (Eq.23)

$$\hat{H}(t) = \hat{T}_e + \hat{V}_{ne}(t) + \hat{V}_{ee}(t) \quad \text{Eq.23}$$

where  $\hat{T}_e$  is the kinetic energy operator,  $\hat{V}_{ne}$  is the Coulomb operator and  $\hat{V}_{ee}$  is the external potential. Analogous to the Hohenberg-Kohn theorem, Runge and Gross laid the foundation of TDDFT by linking the time-dependent external potential to the time-dependent density.<sup>46</sup> Thus, all properties of a many-atom system can again be described by its electron density.

Using the Kohn-Sham approach an auxiliary system of non-interacting electrons is introduced with a fictitious, time-dependent effective potential  $v_{KS}$ .

$$v_{KS}(r, t) = v(r, t) + v_H(r, t) + v_{xc}(r, t) \quad \text{Eq.24}$$

Eq.24 is the time-dependent form of Eq.16 with the external potential  $v$ , the Hartree potential  $v_H$  and the exchange potential  $v_{xc}$ . Analogue to ground state DFT time-dependent Kohn-Sham equations are constructed, which need to be solved numerically. However, the time-dependent exchange potential is considerably challenging to approximate.

Instead, many computer programs apply the easier linear response formalism based on perturbation theory. According to this formalism a time-dependent external perturbation causes small changes in the ground state density  $n_0(r)$  (Eq.25)

$$n(r, t) = n_0(r) + n_1(r, t) + n_2(r, t) + \dots \quad \text{Eq.25}$$

$n_1(r, t)$  is the first order response of the density to the perturbation (linear response) and is dominating for small changes. Thus, higher order terms ( $n_2$ , etc.) are neglected within this approach. The linear response can be written as Eq.26:

$$n_1(r, t) = \int \int \chi(r, t, r', t) v_1(r', t) d^3r' dt \quad \text{Eq.26}$$

where  $v_1$  is the perturbation and  $\chi$  the density response function. The latter contains information about the spectroscopic observables of the system. In contrast to TD-DFT, the

linear response approach depends only on ground state DFT. The lack of the calculation of time-dependent Kohn-Sham wavefunctions is the big advantage of this method.

#### 4.4 Basis Set

In wavefunction-oriented methods like Hartree-Fock molecular orbitals,  $\varphi$ , are expressed as linear combination of atomic orbitals (LCAO),  $\phi_i$ , multiplied by a corresponding coefficient,  $c_i$ , (Eq.27).

$$\varphi = \sum_i c_i \phi_i \quad \text{Eq.27}$$

Due to the introduction of orbitals through the Kohn-Sham equations (Eq.17) the LCAO-approach is equally interesting in calculations of the previously orbital-free density functional theory. In the mathematical procedure of quantum chemical computations atomic orbitals are represented by basis functions centered at the nuclei of the system and form the basis set of the calculation.

Two types of functions have established, namely Slater-type functions,  $\phi_{SF}$  (Eq.28), and Gaussian-type functions,  $\phi_{GF}$  (Eq.29). The equations below show the dependency of their radial part on the distance,  $r$ , of the electron from the atomic nucleus. The coefficients  $\zeta$  and  $\alpha$  are the Slater orbital and Gaussian orbital exponents, respectively, and determine the diffuseness of the function.

$$\phi_{SF} \propto e^{-\zeta r} \quad \text{Eq.28}$$

$$\phi_{GF} \propto e^{-\alpha r} \quad \text{Eq.29}$$

It can be shown that the slower decrease of the Slater functions describes the qualitative properties of orbitals more correctly. In particular, this becomes apparent by comparing the exact solution for the 1s orbital of the hydrogen atom  $(\pi)^{-1/2} e^{-r}$ . However, integration of Gaussian functions is less time-consuming, which is the reason why this type is usually given the preference in modern calculations.

The basis sets used in this work belong to the diverse group of Karlsruhe basis sets introduced by Weigend and Ahlrich.<sup>47</sup>

For the periodic calculations in FHI-Aims the program-internal numeric atom-centered basis set is utilized.

## 4.5 Van der Waals Correction

It is well known that long range electronic interactions are not properly described within DFT,<sup>48,49</sup> however, they play an important role in many systems. Thus, to correct for such van der Waals forces an interaction energy term,  $E_{vdW}$ , is added to the calculated DFT energy,  $E_{DFT}$ , to give the total energy of the system,  $E_{total}$ , (Eq.30).

$$E_{total} = E_{DFT} + E_{vdW} \quad \text{Eq.30}$$

Different approaches to account for this have been proposed, two of which have been used in this work. The method of Tkatchenko and Scheffler<sup>50</sup> as implemented in FHI-Aims was applied for the periodic calculations. It is based on the expression in Eq.27 as a pairwise interatomic correction

$$E_{vdW} = -\frac{1}{2} \sum_{A,B} f_{d,6}(R_{AB}, R_A^0, R_B^0) \frac{C_{6AB}}{R_{AB}^6} \quad \text{Eq.31}$$

where  $R_{AB}$  is the distance between the atoms  $A$  and  $B$  and  $R_A^0$  and  $R_B^0$  are their vdW radii.  $C_{6AB}$  is the corresponding dispersion coefficient and  $f_{d,6}$  a short range damping function. Both are dependent on the ground state charge-density and, thus, account for the local chemical environment of the atoms.

The molecular calculations apply Grimme's D3 correction method<sup>51</sup> as implemented in ORCA. Looking similar to the correction scheme in Eq.31 a second dispersion coefficient,  $C_{8AB}$ , and damping function,  $f_{d,8}$ , is added in Eq.32. Although the charge-density is not involved this time, the dispersion coefficients are also adjusted according to the local geometry around the atoms.

$$E_{vdW} = -\frac{1}{2} \sum_{A,B} \left( f_{d,6}(R_{AB}, R_A^0, R_B^0) \frac{C_{6AB}}{R_{AB}^6} + f_{d,8}(R_{AB}, R_A^0, R_B^0) \frac{C_{8AB}}{R_{AB}^8} \right) \quad \text{Eq.32}$$

## 5 Epitaxial Growth of a Cu-MOF

### 5.1 Background and Motivation

This section is inspired by the work of P. Falcaro et al.<sup>52</sup>, who describe a new fabrication method for the synthesis of heteroepitaxial MOF films. In general, heteroepitaxial films grow on substrates in such a way, that the deposited film is oriented along at least one direction of the substrate's crystal structure. In the present case, a precisely aligned micropore Cu-framework is synthesized on the (010) surface of highly orientated  $\text{Cu}(\text{OH})_2$  nanobelts. For this, the substrate is converted to the MOF in a single-step synthesis after immersing it in a saturated ethanolic solution of the linker. The metal ions form  $\text{Cu}^{2+}$  - paddle-wheels, which are connected by the carboxylic groups of the organic linker molecules. A schematic representation of the system is shown in Figure 4.

Terephthalic acid (=1,4-benzenedicarboxylic acid, BDC) was used as a linker (Figure 4), since cell parameters of MOFs with this molecule<sup>21</sup> match those of  $\text{Cu}(\text{OH})_2$  and, thus, promise epitaxial growth.

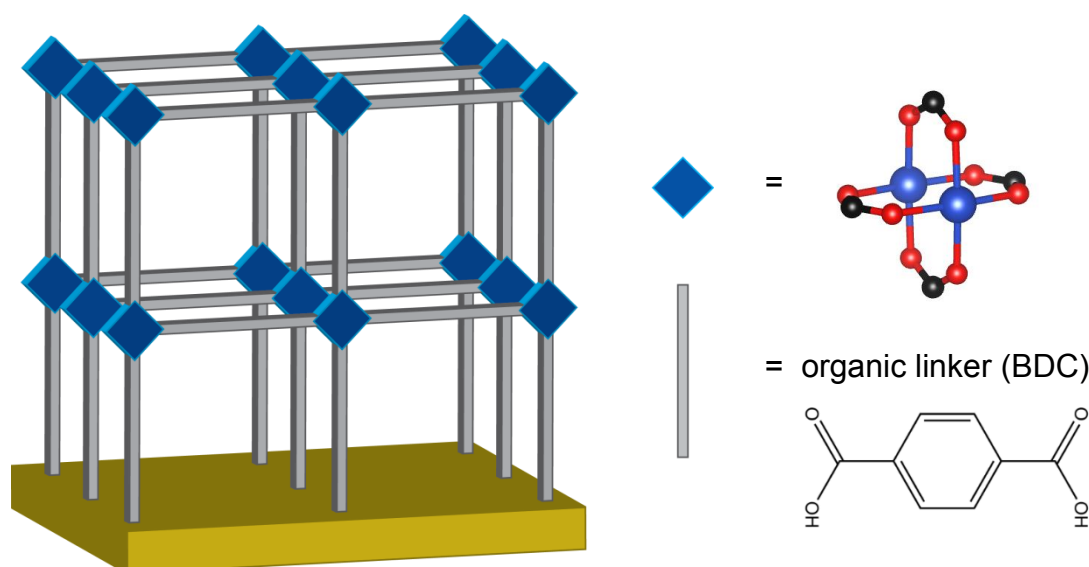


Figure 4: Schematic structure of the Cu-MOF on  $\text{Cu}(\text{OH})_2$  substrate and skeletal formula of BDC, blue = Cu-paddle-wheel, yellow =  $\text{Cu}(\text{OH})_2$ , grey = linker.

The metal nodes for the framework are directly provided by partially dissolving the metal hydroxide substrate. The heteroepitaxial growth is confirmed by electron diffraction pattern and XRD. Based on these data, P. Falcaro proposed an orthorhombic unit cell of the MOF (cell A) film, shown in Figure 5. For comparison, Figure 5 also shows the unit cell of a solvent free Cu-BDC MOF (cell B) described in the literature.<sup>20</sup>



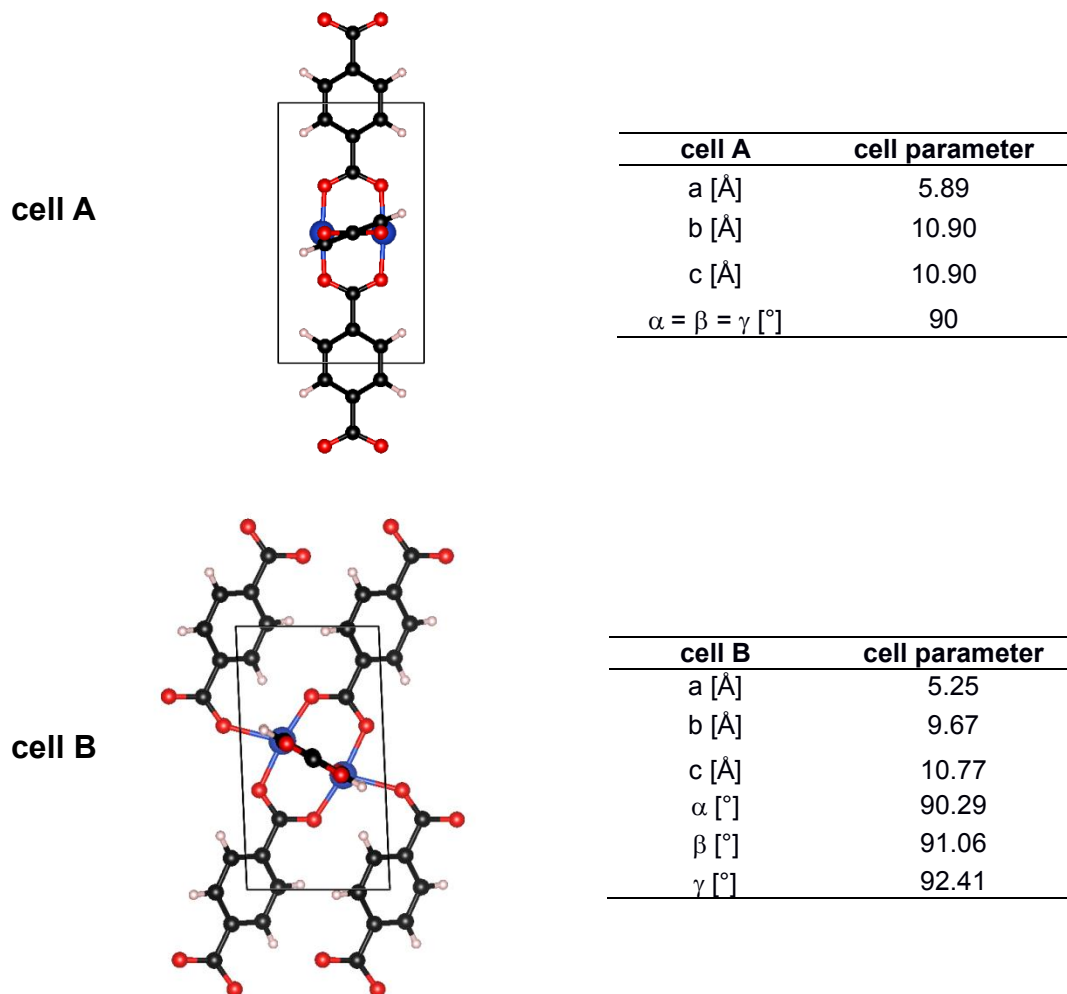


Figure 5: Unit cell and cell parameters of the cell proposed by Falcaro<sup>52</sup> (cell A) and the cell of the solvent free Cu-BDC MOF (cell B) found in literature<sup>20</sup>.

The difference in the two crystal structures is attributed to the heteroepitaxial growth. However, the growth process and the interface at the surface have not yet been described in all details. The theoretical work aims to gain a deeper insight into the formation of the framework and the cause of the epitaxy.

## 5.2 Computational Details

This section contains technical details about the computation as well as benchmarking data for the Cu-MOF.

### 5.2.1 Molecular calculations

Molecular calculations were made to test electronic spin state properties of  $\text{Cu}^{2+}$ -dimers. Therefore, a single SBU (Cu-paddle-wheel coordinating four terephthalic acids, with the apical positions saturated with two water molecules, see Figure 6) was calculated quantum mechanically using ORCA 4<sup>58</sup> in three different spin states: closed shell singlet, open shell triplet and broken-symmetry open shell singlet. The structures were optimized on the PBE<sup>41</sup> and PBE0<sup>44</sup> level of theory with a def2-SVP basis set<sup>47</sup> and Grimme's D3 dispersion correction<sup>51</sup>. Using the same functionals, single point energies were calculated with def2-TZVP<sup>47</sup>. The SBU without the water molecules as well as a single water molecule was computed following the same procedure to investigate the coordination energy of the cluster.

### 5.2.2 Benchmarking of the spin state

The computation of  $\text{Cu}^{2+}$ -dimers is a well-known problem.<sup>24</sup> As already mentioned in the introduction to metal-organic frameworks, weak interaction between the ions leads to a broken-symmetry open shell singlet. However, such systems are difficult to compute and time consuming with DFT. Therefore, a feasible description of the dimers is tested with molecular calculations.

Figure 6 shows the structural differences of the three spin state optimizations. Table 1 lists some bond lengths characteristics for the coordination compound.  $r_{\text{Cu}}$  is the distance between the Cu ions,  $r_{\text{H}_2\text{O}}$  the distance from the Cu ions to the coordinating water molecules and  $r_{\text{OOCR}}$  the distances from the Cu ions to the carboxylate ligands. As one can see, the broken-symmetry and triplet state geometries deviate less than 1 %, whereas the singlet state shows a different coordination environment. Table 1 also compares the total energies relative to the broken-symmetry ground state showing that the singlet state is energetically high above. The triplet state is almost energetically equivalent to the broken-symmetry state. This trend is the same for energies of the def2-SVP geometry optimizations as well as the def2-TZVP single points on these structures.

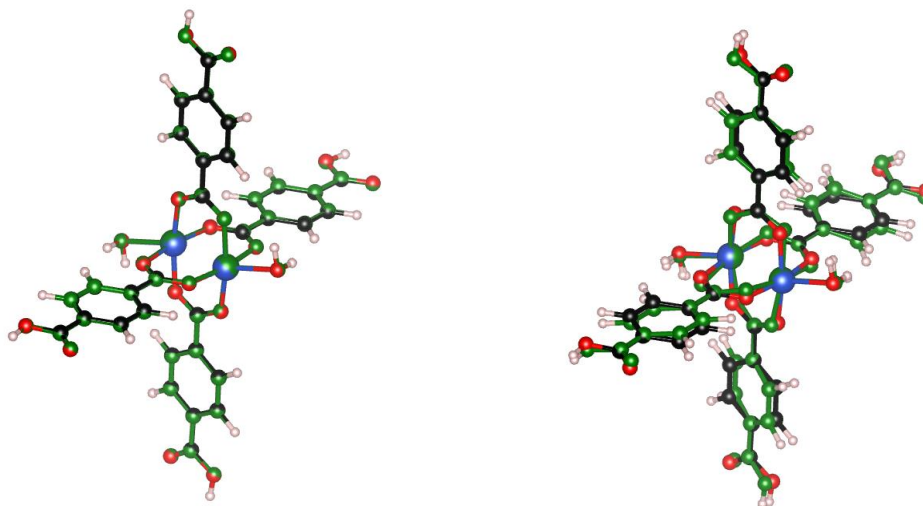


Figure 6: Comparison of the PBE0+D3/def2-SVP optimized broken-symmetry and triplet (left) as well as the triplet and singlet state (right) geometries, triplet=black, other state=green.

Table 1: Relevant bond lengths of the coordination sphere after PBE0+D3/def2-SVP optimization,  $r_{Cu}$ =Cu-Cu,  $r_{H_2O}$ =Cu-H<sub>2</sub>O,  $r_{COOR}$ =Cu-OOCR. Relative energies of the def2-SVP optimized structures and of the def2-TZVP single points.

	broken-symmetry	triplet	singlet
$r_{Cu}$ [Å]	2.607	2.607	2.581
$r_{H_2O}$ [Å]	2.223	2.223	2.250
$r_{COOR}$ [Å]	2.001	2.001	2.009
	1.964	1.963	1.970
Rel. Energy [eV]			
def2-SVP (opt)	0.00	0.02	1.75
def2-TZVP (sp)	0.00	0.02	1.68

Additionally, the influence of the functional on energetic differences was investigated. For this, the coordination energy,  $E_{Coord}$  of two water molecules as defined in Eq.33 was computed.  $E_{complex}$  is the energy of the saturated complex,  $E_{ligand}$  is the energy of a single water molecule and  $E_{paddle}$  is the energy of the paddle-wheel without the water molecules. A visualisation of the reaction equation is shown in Figure 7. Table 2 lists the energies calculated applying two different functionals. In both cases, the energetics described by the triplet state can be well compared to the broken-symmetry state. It was not possible to converge the optimization of the unsaturated cluster in the singlet state in case of the PBE calculations. Therefore, this coordination energy is not shown in Table 2.

$$E_{Coord} = E_{complex} - 2 * E_{ligand} - E_{paddle} \quad \text{Eq.33}$$

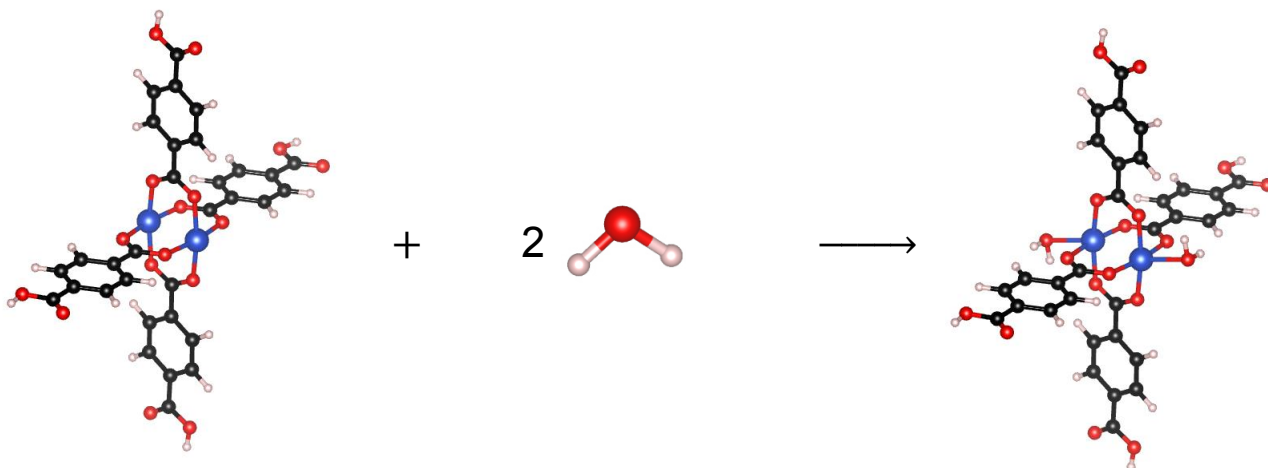


Figure 7: Visual presentation of the reaction equation of the coordination of water to a Cu paddle-wheel cluster.

Table 2: The coordination energy  $E_{Coord}$  of two water molecules with two different functionals in three different spin states.

	PBE0 [eV]	PBE [eV]
broken-symmetry	-1.22	-1.08
triplet	-1.22	-1.08
singlet	-1.06	-

As likewise shown in literature<sup>53,54</sup> the calculated triplet state geometry closely resembles the broken-symmetry ground state of copper paddle-wheels and both states are almost energetically equivalent. That both states have very similar properties can also be observed experimentally for such Cu-dimers.<sup>55</sup> Thus, the copper systems are computed periodically as open shell triplets.

### 5.2.3 Periodic calculations

For all periodic calculations, the PBE<sup>41</sup> functional with *Tight* settings of the numeric atom-centered basis set and dispersion correction (Tkatchenko-Scheffler<sup>50</sup>) as implemented in FHI-Aims<sup>61</sup> was applied. A detailed description of the basic functions used in this program-intern basis set is given in the *Appendix A3*. The unit cell of the Cu-MOF (cell A:  $a=5.89$  Å,  $b=c=10.90$  Å and cell B:  $a=5.25$  Å,  $b=9.67$  Å,  $c=10.77$  Å) was fully optimized using a 4x2x2 k-point grid. Moreover, the lattice constants of cell A ( $a=5.89$  Å,  $b=c=10.90$  Å) were optimized constraining the cell angles to 90°.

The atomic positions of the bulk of the Cu(OH)<sub>2</sub> substrate were relaxed in a constraint unit cell taken from the American Mineralogist Crystal Structure Database<sup>56</sup> ( $a=2.95$  Å,  $b=10.59$  Å,  $c=5.26$  Å) on a 8x2x4 k-point grid. The 010 surface was built out of the relaxed bulk substrate containing four layers of Cu(OH)<sub>2</sub> and calculated with the repeated slab approach ( $a=5.90$  Å,  $b=10.42$  Å,  $c=70$  Å) using a 8x4x1 k-point grid. For this, a vacuum

region of 60 Å as well as a dipole correction is introduced, and the lowest of the four layers is constrained. To model the interface of  $\text{Cu}(\text{OH})_2$  with the MOF, BDC molecules are placed on the 010 surface. The atomic positions are relaxed using a  $8 \times 4 \times 1$  k-point grid again utilizing the repeated slab approach and fixing the lowest of four layers  $\text{Cu}(\text{OH})_2$ . The atomic ZORA approximation was applied in all calculations for relativistic treatment.

## 5.3 Results and Discussion

### 5.3.1 MOF bulk

First, the MOF bulk structure without the substrate was investigated starting from the unit cells introduced in the motivation-section above. The cell parameters of the orthorhombic unit cell proposed by P. Falcaro et al.<sup>52</sup> (cell A) as well as of the unit cell found in literature<sup>20</sup> (cell B) were fully optimized to find the favorable bulk structure of the MOF. The unit cell parameters of the optimized structures are listed in Table 3. While cell B from literature remained almost the same during the optimization, the orthorhombic cell A underwent a major tilting (see Table 3 and Figure 8). The driving force for the tilt is the coordination environment of the copper paddle wheel. In accordance with CFT (vide supra), the  $\text{Cu}^{2+}$  ion tends towards a square pyramidal coordination sphere. To make this coordination possible, the paddle-wheel SBUs tilt and coordinate to an O-atom of the next paddle wheel.

Table 3: Lattice constants  $a$ ,  $b$  and  $c$ , cell angles  $\alpha$ ,  $\beta$  and  $\gamma$ , cell volume  $V$  and relative energies  $E_{\text{rel}}$  before and after optimization of the bulk structures proposed by Falcaro (cell A) and the one found in literature (cell B) (all PBE+TS/tight).

	$a$ [Å]	$b$ [Å]	$c$ [Å]	$\alpha$ [°]	$\beta$ [°]	$\gamma$ [°]	$V$ [Å <sup>3</sup> ]	$E_{\text{rel}}$ [eV]
cell A start (Falcaro)	5.89	10.90	10.90	90	90	90	699.79	-
cell A opt	5.29	10.91	10.88	95.52	92.53	116.35	557.51	0.00
cell B start (lit.)	5.25	9.67	10.77	90.29	91.06	92.41	546.18	-
cell B opt	5.31	9.79	10.87	93.76	86.91	92.56	562.76	0.01

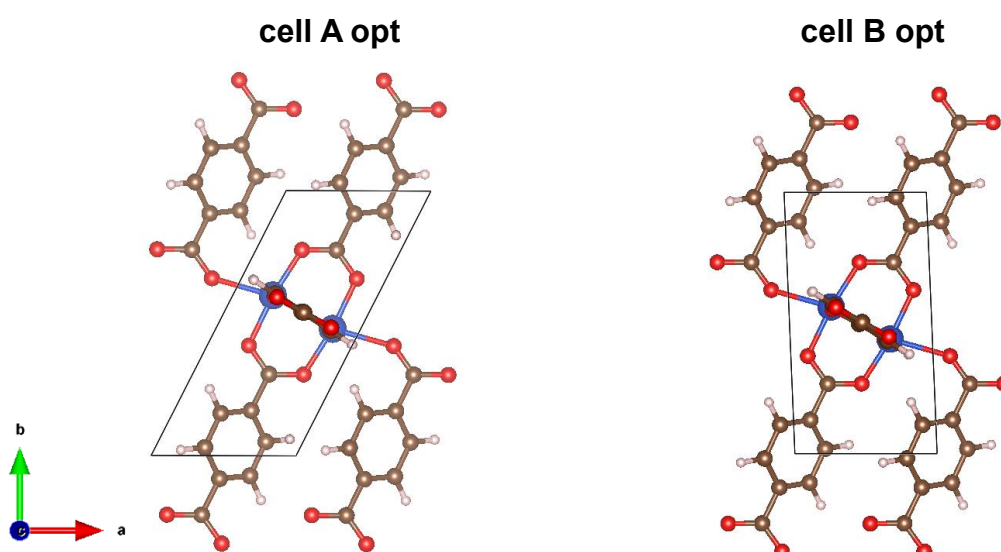


Figure 8: Optimized unit cell of cell A (left) and cell B (right) along the  $c$ -axis showing both times the square pyramidal coordination of the copper paddle wheel (PBE+TS/tight).

Interestingly, the overall structure turns out to be almost the same independent of the two starting geometries (shown in Figure 9). This is due to the fact that the bulk framework can be built up by either of the two different unit cells. However, cell A is smaller and the arrangement is 0.01 eV more stable. In absence of solvent or other directing effects, full relaxation of the bulk will always result in the framework shown in Figure 9 due to CFT. The  $\text{Cu}(\text{OH})_2$  substrate must provide thus directing effects to stabilize the structure found by P. Falcaro et al.<sup>52</sup>

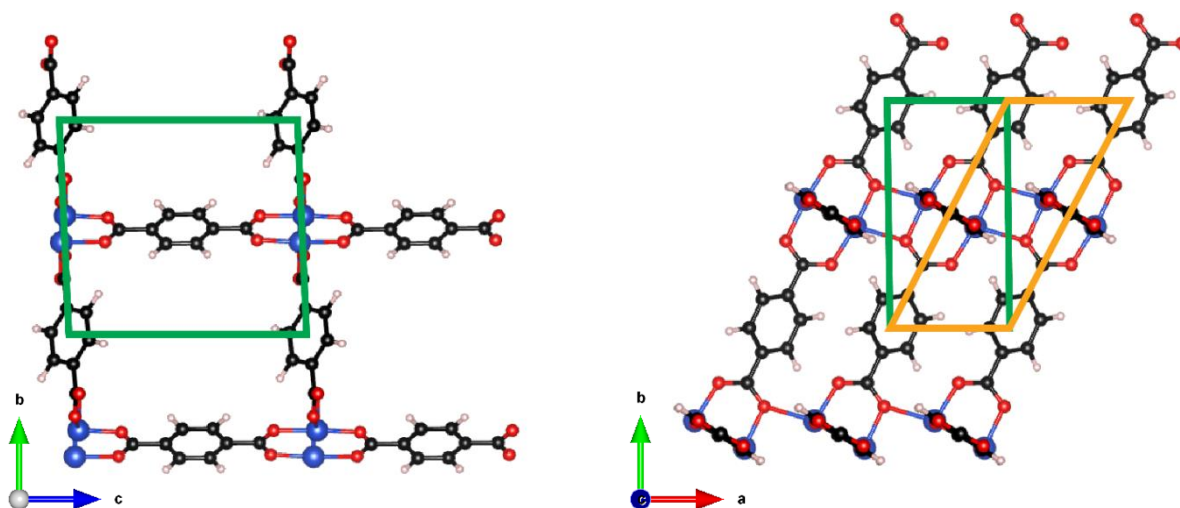


Figure 9: Fully relaxed bulk structure of the Cu-MOF (PBE+TS/tight) along the a-axis (left) and c-axis (right), the two different unit cells are marked, orange = cell A opt, green = optimized cell B opt.

As full optimization of the orthorhombic unit cell A distorted the proposed framework of P. Falcaro et al.,<sup>52</sup> the calculation was repeated with constrained cell angles. Ensuring the orthorhombic character leads to the cell displayed in Figure 10 (cell C). The cell constants are close to the ones proposed by P. Falcaro et al.<sup>52</sup> (compare Figure 5). Cell C is 0.66 eV less stable than the fully relaxed cell A.

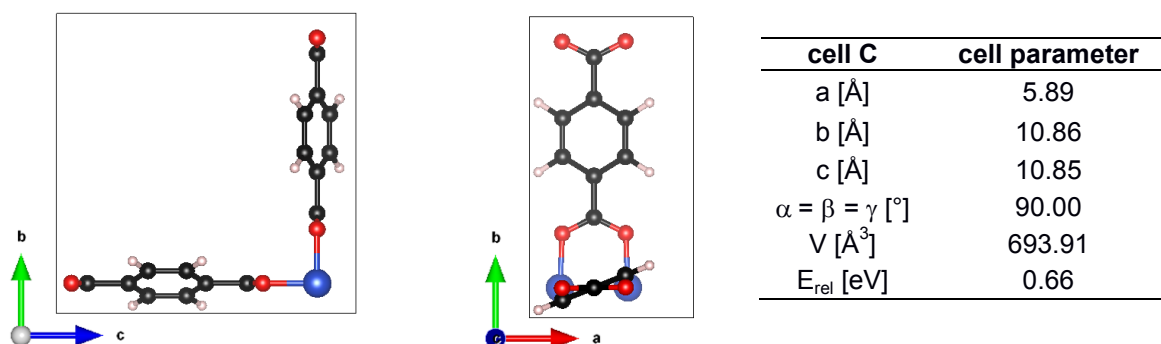


Figure 10: Optimized unit cell and cell parameters (lattice constants a, b and c, cell angles  $\alpha$ ,  $\beta$  and  $\gamma$ , cell volume V and energy relative to cell A) of the Cu-MOF (PBE+TS/tight) ensuring the orthorhombic character by constraining the cell angles (cell C).

### 5.3.2 The substrate

In the next step, the 010  $\text{Cu}(\text{OH})_2$  surface is modelled. The substrate is made out of  $\text{Cu}(\text{OH})_2$  nanobelts. Information about the unit cell of this material was taken from ref.56 and is presented in Figure 11.

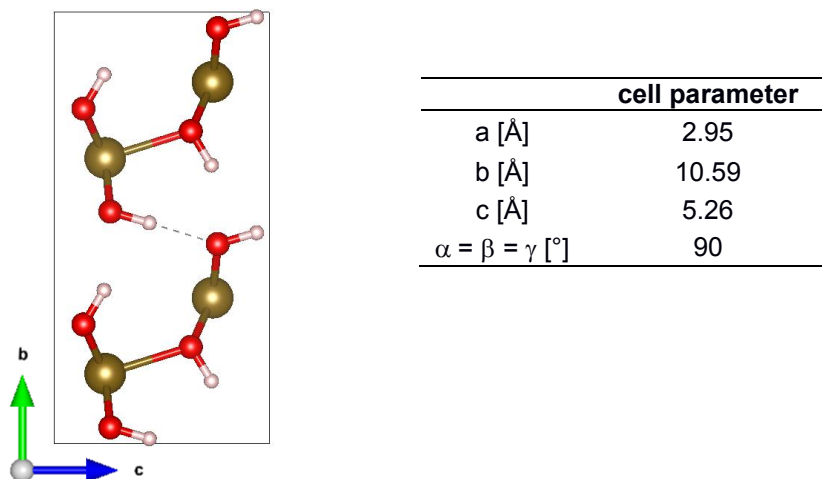


Figure 11: Unit cell and cell parameters of bulk  $\text{Cu}(\text{OH})_2$  taken from ref.56.

Apparently, the substrate is vital for the correct orientation of the framework enforcing the observed orthorhombic system. The Cu-MOF grows on the (010) surface of the  $\text{Cu}(\text{OH})_2$  nanobelts. For the simulations, this surface was built from the relaxed bulk unit cell of  $\text{Cu}(\text{OH})_2$  and was chosen such, that the lengths in the [100] and [001] directions resemble the proclaimed unit cell of the MOF. For this, the a- and c-axis of the  $\text{Cu}(\text{OH})_2$  bulk were doubled (5.90 and 10.52 Å, respectively). The corresponding lattice constants of the MOF (5.89 and 10.85 Å) deviate by less than 4 %. A scheme of the substrate/MOF interface can be seen in Figure 12, where the anchor points for the MOF are shown in blue.

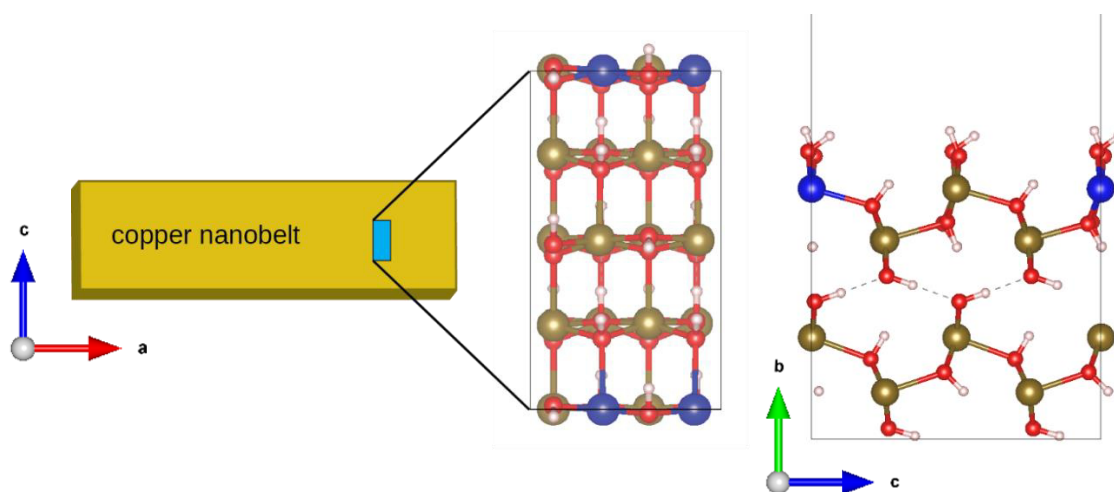


Figure 12: Left: Top view of the  $\text{Cu}(\text{OH})_2$  surface (010). Right: View along the a-axis of the  $\text{Cu}(\text{OH})_2$  surface with four layers used in periodic calculations. Blue Cu atoms mark the ions, which distances are responsible for the heteroepitaxy of the MOF.



All OH-groups of the  $\text{Cu}(\text{OH})_2$  bulk structure face in the same direction due to the hydrogen bonds within the network. However, in contrast to the bulk, the OH groups on the surface of  $\text{Cu}(\text{OH})_2$  can reorient, meaning, they face in alternate directions. In this context, two arrangements of the OH-groups can be distinguished as indicated by the arrows in Figure 13. The structure with the OH groups pointing alternately towards and away from each other along the c-axis will further be called the a-surface. When they all face the same direction along the c-axis the structure will be called the b-surface. Calculations suggest that the a-surface is 0.02 eV more stable than the b-surface.

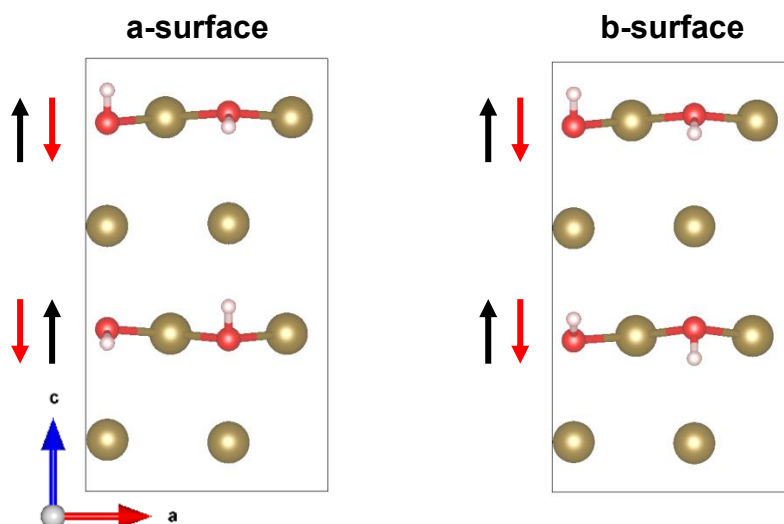


Figure 13: Arrangements of the OH-groups on a  $\text{Cu}(\text{OH})_2$  surface (010); a-surface (left) and b-surface (right). For clarity only the two uppermost  $\text{Cu}^{2+}$  positions and the top OH groups are shown (PBE+TS/tight).

### 5.3.3 Substrate and MOF

The actual heteroepitaxial growth process of the Cu-MOF is unknown. We hypothesized, that, as a first step, a self-assembling monolayer (SAM) of terephthalic acid (BDC) could form on the surface. Therefore, this structure was tested by placing two BDC molecules on each of the surfaces as shown in Figure 14. Two BDC molecules in the chosen unit cell corresponds to full coverage of the surface. The docking of BDC is dominated by H-bonds between the carboxylic acid and the OH-groups of  $\text{Cu}(\text{OH})_2$ . Depending on the orientation of the carboxylic group, the lines of BDC molecules are either aligned (called parallel) or form a zipper-like pattern (called shifted), all in all resulting in four different arrangements. The four systems are schematically shown in Figure 14, and their energetics are listed in Table 4 relative to the structure with the lowest energy. The trend consolidates that the b-surface is unfavorable. This is most likely due to fewer H-bonding on the surface. A distinct difference between the parallel and shifted arrangement is not found. A larger section of the two different patterns on the surface is shown in Figure 15.

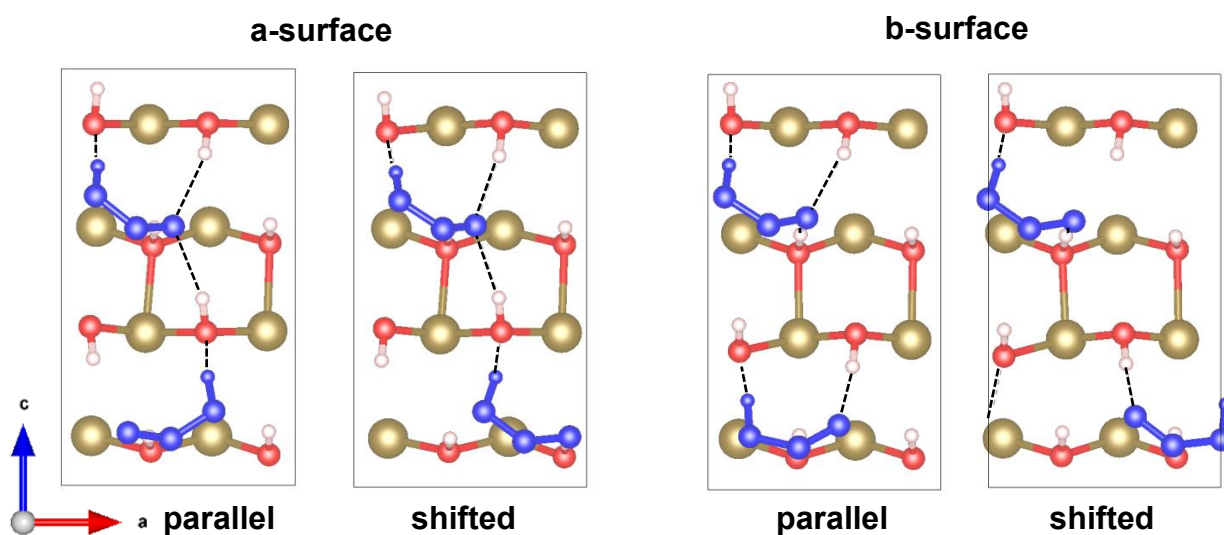


Figure 14: Parallel and shifted arrangement of BDC on the  $\text{Cu}(\text{OH})_2$  a-surface (left) and b-surface (right); for clarity only the two uppermost  $\text{Cu}(\text{OH})_2$  layers and the binding COOH of BDC are shown (PBE+TS/tight).

Table 4: Relative energies of the different arrangements of BDC on  $\text{Cu}(\text{OH})_2$  according to PBE+TS/tight calculations.

System	relative energy [eV]	relative energy [kJ/mol]
a/parallel	0.00	0.00
a/shifted	0.02	1.93
b/parallel	0.22	21.22
b/shifted	0.24	23.16

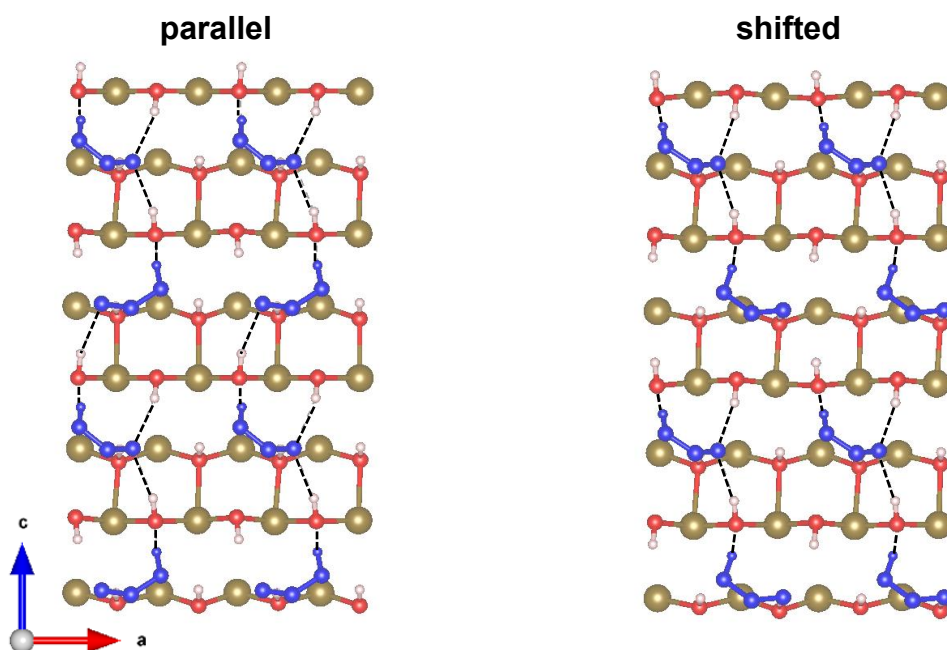


Figure 15: Parallel (left) and shifted (right) arrangement of BDC on the  $\text{Cu}(\text{OH})_2$  a-surface; for clarity only the two uppermost  $\text{Cu}(\text{OH})_2$  layers and the binding COOH of BDC are shown (PBE+TS/tight).

The organic molecules are orientated at the surface with a tilt-angle of  $43^\circ$  and rotated such that their aromatic systems show parallel displaced pi-stacking (Figure 16).

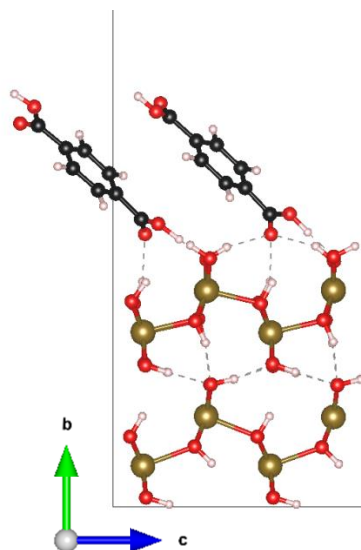


Figure 16: View of the parallel arrangement of BDC on the  $\text{Cu}(\text{OH})_2$  a-surface along the a-axis (PBE+TS/tight).

Similar to some liquid-phase epitaxy approaches,<sup>21</sup> the SAM could function as a layer on which the framework is build.

Figure 17 shows two possible MOF structures growing on a BDC monolayer. These structures are solely hypothetical and were created by placing both the orthorhombic cell C and the optimized cell A, respectively, on the parallel BDC monolayer on the a-surface. In both cases, the copper paddle wheel has more or less square planar coordination environment. Although the tilted arrangement on the right side of Figure 17 is close to square pyramidal coordination, the distance of the apically bridging O-atom to the Cu-paddle wheel is about 3 Å compared to 2 Å in the  $\text{Cu}(\text{BDC})$  bulk (optimized cell A). The paddle wheel SBU and, thus, also the carboxylic acid functionality of the BDC of the SAM would have to tilt further to reach the square pyramidal coordination.

However, due to full coverage, the BDC molecules are limited in their movements by sterical hindrance. The rigidity of the SAM would thus be responsible for the stabilization of the MOF structure as it prevents further tilting of the paddle-wheel.

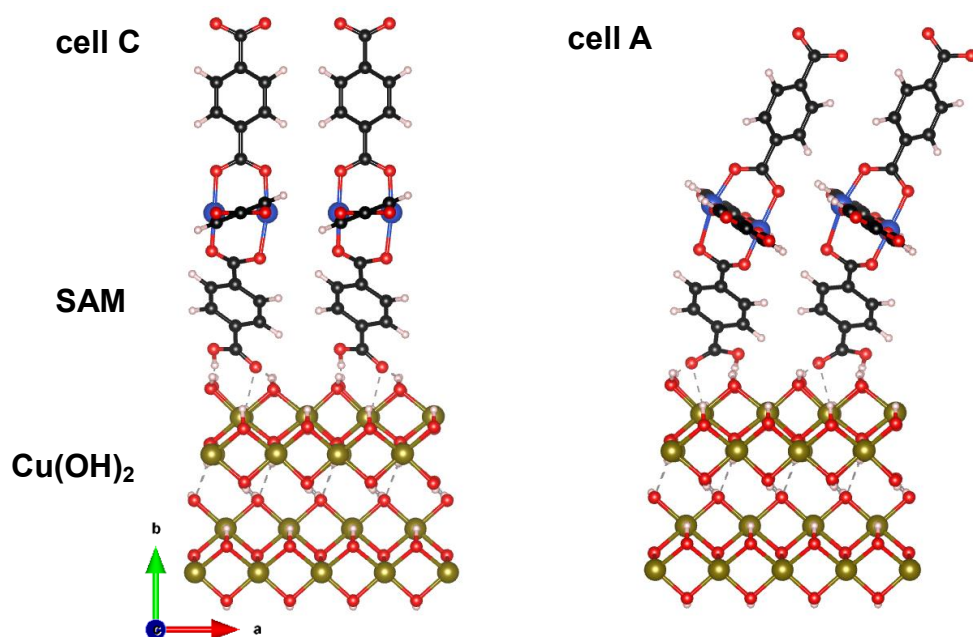


Figure 17: Hypothetic growth of a Cu(BDC)-MOF linked to a SAM of BDC on Cu(OH)<sub>2</sub> substrat; left: upright cell C, right: tilted cell A.

Due to a self-assembling monolayer of BDC molecules on the a-surface of the Cu(OH)<sub>2</sub> nanobelts, a MOF-structure could be stabilized that is not necessarily the bulk structure of a Cu(BDC)-MOF. However, simulations of bigger systems also including a part of the framework to further investigate the heteroepitaxial growth have yet to be done.

## 6 FRET in a Zn-SURMOF

### 6.1 Background and Motivation

The theoretical work on Förster energy transfer as well as this introduction is based on the experimental findings of R. Haldar et al.<sup>57</sup>. The structure of interest belongs to the Zn-SURMOF-2 structure type.<sup>21</sup> This MOF-type is based on  $Zn^{2+}$ -paddle-wheel units, which are connected via carboxylic groups to organic linkers to form an array of square grid type 2D sheets. For better experimental control of the orientation of the MOF, it is grown on OH-functionalized quartz or silicon substrates by alternating deposition of organic linkers and metal-ions (liquid phase epitaxy). A schematic representation of the framework is depicted in Figure 18.

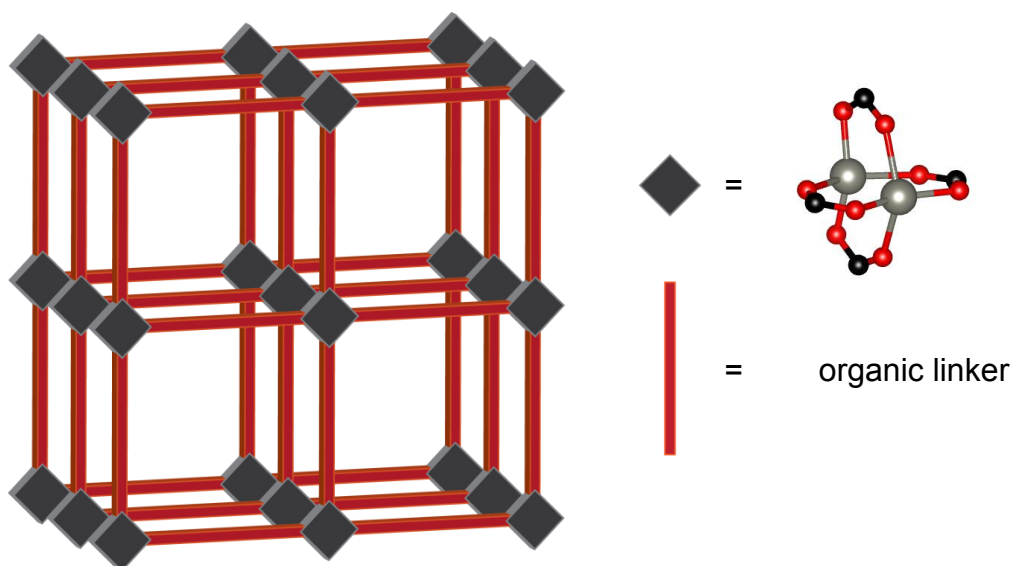


Figure 18: Schematic structure of SURMOF-2, grey=Zn-paddlewheel-node, red=organic linker.

The work of R.Haldar et al. focuses on Förster resonance energy transfer (FRET) and excited state dynamics. 4,4'-(anthracene-9,10-diyl) dibenzoic acid (ADB) was used as organic linker being able to act as donor for energy transfer. To investigate the exciton transport properties, a mixed SURMOF was built by doping with 0.1 - 4% of a suitable FRET acceptor (2,5-bis(butyl)-3,6-bis(4-carboxylicphenyl-4-yl)-2,5-dihydropyrrolo[3,4-c]pyrrole-1,4-dione, or DPP) as a second organic linker (Figure 19). XRD-data suggests that varying the linker does not affect the resulting unit cell due to similar lengths of both chromophores.

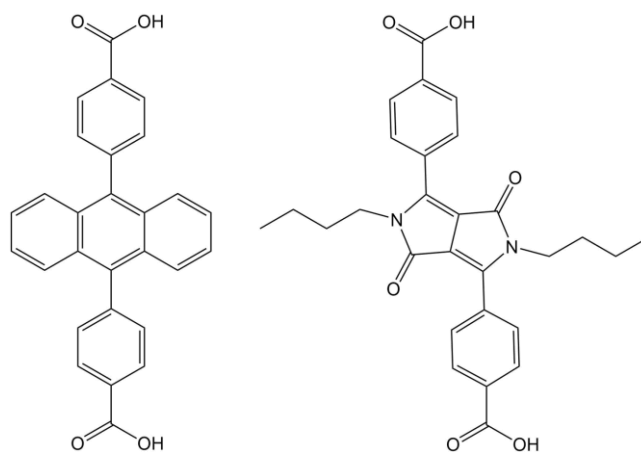


Figure 19: Skeletal formula of the organic linkers ADB(left) and DPP(right).

Time-resolved spectroscopy experiments suggest that photon absorption of the Zn-ADB-SURMOF creates two distinct excited states, which show different energy migration behaviours. The first PL component,  $PL_{\text{mon}}$ , with a lifetime of 1.2 ns belongs to the excited state of one ADB unit. The second component,  $PL_{\text{exm}}$ , with a rise time of 80 ps and a lifetime of 4 ns is related to the formation of an excimer state among several ADB units along the inter-sheet direction. This excimer formation is supposedly enabled by rotation of the anthracene moiety of ADB, which reduces the distance between the ADB units. To investigate the diffusion of the two excited states, the efficiency of the quenching by DPP of both states was determined in two different MOF-structures. The first structure was a Zn-ADB MOF randomly doped with DPP. In this framework 40% of the transferred energy was determined to come from excited monomer states, while 60% come from excimer states. In the second structure, multiple layers of undoped Zn-ADB were grown on top of the first structure. In this bilayer-structure, the excitation occurs in the ADB top layers. As the top layers contain solely ADB, inter-sheet transport of the excitation in the top layers does not result in quenching by DPP. Instead, the excitation has to travel downward intra-sheet (perpendicular to the inter-sheet) to the DPP containing layers. Indeed, the quenching efficiency of the inter-sheet oriented  $PL_{\text{exm}}$  is decreased from 60 % to 20% depending on the layer thickness. Due to the low quencher concentrations (max. 4 %) this change in efficiency can be attributed to the energy transport solely between ADB units. Therefore, R. Haldar et al. concluded that  $PL_{\text{exm}}$  favourably migrates along the inter-sheet direction, whereas  $PL_{\text{mon}}$  shows diffusion in all directions. The aim of this thesis is to model the Förster resonance energy transfer between the ADB units and thus, gain insight into its directionality.

## 6.2 Computational Details

This section contains technical details about the computation as well as the validation of the methods used. In the further course of the work the term “molecule” is used to describe only the organic compound, whereas “monomer” always describes the combination of one organic linker with its connected metal nodes.

### 6.2.1 Molecular calculations

The organic linkers (ADB and DPP) and their excited state properties were characterised using the program ORCA 4.<sup>58</sup> The ground and excited states of the molecules were optimized on the DFT level of theory with the PBE,<sup>41</sup> PBE0<sup>44</sup> and CAM-B3LYP<sup>59</sup> functionals with def2-TZVP basis set<sup>47</sup> and Grimme’s D3 dispersion correction.<sup>51</sup> Solvent effects of ethanol were included using the SMD continuum solvation model ( $\epsilon=24$ )<sup>60</sup> for all molecular calculations. The absorption and emission spectra of the relaxed structures in solution were computed with TD-DFT using the same three functionals (PBE, PBE0 and CAM-B3LYP, respectively) and the def2-TZVP basis set taking 15 excitations into account. Frequencies were calculated numerically in ethanol (SMD).

Secondly, molecular calculations concerning only the anthracene moiety of ADB were done as a test system. For this, the ground and first excited state of the molecule anthracene was optimized with PBE0 with the def2-TZVP basis set and Grimme’s D3 dispersion correction. The absorption and emission properties were calculated with TD-DFT with the same functional and basis set taking 15 excitations into account.

### 6.2.2 Workflow for the calculation of FRET in MOFs

The bulk structure of MOFs may be strongly influenced by steric hindrance between the linkers, for instance in the present case of a layered 2D-MOF. Thus, the geometry of the incorporated linkers likely differs from their geometry as solvated molecules. Simple molecular simulations will, therefore, not accurately represent the ground and excited state geometries of the linkers. However, as excited state optimizations are not feasible periodically for systems as large as the present ones, excitation properties have to be gained via molecular calculations. The chosen approach combines three types of calculations:

- Periodic calculations

Periodic calculations give insight into the geometric structure of the MOF.

- Oligomer calculations

Oligomers consisting of three (trimers) and four (tetramers) building blocks are cut out of the periodic bulk structure to simulate an excitation situation in the bulk of the MOF. Free coordination sites of the metal-ions are saturated with acetate units. Such oligomers should ensure the accurate description of the MOF-structure during optimization, especially along the direction with the shortest intermolecular-distance, which is assumed to also contribute the most to intermolecular interactions.

- Monomer calculations

After optimization of the oligomers, single building blocks (called monomers), which resemble bulk geometry, are extracted from the clusters. For consistency in this work, the monomers are obtained from the central unit of the trimers. The monomer cut out of the ground state optimized trimer is used as the acceptor (absorption). The monomer cut out of the  $S_1$  optimized trimer is used as the donor (emission). The transition density between the ground and first excited state is obtained from single point TD-DFT calculations for those monomers. After the TD-DFT calculation, the transition density is generated as a Gaussian cube-file format by the routine *orca\_plot* (grid resolution = 80x80x80). The calculated vertical absorption and emission spectra are visualized by the routine *orca\_asa*. The Coulombic coupling is then estimated applying the Transition-

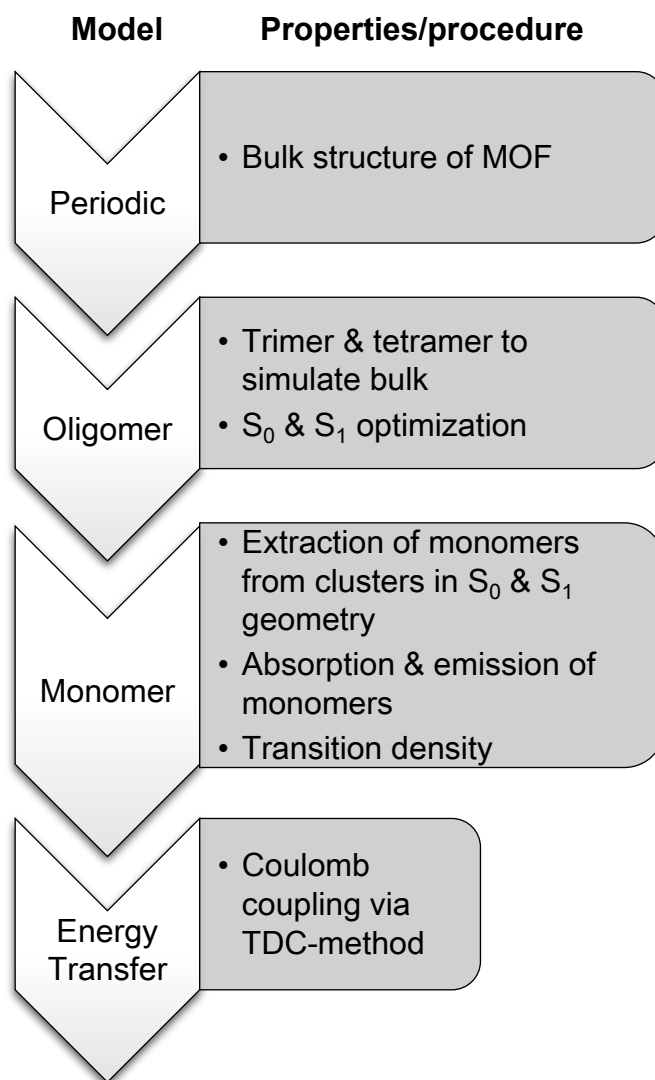


Figure 20: Workflow proposed for the calculation of FRET in MOFs.



Density-Cube (TDC) method with the ADB ground state as acceptor and the first excited state as donor. The method is implemented in a homemade code described in the *Appendix A2*. Essentially, the transition density cube files of the respective monomers are translated to the positions of the organic linkers in the periodic MOF structure and the coupling is calculated according to Eq.11.

The procedure described above is visualized in the workflow-scheme of Figure 20. In all oligomer and monomer units the  $Zn^{2+}$  ions were coordinatively saturated with acetate units to ensure the paddlewheel structure of the metal node. In difference to the molecular calculations of the organic linkers ADB and DPP in EtOH (vide supra), all other calculations were done in the gas-phase. Solvent effects were not accounted for as experimental data suggests solvent free pores of the MOF.<sup>57</sup>

### 6.2.3 Periodic calculations

The bulk structure of the Zn-ADB-MOF was calculated with FHI-Aims.<sup>61</sup> The Perdew–Burke-Ernzerhof (PBE)<sup>41</sup> functional with van der Waals correction (Tkatchenko-Scheffler method<sup>50</sup>) was used with a 2x2x8 k-point grid and *Tight* settings of the numeric atom-centered basis set. A detailed description of the basic functions used in this program-internal basis set is given in the *Appendix A3*. The atomic ZORA approximation was applied for relativistic treatment. Starting from the XRD-data provided by R. Haldar et al.,<sup>57</sup> the atom positions within the cell were optimized fixing the cell parameters to ensure the tetragonal character of the unit cell.

### 6.2.4 Oligomer calculations

For all calculations of oligomers (trimers and tetramers) the PBE0 hybrid functional with def2-SVP basis set and Grimme's D3 dispersion correction was applied as implemented in ORCA 4. The  $Zn^{2+}$  ions were coordinatively saturated with acetate units (charge = 0, mult. = 1). The ground state as well as the first excited state was optimized keeping the Cartesian coordinates of the Zn- and O-atoms fixed to the values obtained in the periodic calculations. Then, the absorption and emission spectra of these structures were calculated. All TD-DFT calculations were done taking 5 excited states into account.

### 6.2.5 Monomer calculations

The central units of the PBE0/def2-SVP optimized trimers in  $S_0$  and  $S_1$  state geometry were extracted. Such monomers contain one ADB molecule connected on both ends to a saturated Zn-paddle wheel (charge = 0, mult. = 1). On these structures TD-DFT calculations with the PBE0 hybrid functional using the def2-TZVP basis set were

performed taking 5 excited states into account. The transition densities from the ground to the first excited state for the absorption ( $S_0^{\text{opt,cut}} - S_1^{\text{vert}}$ ) and for the emission ( $S_1^{\text{opt,cut}} - S_0^{\text{vert}}$ ) were obtained using the routine *orca\_plot* provided by ORCA 4.

## 6.2.6 Benchmarking of the functional

A good choice of the DFT functional can be crucial for the correct description of the excited state properties of a molecule. The molecular calculations in ethanol (SMD) with the def2-TZVP basis set were used to benchmark the results of three common functionals (PBE, PBE0 and CAM-B3LYP) against the experimental spectra of ref.57. The calculated absorption and emission energies for the first excited state of the chromophores ADB and DPP are compared to the experimental  $\lambda_{\text{max}}$  values of the two molecules dissolved in ethanol in Table 5. In comparison, PBE0 seems to describe the first excited state of the molecules better than CAM-B3LYP, which overestimates the experiment by about 0.3 eV. The deviations of the PBE-energies do not show a constant trend and differ between 0.1 and 0.6 eV. Excited state calculations with PBE were, thus, found to be not necessarily reliable. Therefore, PBE0 was the functional of choice for the further computation of excited state properties.

Table 5:  $S_1$  absorption and emission data of ADB and DPP calculated with two hybrid-functionals (PBE0 and CAM-B3LYP) and a GGA-functional (PBE) in ethanol (SMD) in comparison with experiment ( $\lambda_{\text{max}} = 380 \text{ nm}$ ).

	PBE0 [eV]	CAM-B3LYP [eV]	PBE [eV]	Experiment <sup>57</sup> [eV]
ADB abs	3.347	3.641	2.985	3.3
ADB em	2.741	3.063	2.871	2.9
DPP abs	2.791	3.219	2.054	2.6
DPP em	2.412	2.642	1.885	2.2

## 6.2.7 Benchmarking of the basis set

Especially for the computation of bigger systems, the question of CPU-time is omnipresent. A combination of functional and basis set is favoured that produces good results in an acceptable amount of time. In the present case, such a combination is searched for the geometry optimization of the oligomers and the subsequent calculation of the transition densities of the extracted monomers.

For this, one monomer unit was fully optimized with two different functionals (PBE and PBE0) at the def2-SVP and def2-TZVP levels of theory applying Grimme's D3 dispersion correction. Then, the absorption spectra of these structures with 5 excited states were calculated. For all TD-DFT calculations PBE0 was used, assuming that this functional gives a good description of the excitation properties according to the validation above.

Table 6 summarizes the different calculations with the functionals and basis sets used, as well as their abbreviations used throughout this chapter.

Table 6: Combinations of functionals and basis sets used.

Optimization	Absorption	Abbreviation
PBE/def2-TZVP	PBE0/def2-TZVP	PBE0//PBE
PBE0/def2-SVP	PBE0/def2-SVP	SVP//SVP
PBE0/def2-SVP	PBE0/def2-TZVP	TZVP//SVP
PBE0/def2-TZVP	PBE0/def2-TZVP	TZVP//TZVP

The PBE0 geometries with the two basis sets as well as the PBE/def2-TZVP geometry are characterized in Table 7 by their bond lengths and angles. Optimization with PBE/def2-TZVP leads to a 6° smaller Ant/Ph angle and to shorter bond lengths compared to the PBE0/def2-TZVP geometry. In Figure 21 the triple-zeta geometry of PBE0 (black) lies on top of the double-zeta one (orange), showing the small changes in the anthracene-phenyl angle of about 4°. The bond lengths do almost not differ between the two different basis sets for the PBE0 optimizations.



Figure 21: PBE0 optimized structures of a monomer with two different basis sets; orange = def2-SVP, black = def2-TZVP.

Table 7: Geometrical data of PBE0 optimized structures at the def2-SVP and def2-TZVP level and of a PBE optimized structure at def2-TZVP level, bond lengths: B1 = phenyl-carboxylate, B2 = phenyl-anthracene.

	PBE0		PBE
	def2-SVP	def2-TZVP	def2-TZVP
Ant/Ph [°]	84.16	80.69	74.32
Zn/Ant [°]	84.30	81.97	73.35
Zn/Ph [°]	0.14	1.28	0.97
B1 [Å]	1.511	1.511	1.508
B2 [Å]	1.507	1.508	1.504

The absorption spectra for the monomers are shown in Figure 22. As the  $S_0$ - $S_1$  transition is only localized on the organic linker, it seems justified to benchmark the absorption energies to the experimental value of the ADB molecule (Table 8). The shift due to the

solvent for the  $S_0$ - $S_1$  excitation is calculated to be 0.007 eV for all methods and should not interfere in the comparison.

Table 8: Vertical absorption energies of four methods used in the gas phase benchmarking compared to the experimental value from ref.57.

method	absorption ( $S_0$ - $S_1$ ) [eV]
PBE0//PBE	3.230
SVP//SVP	3.436
TZVP//SVP	3.353
TZVP//TZVP	3.375
experiment	3.3

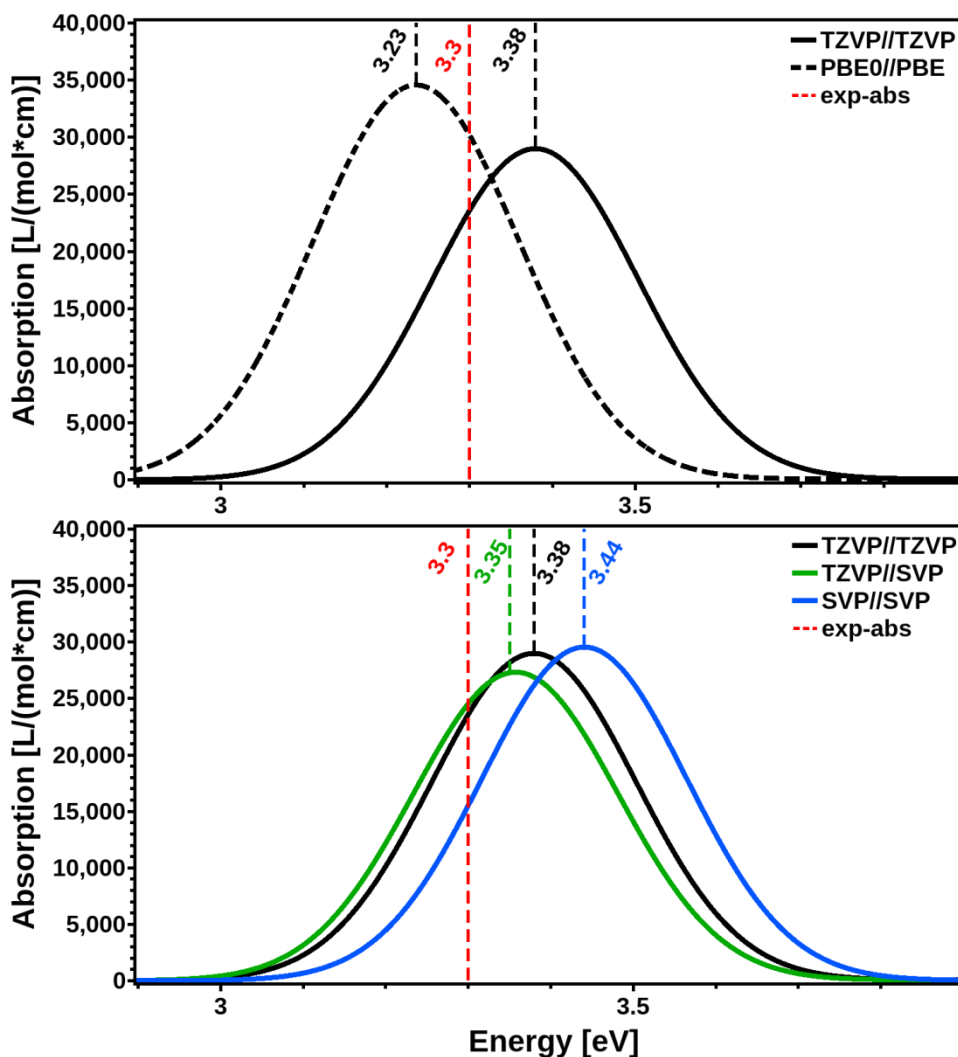


Figure 22: Absorption spectra of an ADB monomer optimized with two different basis sets (def2-SVP and def2-TZVP) at PBE0+D3 and with def2-TZVP at PBE+D3 level of theory, TD-DFT in all calculations with PBE0; FWHM=0.3 eV as taken from experimental spectra.<sup>57</sup>

The absorption energies of the PBE/def2-TZVP and PBE0/def2-TZVP optimized structures differ by about 0.15 eV. As the TD-DFT calculations were all done with PBE0/def2-TZVP, the difference is due to the different functional in the geometry optimization. This shows that the choice of the functional for the initial geometry optimization affects the excitation properties. However, both functionals perform equally well. While the vertical absorption

energy for the PBE structure is underestimated by 0.07 eV, the energy of the PBE0 structure is overestimated by 0.08 eV. The hybrid functional PBE0 was chosen for the oligomer calculations to consistently calculate the geometry and the excitation properties with the same functional.

The influence of the basis set on the PBE0 geometry optimization can be seen comparing the TZVP//SVP and TZVP//TZVP calculations and is 0.03 eV. Comparing the TZVP//SVP and SVP//SVP calculations shows the deviation of the absorption energy, which is 0.1 eV, due to a change of the basis set for the TD-DFT calculation. The TZVP//TZVP as well as the TZVP//SVP PBE0 excitation energies agree well with the experimental value of 3.3 eV. This means, a smaller basis set can be used for the optimization of the structure without influencing the absorption spectrum, but the spectrum itself should be calculated with a triple-zeta basis set.

Therefore, the extraction of the monomers from PBE0 clusters at the def2-SVP level should be acceptable for the calculation of the excitation properties at the def2-TZVP level.

## 6.3 Results and Discussion

In experiment, the acceptor molecule DPP is essentially used to monitor the transfer process. However, due to the small concentration of DPP, the rate determining step of the energy transfer is most likely the transfer between two donor molecules (ADB) until the exciton is spatially close enough to interact with DPP. Thus, the following theoretical investigation of energy transfer in Zn-SURMOF2 focuses on the interaction between the ADB linkers and does not yet include the coupling between the actual donor and acceptor.

### 6.3.1 Molecular simulations

By optimizing one ADB molecule in solution, two different conformational isomers can be found, differing in the relative orientation of the phenyl groups relative to the anthracene system. The conformer with both phenyl rings oriented in the same direction will further be called *cis*. The other conformer will correspondingly be called *trans*, as the phenyl rings are oriented in opposing directions. The different orientation of the phenyl rings results in different symmetries. While the *cis*-conformer shows a mirror plane through the long axis of the anthracene moiety, this is the axis of rotation in the case of the *trans*-conformer. To visualize the difference, a projection along the long molecular axis of ADB is shown in Figure 23.

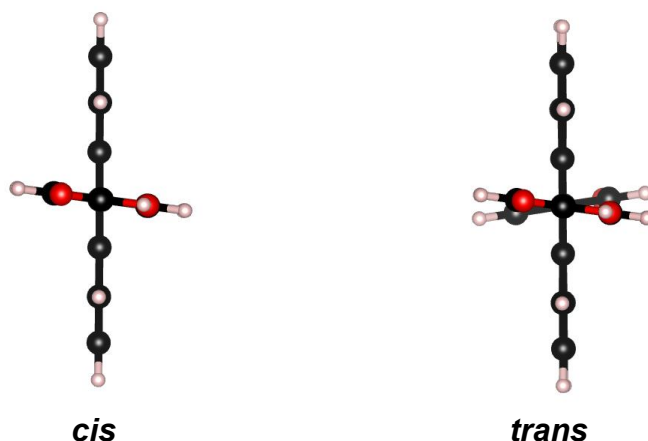


Figure 23: Projection of the two conformational isomers of ADB along the long molecular axis optimized with PBE0+D3/def2-TZVP in ethanol; *cis* (left), *trans* (right).

Frequency calculations confirm the stability of both isomers. Considering  $\Delta G$  at room temperature shows a  $\Delta\Delta G$  of 0.19 kJ/mol favouring the *cis*-phase. This difference is 13 times smaller than the energy available at 25°C ( $k_B T$ ). Thus, both conformers can be seen as equally stable. According to the dynamic equilibrium approach<sup>62</sup> this energy difference results in a 1:1 ratio of the isomers in solution.

### 6.3.2 Absorption and emission of ADB molecule

The angles between the phenyl and the anthracene moiety as well as between both phenyl rings are representative for each conformation. As a second characteristics, the bond lengths B1 and B2 are chosen, which connect the phenyl ring to the carboxyl group (B1) and the anthracene (B2), respectively. A schematic depiction of the bond lengths is shown in Figure 24.

Optimization of the first excited state leads to a flattening of the anthracene-phenyl angle in the *cis*- and the *trans*-phase as shown in Table 9 and therefore to a stronger interaction between the aromatic systems. As a consequence, the angle between the phenyl rings in the *trans*-phase becomes steeper. The bond lengths of B1 and B2 are shortened with respect to the ground state and thus, indicate the formation of a quinoid-like structure, as is expected for this system. This is confirmed by the general bond length change upon relaxation of the  $S_1$  state (see *Appendix A1.3*). To visualize the conformational change, the  $S_1$  geometry (orange) is shown on top of the ground state geometry (black) in Figure 25.

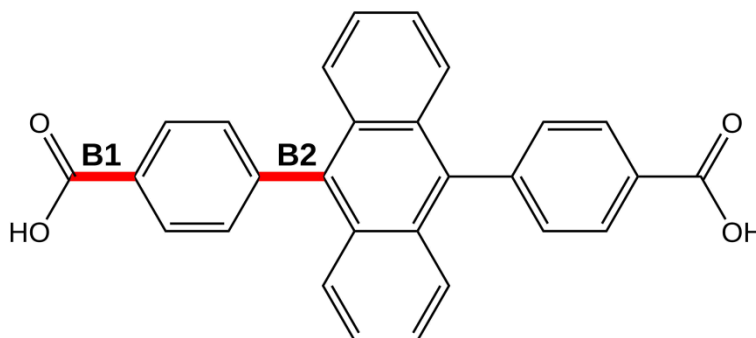


Figure 24: Skeletal formula of ADB with bonds B1 and B2 shown in red.

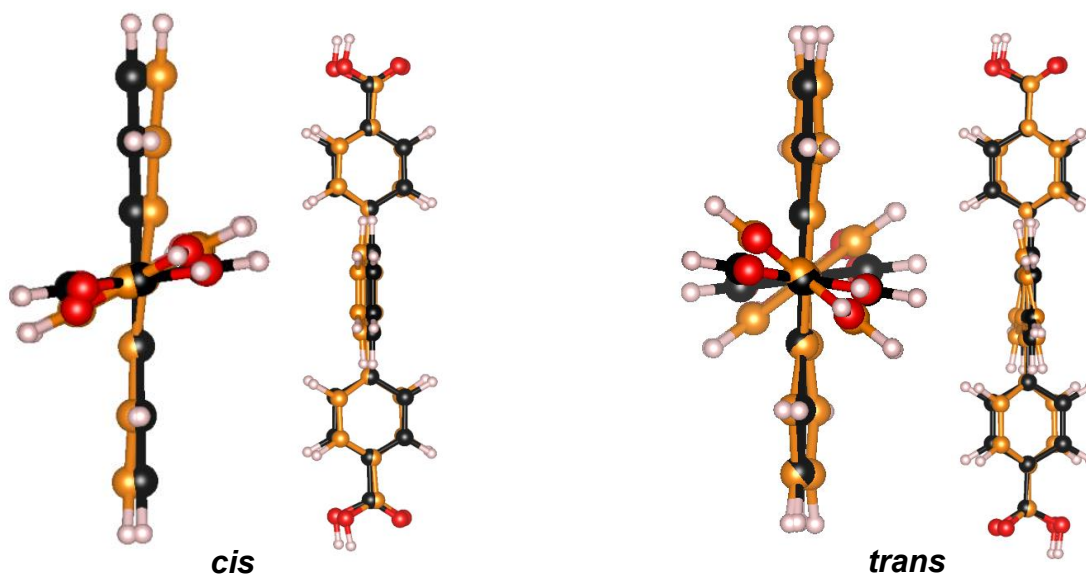


Figure 25:  $S_0$  (black) and  $S_1$  (orange) geometry of the *cis* (left) and *trans*-phase (right) after PBE0+D3/def2-TZVP optimizations in ethanol.

Table 9: Relevant conformational data of the  $S_0$  and  $S_1$  geometry for both phases after PBE0+D3/def2-TZVP optimizations in ethanol as well as their relative energies.

	<i>cis</i>		<i>trans</i>	
	$S_0$	$S_1$	$S_0$	$S_1$
Anth/Ph [°]	81.97	58.75	81.72	53.91
Ph/Ph [°]	0.34	1.03	16.71	76.81
COOH/Ant [°]	82.17	59.79	81.80	54.94
COOH/Ph [°]	0.21	1.04	0.12	1.03
B1 [Å]	1.479	1.469	1.479	1.469
B2 [Å]	1.485	1.462	1.485	1.460
rel. $E_{el}$ [kJ/mol]	0.0	111.7	$4 \cdot 10^{-3}$	113.2
$\Delta\Delta G$ [kJ/mol]	0.0	-	0.2	-

The excitation properties of the molecule in both conformations were investigated focusing on the  $S_0$ - $S_1$  transition relevant for the energy transfer.

The absorption and emission spectra are shown in Figure 26 with the excitation energies and oscillator strengths listed in Table 10. Table 10 also shows the corresponding transition densities. The transition dipole points along the long molecular axis. As visible in the almost identical spectra, the excitation properties of the two conformers do not differ much for low lying excitations. A list of the prominent peaks for both conformers as well as the involved molecular orbitals is given in the *Appendix A1.2*. The experimental excitation energies in ethanol are 3.4 and 2.9 eV for the  $S_1$  absorption and emission ( $\lambda_{ex} = 380$  nm), respectively. The calculated vertical absorption correlates well with the experimental data within 0.05 eV, the vertical emission is underestimated by about 0.16 eV.

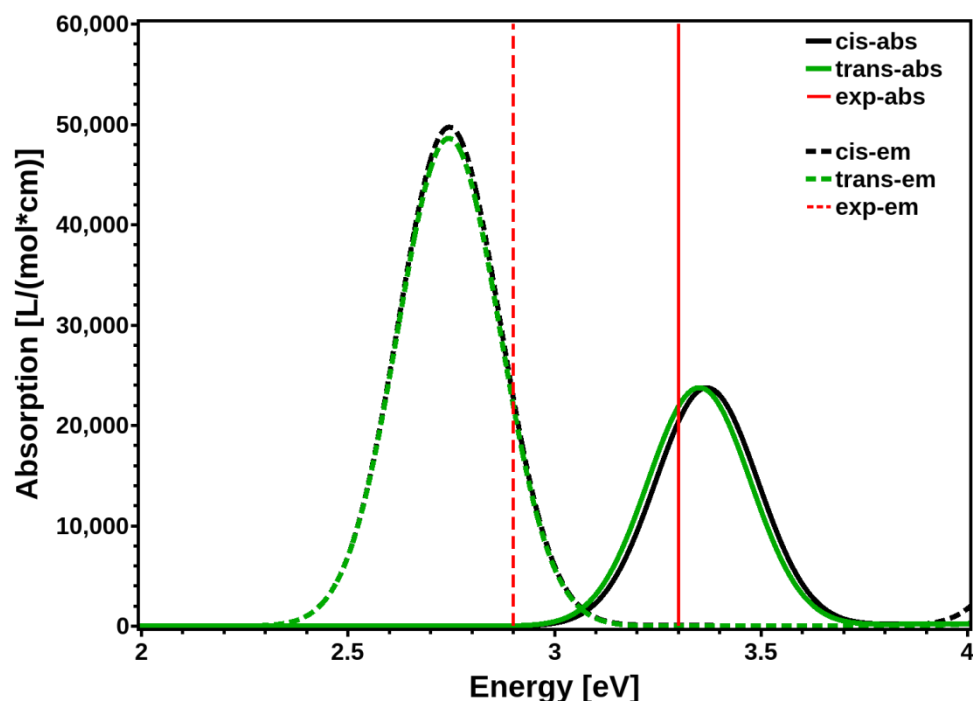
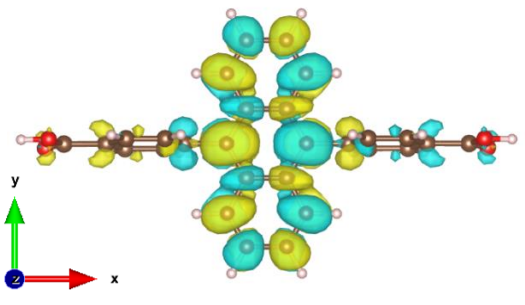
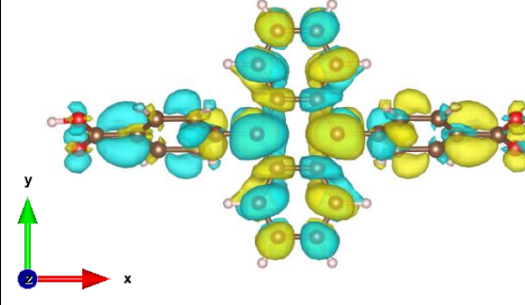
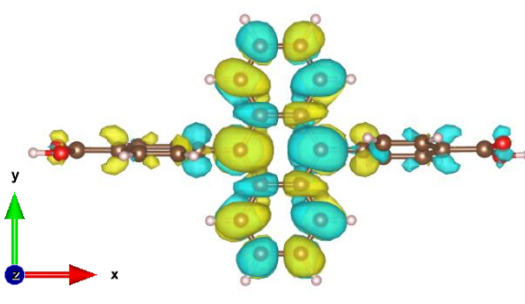
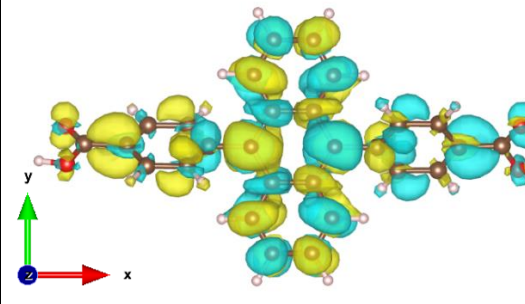


Figure 26: Vertical absorption and emission spectra of the *cis* and *trans*-conformer of ADB molecule according to TD-DFT calculations (PBE0/def2-TZVP) in ethanol compared to  $\lambda_{max}$  of experimental spectra from ref.57; FWHM=0.3 eV as taken from experimental spectra.<sup>57</sup>



Table 10: PBE0+D3/def2-TZVP excitation energies  $E_{ex}$ , oscillator strengths  $f_{osc}$ , transition dipoles  $\mu_{tr}$  and transition densities of  $S_0$ - $S_1$  transitions of cis and trans-conformer according to TD-DFT calculations in ethanol.

<b>cis</b>	<b>abs</b>			<b>em</b>		
						
	$E_{ex}$ [eV] ( $f_{osc}$ )	$\mu_{tr}^2$ [au <sup>2</sup> ]	$\begin{pmatrix} \mu_{tr,x} \\ \mu_{tr,y} \\ \mu_{tr,z} \end{pmatrix}$ [au]	$E_{ex}$ [eV] ( $f_{osc}$ )	$\mu_{tr}^2$ [au <sup>2</sup> ]	$\begin{pmatrix} \mu_{tr,x} \\ \mu_{tr,y} \\ \mu_{tr,z} \end{pmatrix}$ [au]
3.365 (0.255)	3.09	$\begin{pmatrix} 1.76 \\ 0.00 \\ 0.01 \end{pmatrix}$	2.739 (0.538)	8.01	$\begin{pmatrix} -2.83 \\ 0.00 \\ -0.01 \end{pmatrix}$	
<b>trans</b>	<b>Abs</b>			<b>em</b>		
						
	$E_{ex}$ [eV] ( $f_{osc}$ )	$\mu_{tr}^2$ [au <sup>2</sup> ]	$\begin{pmatrix} \mu_{tr,x} \\ \mu_{tr,y} \\ \mu_{tr,z} \end{pmatrix}$ [au]	$E_{ex}$ [eV] ( $f_{osc}$ )	$\mu_{tr}^2$ [au <sup>2</sup> ]	$\begin{pmatrix} \mu_{tr,x} \\ \mu_{tr,y} \\ \mu_{tr,z} \end{pmatrix}$ [au]
3.347 (0.250)	3.04	$\begin{pmatrix} 1.75 \\ -0.01 \\ -0.01 \end{pmatrix}$	2.738 (0.526)	8.00	$\begin{pmatrix} 2.83 \\ -0.01 \\ -0.02 \end{pmatrix}$	

### 6.3.3 Periodic simulations

Starting from the isomeric mixture of ADB in solution, the synthesis possibly leads to the equal incorporation of the *cis*- and *trans*-conformers into the MOF resulting in two different phases. XRD data<sup>57</sup> suggests a tetragonal unit cell as shown in Table 11. Therefore, both conformers were fitted into the experimental unit cell and found to be stable.

The relaxed structures are shown in Figure 27. In the periodic framework, two additional angles can be introduced indicating the relative orientation of the Zn-plane to the phenyl rings and the anthracene, respectively. A full angle-analysis of both phases is provided in Table 12.

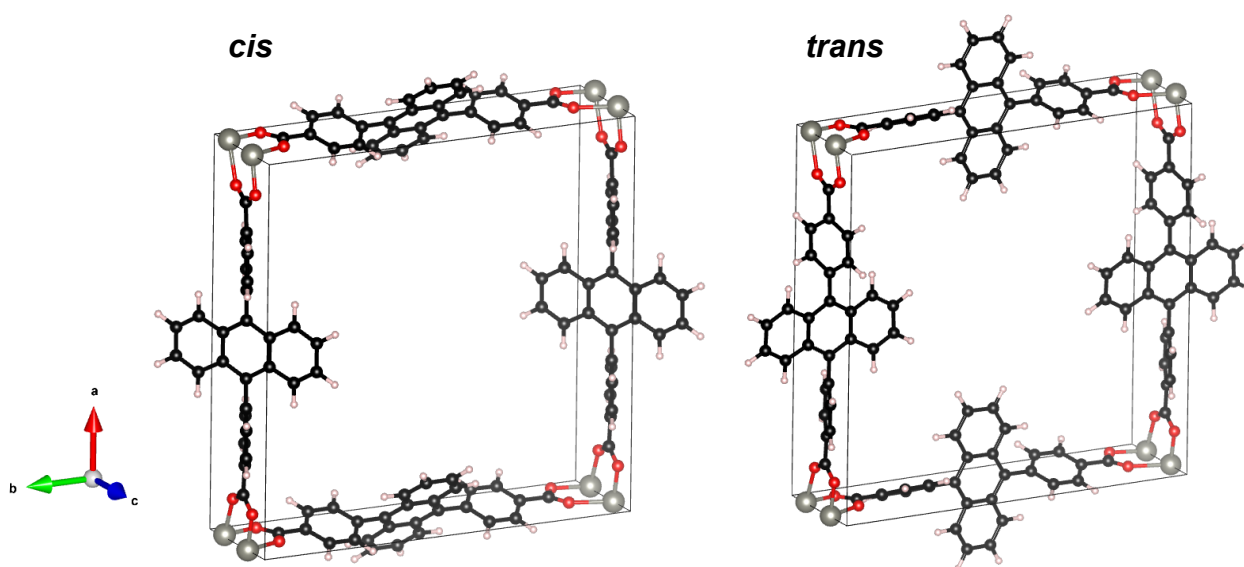


Figure 27: Atomic positions after relaxation of the two MOF-phases (PBE+TS/tight) in the fixed experimental unit cell; *cis* (left), *trans* (right).

Table 11: Cell parameters of the experimental unit cell taken from ref.57.

cell constants	
a	19.803 Å
b	19.803 Å
c	5.819 Å
$\alpha=\beta=\gamma$	90°

Table 12: Angles of the two MOF-phases of the periodic PBE+TS/tight optimization compared to the molecular PBE0+D3/def2-TZVP calculations.

	periodic		molecule	
	<i>cis</i>	<i>trans</i>	<i>cis</i>	<i>trans</i>
Anth/Ph [°]	66.30	69.61	81.97	81.72
Ph/Ph [°]	0.72	45.12	0.34	16.71
Zn/Ant [°]	42.33	88.03	82.17*	81.80*
Zn/Ph [°]	24.02	22.40	0.21*	0.12*
B1 [Å]	1.509	1.511	1.479	1.479
B2 [Å]	1.507	1.507	1.485	1.485
rel. Energy [kJ/mol]	0.00	60.97	0.00	0.04

\*as Zn atoms are missing, the angles are measured relative to the COOH-plane

In difference to the solution, the *cis* and *trans*-phase of the MOF are not energetically equal. The *cis*-phase is 61 kJ/mol (0.6 eV) more stable than the *trans*-phase. The energetics suggest that the bulk of the Zn-ADB MOF consists of the *cis*-phase.

The change of the bond length from the molecular to the periodic calculations can most likely be attributed to the fixed experimental unit cell, in which the molecules were put. The fixed lattice constants enforced an elongation of the bond length.

Upon incorporation of the *cis* as well as the *trans*-conformer into the 3D framework the angle between the anthracene and the phenyl rings decreases by about 15°. The phenyl rings tilt out of the Zn-plane by about 23°. Both changes of rotation are due to the tight packing in the framework in contrast to a solution. However the question arises, which forces are responsible for the rotational changes of the linkers upon incorporation.

To get a first idea, the atomic positions were relaxed with and without van der Waals correction in the periodic calculations. Figure 28 shows a projection of the unit cell along the *c* axis. Structures relaxed without van der Waals correction are shown in orange, structures relaxed applying van der Waals correction are shown in black. In both cases, vdW forces do not affect the phenyl rings, suggesting that their rotational conformation is due to the steric repulsion of the neighbouring linker units. The rotation of the anthracene in the *cis*-conformation is mainly due to attractive dispersion forces. The anthracenes in *trans*-conformation seem to be too far apart in the *c* axis to influence each other or are rather fixed in their position due to sterical hindrance by the phenyl rings.

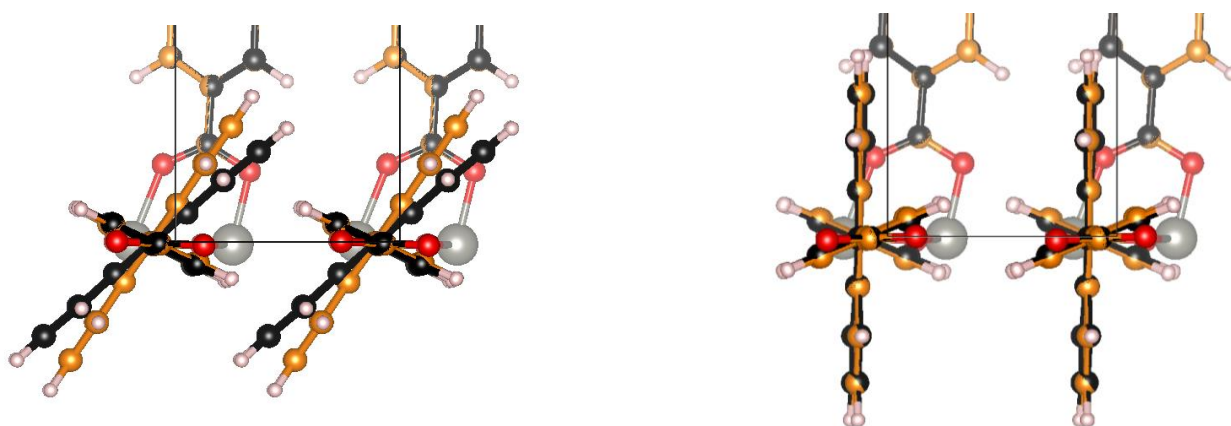


Figure 28: Projection of the unit cell relaxed with (black) and without (orange) van der Waals correction (PBE+TS); cis (left), trans (right).

Note that if the conformers in one sheet (along a- and b-axis) alternately point in opposite directions, bigger unit cells would result, such as the one in Figure 29. The cell parameters of the shown cell are calculated to be  $a = b = 28.006 \text{ \AA}$  and  $c = 5.819 \text{ \AA}$ . This estimation is based on the smaller experimental unit cell from ref.57 listed in Table 11. The estimated a- and b-parameters of the cell in Figure 29 are the diagonals of the experimental cell.

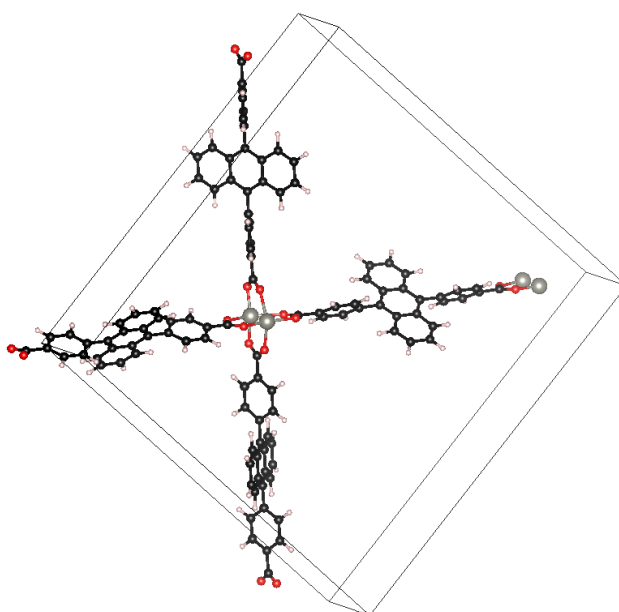


Figure 29: Constructed bigger unit cell where the conformers along the a- and b-axis alternately point in opposite directions.

### 6.3.4 Importance of adjacent linkers

The last chapter showed the conformational changes of the *cis* and *trans*-molecule upon incorporation into the MOF structure due to the adjacent linkers in inter-sheet direction. To underline the importance of the 3D framework, a monomer (one linker coordinated to paddle wheels saturated with acetates) was cut out from the periodic *cis* and *trans*-phase, respectively. It was relaxed with the coordinates of the Zn- and O-atoms fixed to the values obtained in the periodic calculations.

The geometry of the relaxed monomer is independent of the phase, as it leads in both cases to the same relaxed structure shown in Figure 30. In contrast to the periodic conformations, the relaxed monomer resembles the *cis*-molecule in solution as can be seen by the characteristic angles in Table 13. Figure 30 also compares the ground state geometry of the monomer to the optimized excited state geometry. Again, the  $S_1$  state geometry of the monomer resembles the  $S_1$  geometry of the *cis*-molecule as can be seen in Table 13. The most apparent difference of the monomer to the periodic structure is that the phenyl rings are rotated into the Zn-plane. As a consequence, the anthracene-phenyl angle increases from  $66^\circ$  in the periodic case to about  $81^\circ$  in the monomer.

This again highlights the importance of neighbouring linkers on the conformation. It simultaneously suggests that optimization of the excited state on a simple monomer basis would not accurately represent the situation in the bulk of the MOF due to the neglected influence of neighbouring linkers.



Figure 30: Relaxed Monomer of PBE0+D3/def2-TZVP optimization constraining the Zn and O coordinates in ground and excited state;  $S_0$  = black,  $S_1$  = orange.

Table 13: Geometry parameters of the ground and excited state of the *cis*-isomer in solution (PBE0+D3/def2-TZVP) and of the relaxed monomer and a *cis*-monomer cut from a tetramer (PBE0+D3/def2-TZVP).

	$S_0$			$S_1$		
	Molecule <i>cis</i>	monomer	periodic	Molecule <i>cis</i>	monomer	periodic
Ant/Ph [ $^\circ$ ]	81.97	80.69	66.30	58.75	57.36	-
Zn/Ant [ $^\circ$ ]	82.17*	81.97	42.33	58.17	57.21	-
Zn/Ph [ $^\circ$ ]	0.21*	1.28	24.02	0.66	0.47	-
B1 [ $\text{\AA}$ ]	1.479	1.511	1.509	1.469	1.498	-
B2 [ $\text{\AA}$ ]	1.485	1.508	1.507	1.462	1.483	-

\*as Zn atoms are missing, the angles are measured relative to the O-plane

### 6.3.5 Cluster approach

To gain information about excitation properties of large systems through periodic calculations is currently very time-consuming. On the other hand, geometries of the linkers obtained on a molecular basis have shown to significantly deviate from the periodic conformations. Therefore, the procedure as described in the *Workflow* was applied to get insight into the absorption and emission processes of the linkers. The optimized trimer and tetramer clusters for both conformers in their ground states are shown in Figure 32. The angles of the molecular calculations are compared to those of the periodic calculations in Table 14. B1 is the bond connecting the phenyl ring to the SBUs and B2 the bond between the phenyl and the anthracene moiety. As one can see, the *cis* conformation is reasonably well described by the cluster approximation. Concerning the angles and bond lengths the units in the middle of the clusters are in good agreement with the periodic structure. The units at the ends of the clusters are likely to experience finite size effects as they miss a neighbouring unit. As expected, they tend towards the optimized structure of the monomer, best be seen in the rotation of the phenyl rings towards the Zn-plane in Figure 32. The Zn-phenyl angle decreases from  $24.02^\circ$  in the periodic case to about  $15.23^\circ$  in the end units of the oligomer. It follows a change in the phenyl-anthracene angle and the deviation from the periodic structure.

In the case of the *trans*-isomer the situation is somewhat less promising. Optimization leads to a herringbone like arrangement of the anthracenes at variance with the periodic structure, and, therefore, the cluster approach seems to fail for the *trans*-phase. Nevertheless, one of the middle units of both *trans*-oligomers still represents the periodic geometry. The failure may result from two factors. On the one hand, the formation of the herringbone in the periodic case could just be prevented by the chosen unit cell (compare Figure 27) as it only contains one linker along the direction in question (c-axis). On the other hand, the spatial expansion of the basis set chosen for the cluster calculation could be too small enforcing fake interaction between the monomers. The def2-SVP basis set is composed of Gaussian-type orbitals, which show a faster decrease of the radial part than for instance the physical more meaningful Slater-type orbitals. Thus, they may not reach far enough into the space between the linkers.

Doubling the unit cell in z-direction has no effect on the structure. However, changing the basis set from Gaussian-type orbitals to numeric atom-centered orbitals (FHI-Aims) leads to a stabilization of the *trans*-cluster (Figure 31). This hints towards a basis set dependent error of the geometry optimization in the oligomer calculations.

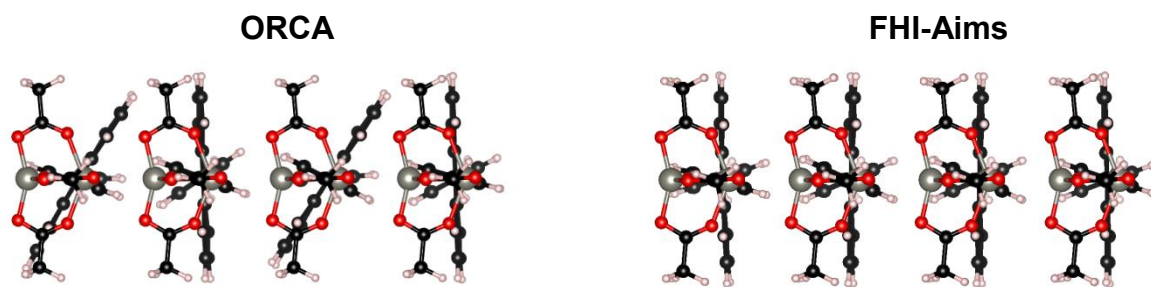


Figure 31: Structures of the trans-tetramer optimized with ORCA 4 (def2-SVP) and FHI-Aims (numeric atom-centered orbitals).

However, as FHI-Aims was not suited for the calculation of the first excited state properties in question, all quantum molecular calculations were done with ORCA. In the next step, we evaluate the first excited state optimizations of the oligomers.

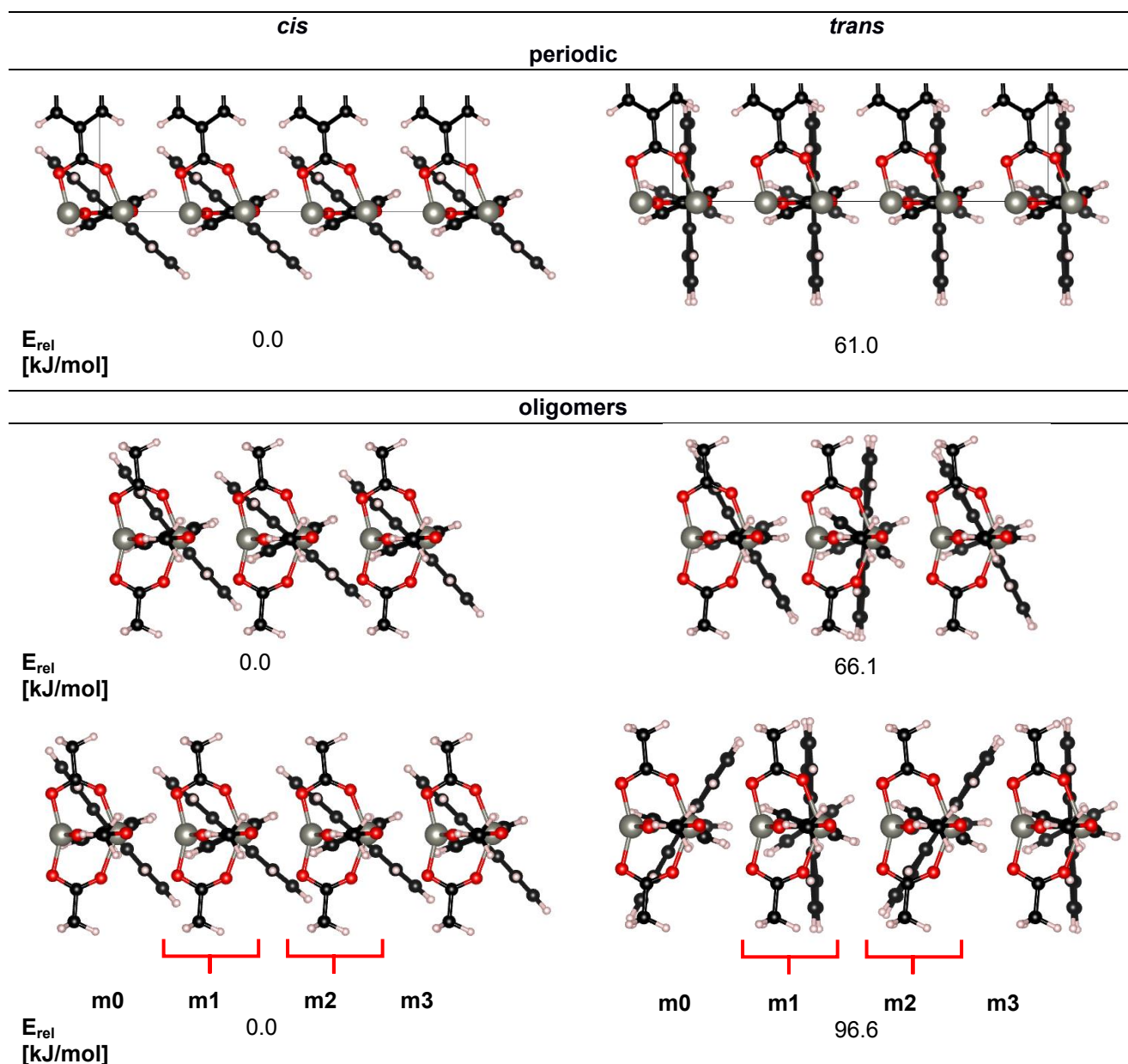


Figure 32: PBE+TS optimized periodic structures and PBE0+D3/def2-SVP optimized ground state structures of trimer and tetramer clusters of *cis* and *trans*-phase.

Table 14: Comparison of the geometry data of the trimers and tetramers of both conformers (PBE0+D3/def2-SVP) in the ground state with the periodic calculations (PBE+TS/tight); middle units of the tetramers as defined in Figure 32.

$S_0$	<i>cis</i>				<i>trans</i>			
	periodic	trimer	tetramer m1	tetramer m2	periodic	trimer	tetramer m1	tetramer m2
Ant/Ph [°]	66.30	66.36	64.93	64.07	69.61	60.39	68.39	81.97
Zn/Ant [°]	42.33	42.33	41.91	42.21	88.03	85.44	88.49	55.59
Zn/Ph [°]	24.02	24.03	23.02	21.86	22.40	34.28	20.13	26.47
B1 [Å]	1.509	1.512	1.512	1.512	1.511	1.513	1.513	1.511
B2 [Å]	1.507	1.510	1.510	1.510	1.509	1.509	1.510	1.511



In Figure 33 the clusters of the excited state optimizations are shown. Analog to the ground state analysis, Table 15 lists characteristic angles and bond lengths, however, this time they are compared to the  $S_1$  geometry of the ADB molecule. As one can see, during optimization of the first excited state the anthracene units in the clusters undergo similar rotational changes as the free molecules, meaning a decrease of the Ant/Ph angle, but not that pronounced. Furthermore, the quinoid-like structural change can be confirmed for all central units of the oligomers (see Appendix for detailed bond analysis). These are promising conditions for the extraction of reasonable  $S_1$  monomer units.

As already seen in Figure 32, the double-zeta basis set calculation of the tetrameric cluster does not represent the bulk structure of the *trans*-phase accurately. Due to the formation of a herringbone structure, one of the central units (m2) differs greatly from the bulk conformation. Despite this fact, the rotational conformation of the other central unit (m1) is in good agreement with the periodic calculation. DFT optimizations with larger basis sets were computationally too expensive, especially concerning TD-DFT calculations. Therefore, the first excited state of the *trans*-tetramer was not optimized. This leaves the best guess of an excited state geometry to the trimer cluster assuming that the central unit still represents the bulk, as it fairly does in the case of the ground state calculation as seen in Figure 32. These problems were not encountered with the *cis*-geometries, for which the middle units of all clusters are assumed to resemble a bulk situation.

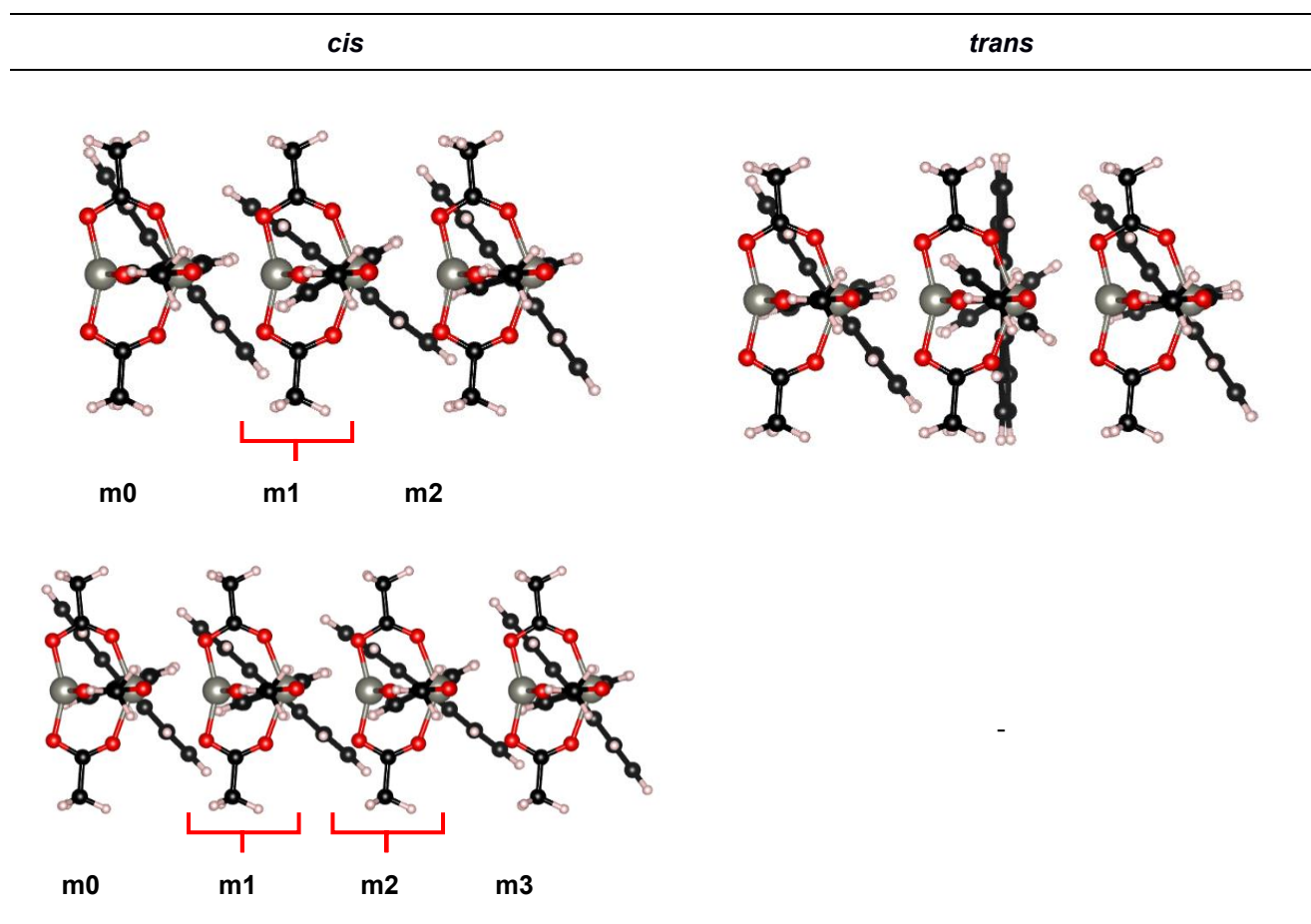


Figure 33: PBE0+D3 optimized first excited state structures of both phases.

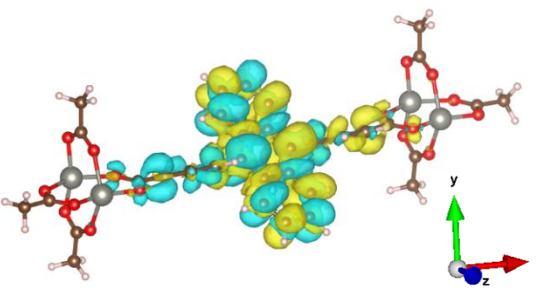
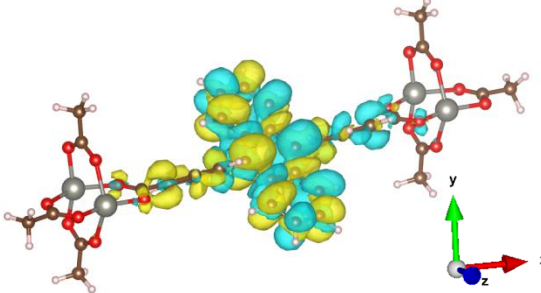
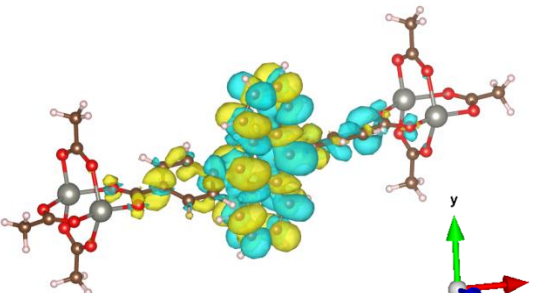
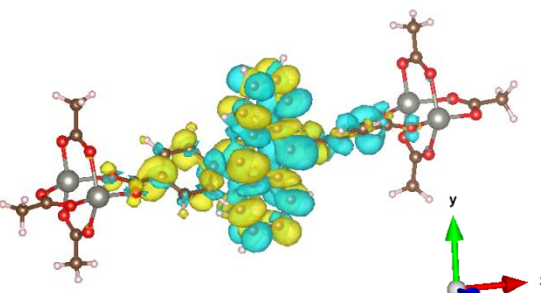
Table 15: Geometry parameters of the optimized first excited state oligomers of both phases (PBE0+D3/def2-SVP) compared to the molecule (PBE0+D3/def2-TZVP).

$S_1$	<i>cis</i>				<i>trans</i>			
	molecule	trimer m1	tetramer m1	tetramer m2	molecule	trimer m1	tetramer m1	tetramer m2
Ant/Ph [°]	58.75	66.45	60.16	62.82	53.91	53.06	-	-
Zn/Ant [°]	58.17*	38.73	42.06	38.69	53.06*	89.69	-	-
Zn/Ph [°]	0.66*	27.73	18.10	24.13	1.03*	37.43	-	-
B1 [Å]	1.469	1.520	1.500	1.518	1.469	1.499	-	-
B2 [Å]	1.462	1.506	1.498	1.505	1.460	1.490	-	-

\*as Zn atoms are missing, the angles are measured according to the COOH-plane

To be consistent, the central unit of the trimeric cluster of both phases was extracted and used for further study of the energy transport according to the *Workflow*. The cut monomer units and their relevant transition densities are shown in Table 16. Analogue to the molecules, the transition dipoles of the cut monomers point along the long molecular axis (meaning the axis between the two paddle wheels). The vertical absorption and emission energies respectively are the same for both conformers. However, the oscillator strengths of the vertical absorption and emission of the *trans*-monomer are a little bit higher than the ones of the *cis*-monomer.

Table 16: PBE0+D3/def2-TZVP excitation energies  $E_{\text{ex}}$ , oscillator strengths  $f_{\text{osc}}$ , transition dipoles  $\mu_{\text{tr}}$  and transition densities of the central monomer units extracted from trimer clusters (PBE0/def2-SVP) and used for the calculation of the Coulomb coupling.

	abs			em		
	<i>cis</i>					
$E_{\text{ex}}$ [eV] ( $f_{\text{osc}}$ )		$\mu_{\text{tr}}^2$ [au <sup>2</sup> ]	$\begin{pmatrix} \mu_{\text{tr},x} \\ \mu_{\text{tr},y} \\ \mu_{\text{tr},z} \end{pmatrix}$ [au]	$E_{\text{ex}}$ [eV] ( $f_{\text{osc}}$ )	$\mu_{\text{tr}}^2$ [au <sup>2</sup> ]	$\begin{pmatrix} \mu_{\text{tr},x} \\ \mu_{\text{tr},y} \\ \mu_{\text{tr},z} \end{pmatrix}$ [au]
3.198 (0.435)		5.55	$\begin{pmatrix} -2.36 \\ 0.00 \\ 0.02 \end{pmatrix}$	2.899 (0.558)	7.85	$\begin{pmatrix} 2.80 \\ 0.00 \\ -0.02 \end{pmatrix}$
<i>trans</i>						
	$E_{\text{ex}}$ [eV] ( $f_{\text{osc}}$ )	$\mu_{\text{tr}}^2$ [au <sup>2</sup> ]	$\begin{pmatrix} \mu_{\text{tr},x} \\ \mu_{\text{tr},y} \\ \mu_{\text{tr},z} \end{pmatrix}$ [au]	$E_{\text{ex}}$ [eV] ( $f_{\text{osc}}$ )	$\mu_{\text{tr}}^2$ [au <sup>2</sup> ]	$\begin{pmatrix} \mu_{\text{tr},x} \\ \mu_{\text{tr},y} \\ \mu_{\text{tr},z} \end{pmatrix}$ [au]
	3.130 (0.474)	6.18	$\begin{pmatrix} 2.49 \\ 0.01 \\ 0.00 \end{pmatrix}$	2.866 (0.563)	8.02	$\begin{pmatrix} -2.83 \\ -0.02 \\ -0.01 \end{pmatrix}$

In Table 17, the vertical absorption and emission energies of the cut monomers (TZVP//SVP) are compared to the calculated excitation energies of the molecule in ethanol (TZVP//TZVP, SMD) and the experimental values from ref.57. Ref.57 investigated the absorption and emission of the ADB molecule in ethanol as well as of the Zn-ADB-MOF. Moreover, Table 17 provides the shift between the experimental excitation energies of the ADB molecule in solution and inside the MOF. In case of the calculations, the shift between the molecule in ethanol (SMD) and the cut monomer is given.

As already shown in the benchmarking, the excited state properties of SVP and TZVP geometries should be comparable and are not influenced by the SMD solvent model. The difference in the absorption energy (~0.2 eV, “shift” Table 17) between the molecule in solution and the monomer experiencing periodic influence is due to the change in the

Ant/Ph angle. The decrease from  $\sim 81^\circ$  (molecule) to  $\sim 66^\circ$  (monomer cut from trimer) leads to stronger interaction between the aromatic systems of the phenyl rings and the anthracene moiety and, thus, to smaller absorption energies. Interestingly, the experimental difference between the molecule and the MOF found by R.Haldar et al.<sup>57</sup> is only about 0.05 eV. This is a quarter of the shift expected from computations. On the one hand this could be an error of the calculations due to the neglect of actual solvent molecules or of periodic effects during the TD-DFT calculations. However, on the other hand this could also mean that the ADB incorporated in the MOF is less tilted as the experimental unit cell suggests.

On the other side, the calculated emission energy is increased by about 0.1 eV from the molecule to the cut monomer (Table 17). Due to the sterical hindrance of the adjacent linkers, the anthracene-phenyl angle is less flattened in the trimer compared to the molecule in solution. In experiment, incorporation of ADB into the MOF structure decreases its emission energy by about 0.3 eV. Such a change is not found in the calculation. Note that this discrepancy between experiment and calculation could easily be due to the crude modelling of the excited state in an oligomer. However on the other hand, it is also possible, that this hints towards an actual change of the emission properties, as for example due to excimer formation.

*Table 17: Vertical absorption and emission of the ADB molecule in ethanol (TZVP//TZVP), the monomers cut from the trimer (TZVP//SVP) representative for the periodic structure and the experimental value from ref.57; calculated and experimental shift respectively between molecule and monomer.*

		abs [eV]	shift [eV]	em [eV]	shift [eV]
cis	molecule	3.365		2.739	
	monomer	3.198	-0.17	2.899	+0.16
trans	molecule	3.347		2.738	
	monomer	3.130	-0.22	2.866	+0.13
experiment	molecule	3.3		2.9	
	MOF	3.25	-0.05	2.6	-0.3

Note that at this point I will proceed with the calculation of the Förster Resonance energy transfer between the monomer units cut from the trimers. Analysis of the excited state properties of the oligomers (trimers and tetramers) is given in chapter 6.3.8 *Beyond simple hopping in Scenario 2*.

### 6.3.6 Monomer hopping

The transition densities of the monomers cut from trimers (Table 16) were used to study the Förster resonance energy transfer provided that the excitation is localized on only one ADB linker. This corresponds to the transport of the  $PL_{\text{mon}}$  component, described in the motivation-section (6.1).

The Coulomb coupling was calculated according to Eq.11 along four different directions as visualised in the scheme in Figure 34. Considering the given MOF-structure, three different hoppings may occur within the same sheet (called perp, diag and hori), whereas one path requires inter-sheet hopping (para). The latter is also the path to the closest adjacent monomer. To demonstrate the distance dependency of the Coulomb coupling, the coupling to the second nearest neighbour along the inter-sheet direction was calculated as well (para second) by simply doubling the distance between the cube-files.

Along each of these five potential hopping routes the exciton covers a different distance inside the framework. In this case the jumping distance is measured as the distance between the centers of mass of two chromophores, and is the same for both phases. The Coulomb couplings of both conformers and their corresponding distances are listed in Table 18. In the following, the couplings are calculated with two different approaches:

In the first approach ( $S_0$ - $S_0$ ), the donor as well as the acceptor ADB is in  $S_0$  geometry. This approach is theoretically wrong as the donor should be in  $S_1$  geometry. However, it has the advantage that the time-consuming  $S_1$  optimization is avoided. In the second approach ( $S_1$ - $S_0$ ) the donor is in  $S_1$  geometry and the acceptor is in  $S_0$  geometry. Both approaches result in the same qualitative trend.

With the highly favourable coupling along the para-direction, Table 18 shows a substantial anisotropy of the Coulomb coupling. The energy transfer in para-direction to the nearest sheet is at least five times faster than in every other direction and even one order of magnitude higher than to the second nearest sheet. A jump to the second nearest neighbour is, therefore, unlikely within the Förster model.

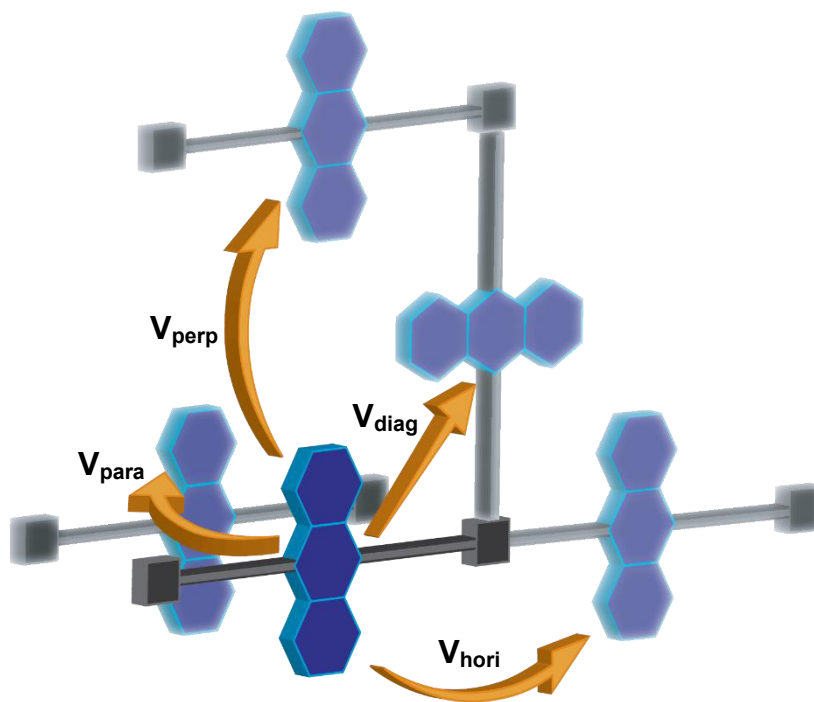


Figure 34: Schematic representation of the four different nearest hopping directions inside the MOF.

Table 18: The five potential Coulomb couplings of both phases applying the TDC-Method with two different approaches;  $S_0$ - $S_0$ : donor and acceptor in  $S_0$  geometry,  $S_1$ - $S_0$ : donor in  $S_1$  geometry, acceptor in  $S_0$  geometry.

		para	para second	perp	hori	diag
Jump distance [Å]		5.81	11.63	19.81	19.81	13.95
$S_0$ - $S_0$ $V^2$ [ $\text{cm}^{-2}$ ]	<i>cis</i>	13799	964	80	1542	2387
	<i>trans</i>	21381	1280	93	1938	3209
$S_1$ - $S_0$ $V^2$ [ $\text{cm}^{-2}$ ]	<i>cis</i>	20402	1386	112	2217	3397
	<i>trans</i>	27710	1673	122	2381	3949

Note that in chapter 6.3.3 *Periodic simulations* a bigger unit cell was introduced, which differs from the smaller experimental unit cell by the ADB units of one sheet alternately pointing in opposite directions (compare Figure 29). The effect of this alternating rotation of  $180^\circ$  on the *cis*-conformer was investigated within the  $S_1$ - $S_0$  approach. For this, the  $S_0$  transition density was rotated by  $180^\circ$  and the coupling calculated along the perp- and hori-direction. The couplings in the alternating arrangement were calculated to be 107 and  $2188 \text{ cm}^{-2}$  compared to 112 and  $2217 \text{ cm}^{-2}$  in the experimental unit cell (Table 18). Rotation of the linker by  $180^\circ$  has, thus, no effect on the general trend of the Coulomb coupling and bigger unit cells were not investigated any further.

### 6.3.7 Model system anthracene

Interestingly, the coupling along the inter-sheet distance increases upon changing from *cis* to *trans*-phase (see Table 18). This seems counterintuitive as the main part of the transition density is localized on the anthracenes and the normal distance between the anthracene rings increases as well in the *trans*-phase. With increasing distance, one would, therefore, expect a decrease in the coupling. To investigate this, an anthracene molecule was chosen as a test system and absorption and emission for the first excited state calculated as described in the *Computational Details*.

Two parameters were identified to define the positions of the anthracenes within the phases. This approach is visualized in Figure 35. The normal distance,  $n$ , is defined as the distance between the planes of the anthracenes. The displacement,  $d$ , is defined as the difference distance to a perfectly stacked arrangement. The center-to-center distance,  $c$ , is the same for both phases, as it corresponds to the *c*-axis of the unit cell, which was held fix at the experimental value.

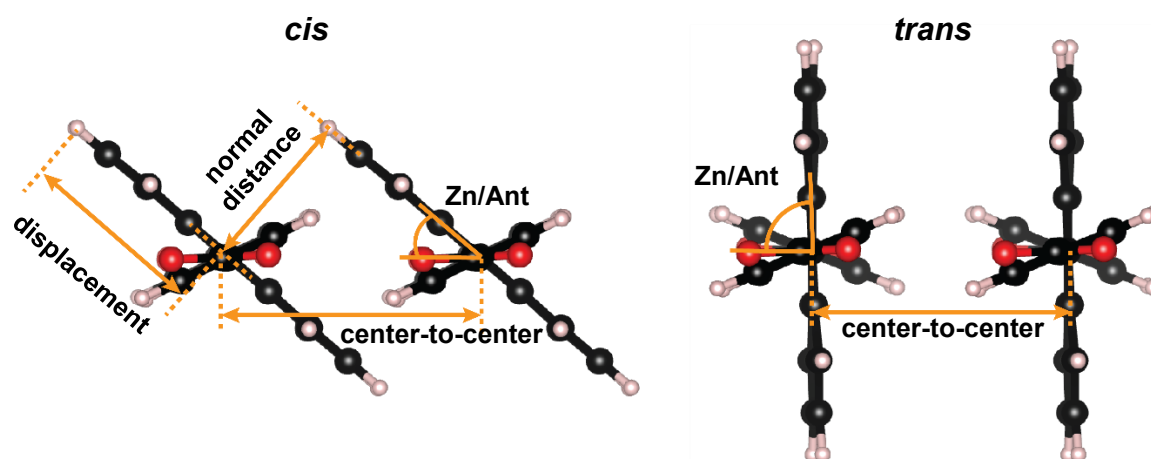


Figure 35: Schematic splitting of Zn/Ant-rotation in displacement and normal distance in the *cis*-phase (left) and the *trans*-phase (right).

Arranging the absorption and emission transition density of anthracene (Figure 36) with different displacement and normal distances should simulate the two MOF phases.

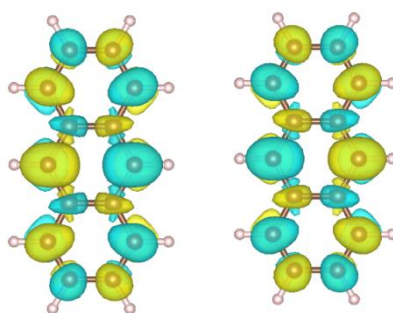


Figure 36: PBE0+D3/def2-TZVP transition densities of absorption (left) and emission (right) of anthracene.

The values  $n$  and  $d$  of both phases as well as their corresponding Zn-anthracene angles are listed in Table 19. The Coulomb coupling was calculated according to the  $S_1-S_0$  approach while scanning the distances between those values. This results in the graphic shown in Figure 37. Lighter areas correspond to more favourable pairs of  $(n,d)$  in terms of the coupling. The black spots indicate the *cis* and *trans*-phase, respectively. The different Zn/Ant angles of the *cis* and the *trans*-phase are responsible for their differing displacements and normal distances. The change of the Coulomb coupling by changing the Zn/Ant angle is shown in Figure 37 by the black line.

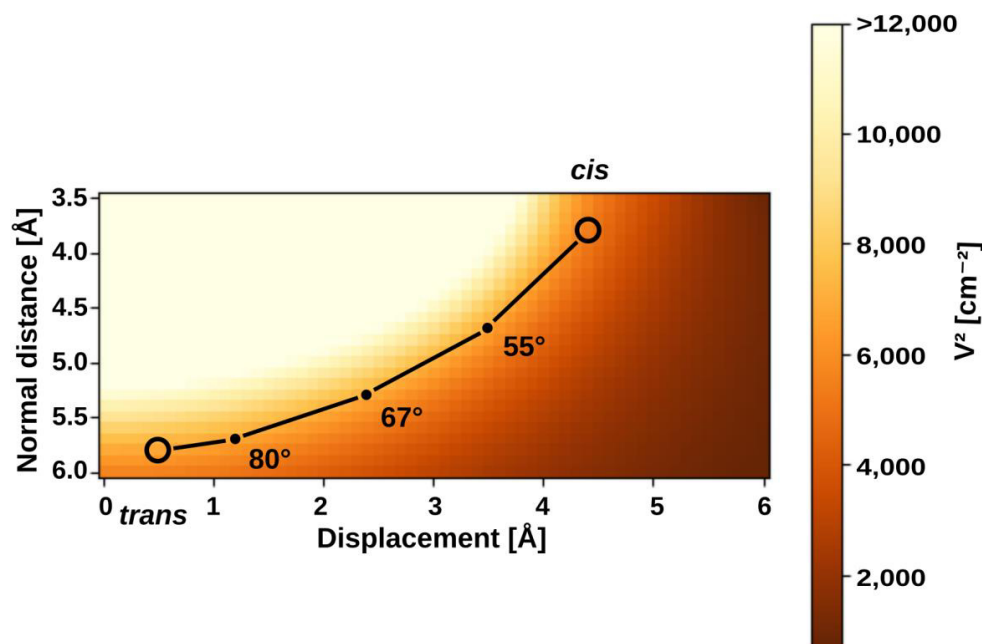


Figure 37: Screening of the Coulomb coupling [ $\text{cm}^{-2}$ ] in  $0.1 \text{ \AA}$  steps between the normal distance and displacement of both phases; the black line indicates the change of the Zn/Ant angle from  $42^\circ$  (*cis*) to  $88^\circ$  (*trans*).

Table 19: Normal distance,  $n$ , and displacement,  $d$ , of anthracene moieties, corresponding to the *cis* and *trans*-phase of the MOF.

$S_1-S_0$	$n$ [ $\text{\AA}$ ]	$d$ [ $\text{\AA}$ ]	$c$ [ $\text{\AA}$ ]	Zn/Ant [ $^\circ$ ]	$V^2$ [ $\text{cm}^{-2}$ ]
<i>cis</i> -MOF	3.8	4.4	5.81	42	5441
<i>trans</i> -MOF	5.8	0.5	5.81	88	6809

In accordance with the computation of the full system (Table 18), the coupling in *trans*-arrangement is bigger, highlighting the influence of the displacement factor. The Coulomb coupling is dependent on the distance between the transition densities. At small displacements, transition density elements of the donor and the acceptor with the same sign lay on top of each other. As the displacements get bigger, these transition density elements go away from each other, whereas elements of opposite sign get closer together. Due to a bigger compensation of the contribution of elements of the same and opposite sign at large displacements, the coupling is smaller.



### 6.3.8 Beyond simple hopping

As a first conclusion, the Coulomb coupling between two ADB units and, thus, also the rate of Förster resonance energy transfer shows highly anisotropic character. However, this does not necessarily correlate with the anisotropy measured in experiment. In the experiment by R.Haldar et al.,<sup>57</sup> the Förster transfer between an ADB donor and a DPP acceptor is measured. Due to the low concentration of DPP doping in the Zn(ADB)-SURMOF, inter-ADB transport is necessary for the exciton to reach a DPP to interact with. Subsequently, they conclude anisotropy of the inter-ADB transport by construction of different layered MOFs, as described in the motivation-section. However, note that none of these experiments measure the direct coupling between two ADB units.

The schematic representation of Figure 38 illustrates the idea of Förster transfer based on monomer hopping inside the MOF. In Figure 38, a DPP acceptor molecule is placed at a distance of about 40 Å from the excited ADB linker along the perp-, hori- and para-direction (names according to Figure 34). As illustrated, it would be the second nearest neighbour in the intra-sheet direction (perp and hori), however, it would only be the seventh neighbour in the inter-sheet direction (para).

Assuming a ADB-DPP interaction distance of 20 Å, we perform a thought experiment to link the calculated Coulomb coupling with the experimentally measured values. The excitation needs only one jump along the intra-sheet direction (perp and hori) to be in interaction distance with a DPP. However, as the inter-sheet distance (para) is significantly shorter (~6 Å, Table 18), it needs at least 3 jumps along the inter-sheet direction to be able to interact with a DPP.

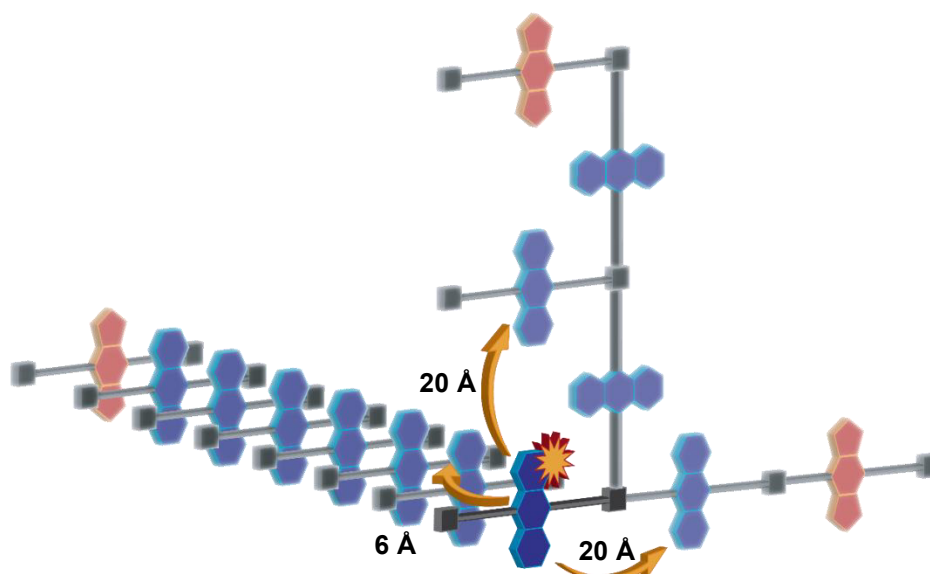


Figure 38: Schematic representation of Förster transfer over 40 Å based on monomer hopping in the Zn-SURMOF; blue=ADB, orange=DPP, asterisk=excitation.

Therefore, not only the rate of the energy transfer but also the diffusion of the exciton is important in the experiment. Modelling of the exciton diffusion is not part of this thesis. However, it has been done by Markus Krammer and suggests that the diffusion is less anisotropic as it could be expected from the Coulomb couplings.\*

Thus, the following section is dedicated to several ideas on how to expand the picture of energy transport and to find a cause for the anisotropy. Attention is laid on the explanation of the two experimentally observed lifetimes (1.5 and 4 ns) and the time delay of 80 ps of the anisotropic exciton travelling along the inter-sheet distance.

---

\* Modelling of exciton diffusion based on the computed couplings has been carried out by Markus Krammer, but is not presented here, as it is not part of this thesis. When translating the Coulomb coupling to exciton diffusion, it is weakened due to the quadratic dependence of the exciton diffusion on the jumping distance (can be derived by Fick's first law of diffusion). As a consequence, the exciton diffusion is less anisotropic as it could be presumed by only looking at the Coulomb coupling.

### Scenario 1 – Rotation of the linker

This scenario includes ideas about rotation of the *cis*-linker and its consequences. Assuming that the MOF consists of the *cis* phase as described by R.Haldar et al., rotation of the ADB linkers could lead to a change of the Coulomb coupling and the formation of excimers.

Two possible rotations were investigated. First, the rotation of the whole ADB linker including both phenyl rings and the anthracene moiety was considered. The potential energy surface of the anthracene rotation was calculated with single points by building a trimer of three ADB monomers in  $S_0$  geometry and rotating the central monomer in steps of  $5^\circ$ , while keeping the end monomers fixed. The energy surface is shown in Figure 39. Furthermore, Figure 39 shows the potential energy surface of the ADB rotation in the unit cell calculated with single points periodically.

The periodic energy surface shows a maximum at a Zn/Ant angle of  $66^\circ$ . Note that the Ant/Ph angle of ADB is  $66^\circ$  as well. A Zn/Ant angle of  $66^\circ$ , therefore, corresponds to a Zn/Ph angle of  $0^\circ$ . In other words, both the phenyl rings of the ADB linker lie in the Zn-plane. As the cell is repeated periodically, consequently all the phenyl rings lie in the Zn-plane. Due to the arrangement in the unit cell (compare Figure 27), they experience maximum sterical hindrance from the neighbouring phenyl rings at this angle. In contrast, this maximum is not observed in the trimer calculation, as only the central unit is rotated, instead of all units. Considering the energy available at room temperature ( $\sim 2.5$  kJ/mol), a change of the rotational conformation of the ground state greater than  $15^\circ$  seems to be energetically too expensive. However, it is possible with the energy provided by the irradiated light of 380 nm ( $=3.3$  eV).

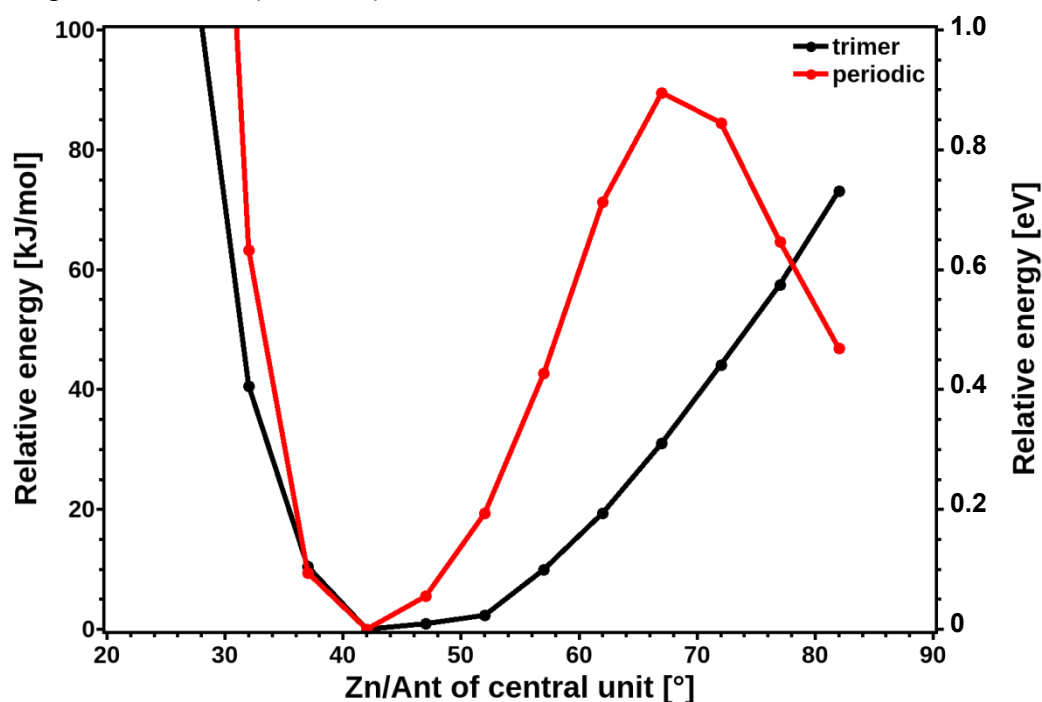


Figure 39: Potential energy surface of the ADB rotation in a trimer (PBE0+D3/def2-SVP) and periodically (PBE+TS/tight).

To find the optimal interaction between two units, the Coulomb coupling as a function of the ADB rotation was screened (see Figure 40). For this, the acceptor ADB monomer in  $S_0$  geometry as well as the donor ADB monomer in the excited  $S_1$  state was rotated in steps of  $5^\circ$ . The couplings to the nearest neighbours were calculated between ADB units rotated by the same amount.

Rotation of the whole ADB linker has only little effect on the intra-sheet couplings (diag, hori, perp). The behaviour of the coupling along the inter-sheet direction (para) is caused by the different displacement of the aromatic rings already investigated in chapter 6.3.7 *Model system anthracene*. Rotation of both the donor and the acceptor ADB by the same amount changes the displacement,  $d$ , of the aromatic rings. As already shown, smaller displacement leads to a bigger coupling.

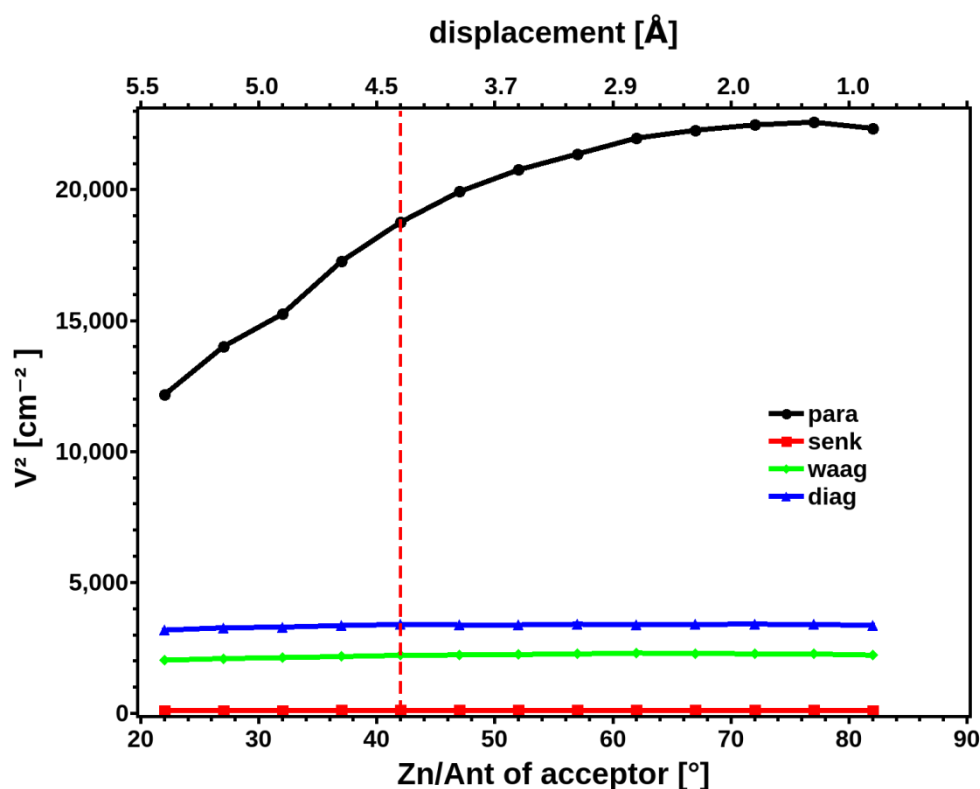


Figure 40: Coulomb coupling in four different directions applying the TDC-method after rotation of the donor and acceptor monomer by the same amount; displacement stands for the displacement of the anthracenes of the monomers; the bulk conformation is indicated with a dashed line.

Second, the rotation of only the anthracene moiety was investigated. The potential energy surface of the anthracene rotation was calculated with single points by building a trimer of three ADB monomers in  $S_0$  geometry and rotating the anthracene moiety of the central monomer in steps of  $5^\circ$ , while keeping the end monomers fixed. A schematic representation is shown in Figure 41 together with the energy surface. Furthermore, Figure 41 shows the potential energy surface of the anthracene rotation in the unit cell calculated

with single points periodically. Considering the energy available at room temperature ( $\sim 2.5$  kJ/mol), a change of the rotational conformation of the ground state greater than  $5^\circ$  seems to be energetically too expensive. Again, the rotation is possible with the energy provided by the irradiated light of 380 nm ( $\approx 3.3$  eV).

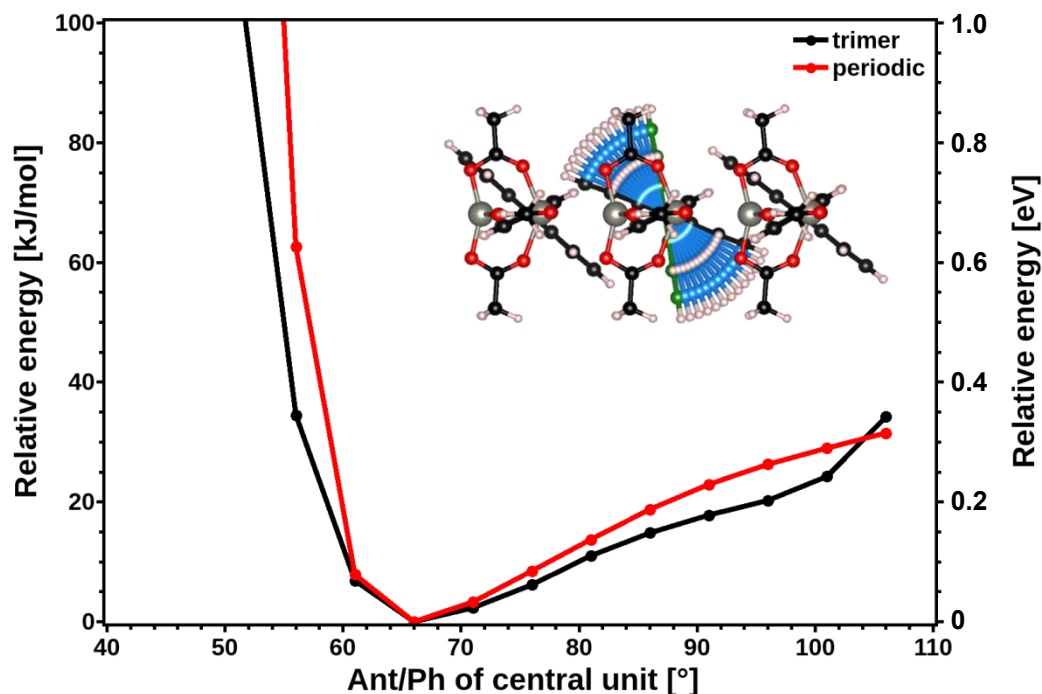


Figure 41: Potential energy surface of the anthracene rotation in a trimer (PBE0+D3/def2-SVP) and periodically (PBE+TS/tight).

Analogous to the rotation of the whole ADB linker, the coupling in dependence of only the anthracene rotation was investigated. For this, the anthracene moiety of the acceptor ADB monomer in  $S_0$  geometry was rotated. The geometry of the donor ADB was held fixed in the excited  $S_1$  state. Then the Coulomb coupling was calculated to the nearest neighbours.

The parabolic shape of the curves in Figure 42 is due to the change of the distribution of the transition density of the acceptor ADB after rotating the anthracene. All five curves show fairly the same behaviour, so that the ratio between the Coulomb couplings in two different directions is not altered much. This means, that also the behaviour of the exciton diffusion is preserved upon rotation.

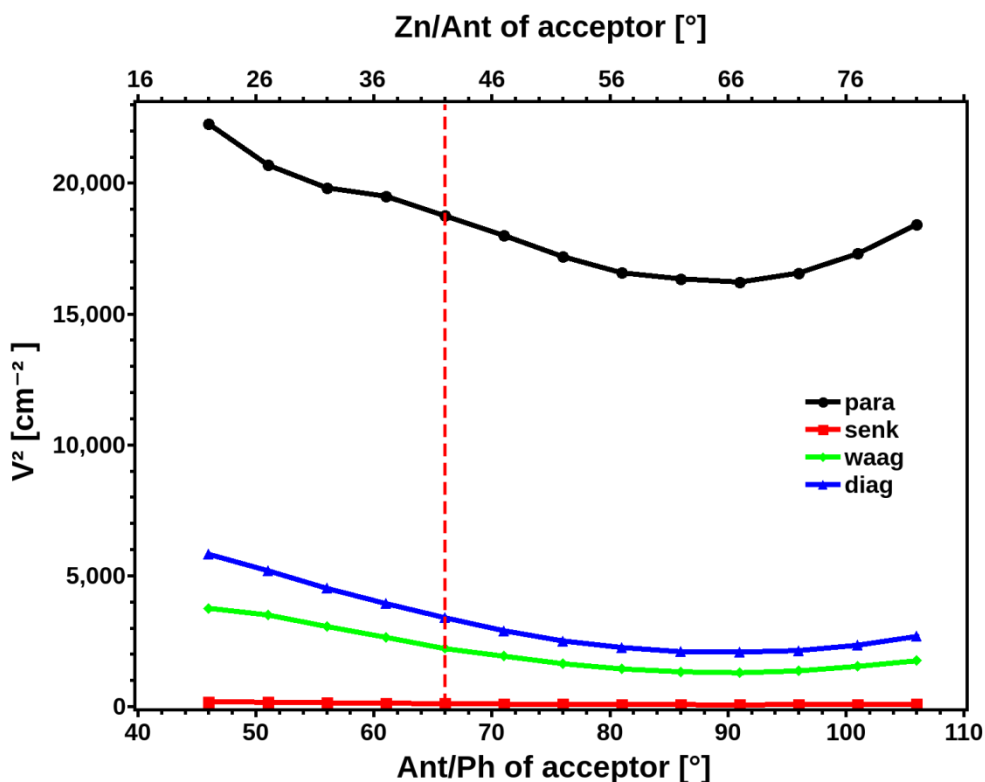


Figure 42: Coulomb coupling in four different directions applying the TDC-method after rotation of the acceptor monomer; the bulk conformation is indicated with a dashed line.

As already explained, the cause of the parabolic shape is the change of the distribution of the transition density of the acceptor ADB with rotation of the anthracene. Decreasing the angle between anthracene and benzenes results in an expansion of the transition density into the benzene rings. The lower limit of the Ant/Ph angle is given by the sterically hindrance between the anthracene (and phenyl) groups. For the investigation, it is set to an anthracene-phenyl angle of 46°. On the other hand, when the anthracene is perpendicular to the benzene rings, the transition density is only located on the anthracene resulting in the smallest coupling. A comparison of the transition densities of the limiting cases is shown in Figure 43. Figure 44 is another visualization of this rotation dependent distribution of the transition density. It shows the partial summation of the cube-file along the short molecular axes (y and z) of the bulk conformer (Ant/Ph = 66°) and the two limiting cases (Ant/Ph = 46° and 91°).

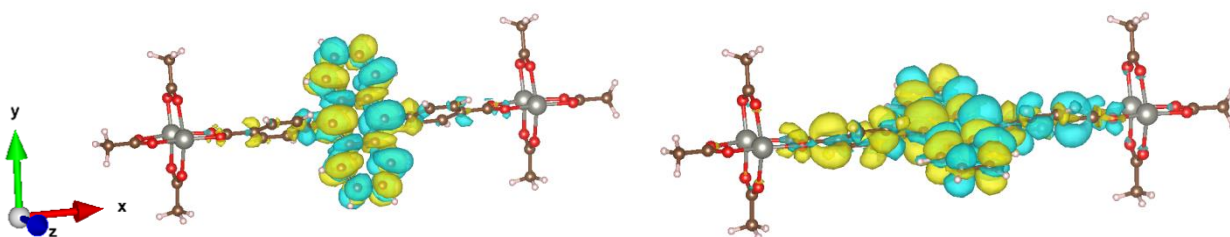


Figure 43: Transition densities of the upper limit (left, Ant/Ph=91°) and lower limit (right, Ant/Ph=46°) concerning the anthracene-phenyl angle showing the different distribution of the exciton.

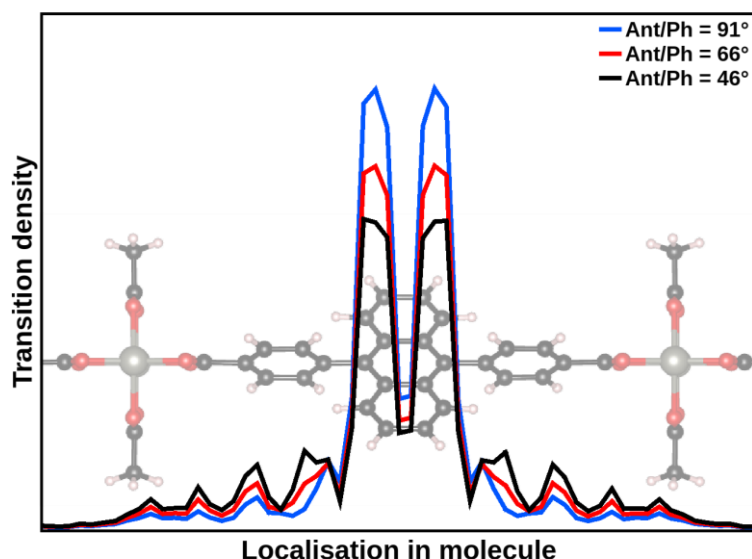


Figure 44: Distribution of the transition density by partial integration along the short molecular axes of the bulk conformer and at different Ant/Ph angles.

Simple rotation of the anthracene may not be the source for the anisotropic energy transfer as it changes the Coulomb coupling almost equally in all directions. However, these calculations say little about the possibility of excimer formation along the inter-sheet direction, as a source of the anisotropic energy transfer. The occurrence of such excimers between ADB units has been shown in literature.<sup>63,64</sup> A counterargument is, that the lifetime of these excimers is usually substantially longer (20 ns) than all the ones measured by R. Haldar et al. (4 ns). Moreover, there is no explanation for the formation time of the excimer of about 80 ps.<sup>†</sup>

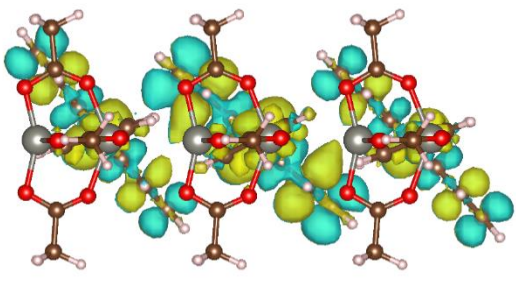
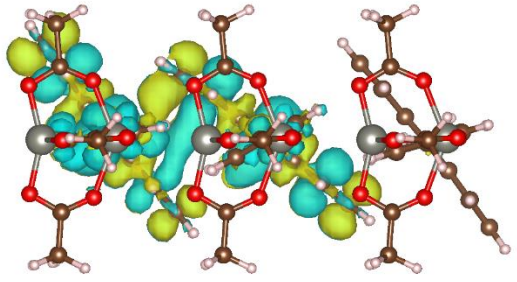
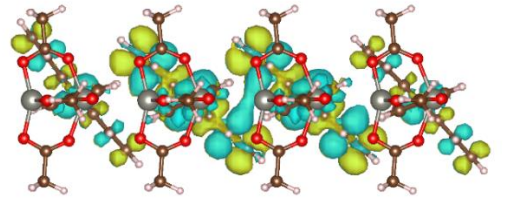
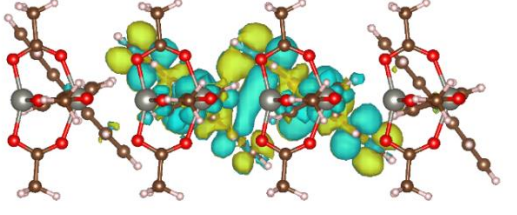
<sup>†</sup> Tomas Kamencek calculated the frequency of the anthracene rotation with FHI-Aims/Phonopy. It is 1.56 THz which corresponds to the time period for the rotation of 0.64 ps. This is significantly faster than the rise time of 80 ps.

## Scenario 2 – Excimer formation

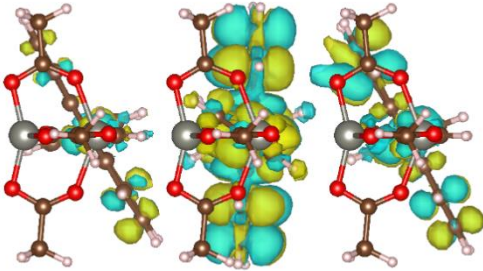
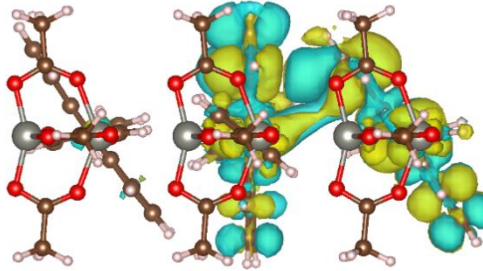
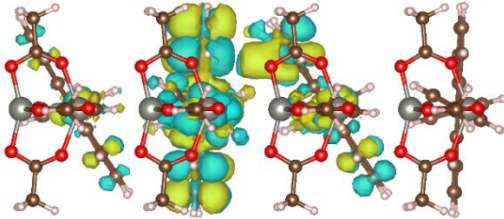
R. Haldar et al.<sup>57</sup> measured a time-dependent red-shift of the emission spectrum of the Zn(ADB)-SURMOF, which they attributed to the formation of an excimer state among the ADB units along the inter-sheet direction.

In this context, the excitation properties of the trimer and tetramer cluster were investigated. The energies and oscillator strengths of the transition  $S_0$ - $S_1$  are listed in Table 20. The corresponding transition densities are shown as well. Due to the limitations described in the *Cluster approach*, the optimization of the first excited state of the tetrameric *trans*-phase was not reasonable and thus, is not shown here.

Table 20: PBE0+D3/def2-SVP excitation energies  $E_{ex}$ , oscillator strengths  $f_{osc}$ , transition dipoles  $\mu_{tr}$  and transition densities of trimer and tetramer clusters of both phases.

	trimer					
	abs			em		
cis						
	$E_{ex}$ [eV] ( $f_{osc}$ )	$\mu_{tr}^2$ [au <sup>2</sup> ]	$\begin{pmatrix} \mu_{tr,x} \\ \mu_{tr,y} \\ \mu_{tr,z} \end{pmatrix}$ [au]	$E_{ex}$ [eV] ( $f_{osc}$ )	$\mu_{tr}^2$ [au <sup>2</sup> ]	$\begin{pmatrix} \mu_{tr,x} \\ \mu_{tr,y} \\ \mu_{tr,z} \end{pmatrix}$ [au]
	2.914 (0.117)	1.63	$\begin{pmatrix} -1.28 \\ -0.01 \\ 0.05 \end{pmatrix}$	2.464 (0.043)	0.72	$\begin{pmatrix} 0.85 \\ 0.01 \\ -0.04 \end{pmatrix}$
	tetramer					
	abs			em		
						
	$E_{ex}$ [eV] ( $f_{osc}$ )	$\mu_{tr}^2$ [au <sup>2</sup> ]	$\begin{pmatrix} \mu_{tr,x} \\ \mu_{tr,y} \\ \mu_{tr,z} \end{pmatrix}$ [au]	$E_{ex}$ [eV] ( $f_{osc}$ )	$\mu_{tr}^2$ [au <sup>2</sup> ]	$\begin{pmatrix} \mu_{tr,x} \\ \mu_{tr,y} \\ \mu_{tr,z} \end{pmatrix}$ [au]
	2.893 (0.148)	2.09	$\begin{pmatrix} 1.44 \\ 0.01 \\ -0.07 \end{pmatrix}$	2.528 (0.051)	0.82	$\begin{pmatrix} 0.90 \\ 0.01 \\ -0.06 \end{pmatrix}$



<b>trans</b>	<b>abs</b>			<b>em</b>		
						
	$E_{\text{ex}}$ [eV] ( $f_{\text{osc}}$ )	$\mu_{\text{tr}}^2$ [au <sup>2</sup> ]	$\begin{pmatrix} \mu_{\text{tr},x} \\ \mu_{\text{tr},y} \\ \mu_{\text{tr},z} \end{pmatrix}$ [au]	$E_{\text{ex}}$ [eV] ( $f_{\text{osc}}$ )	$\mu_{\text{tr}}^2$ [au <sup>2</sup> ]	$\begin{pmatrix} \mu_{\text{tr},x} \\ \mu_{\text{tr},y} \\ \mu_{\text{tr},z} \end{pmatrix}$ [au]
	2.943 (0.009)	0.120	$\begin{pmatrix} -0.35 \\ -0.01 \\ 0.00 \end{pmatrix}$	2.444 (0.005)	0.08	$\begin{pmatrix} -0.27 \\ -0.01 \\ 0.06 \end{pmatrix}$
	<b>tetramer</b>					
	<b>abs</b>			<b>em</b>		
			-			
$E_{\text{ex}}$ [eV] ( $f_{\text{osc}}$ )	$\mu_{\text{tr}}^2$ [au <sup>2</sup> ]	$\begin{pmatrix} \mu_{\text{tr},x} \\ \mu_{\text{tr},y} \\ \mu_{\text{tr},z} \end{pmatrix}$ [au]				
2.903 (0.003)	0.04	$\begin{pmatrix} -0.20 \\ -0.01 \\ -0.03 \end{pmatrix}$				

Note that the shape of the transition density of the optimized oligomers could be misleading. The lack of meaning of DFT-wavefunctions and their basis set dependence (as described in the chapters *Benchmarking of the basis set* and *Cluster approach*) can introduce errors to the interpretation of the excitation properties.<sup>65</sup> Moreover, any major changes in the bond lengths were prevented by the constrained Zn- and O-atoms. Keeping these limitations in mind, the calculations are interpreted here.

Table 21 compares the excitation energies and oscillator strengths of the oligomer calculations (TZVP//SVP) with the ones of the cut monomers (TZVP//SVP) and the experimental values attributed to the monomer (PL<sub>mon</sub>) and excimer state (PL<sub>exm</sub>) of the Zn(ADB)-MOF from ref.57.

In general, there is only little difference between the absorption and emission energies of the *cis* and *trans*-phase (Table 21). For both phases the absorption and emission of the cut monomer is in good agreement with the experimental absorption and emission (PL<sub>mon</sub>).

The emission energies of the oligomer calculations (~2.53 eV, Table 21) are consistent with the experimental value of 2.58 eV attributed to the emission of an excimer state, PL<sub>exm</sub>.

However, the excitations in the oligomers are rather weakly allowed transitions, with oscillator strengths significantly smaller than for monomer excitations (Table 21). Furthermore, the oscillator strengths for the excitation in the *trans*-clusters are considerable smaller than in the *cis*-clusters. As the oscillator strength is related to the transition dipole and, thus, also to the transition density, it directly affects the Coulomb coupling. This would lead to smaller energy transfer rates, the smaller the oscillator strength is.

Table 21: Vertical absorption and emission of the *cis* and *trans*-monomers cut from the trimers, and of the trimers and tetramers (all TZVP//SVP) and the experimental values from ref.57 attributed to the monomer PL<sub>mon</sub> and the excimer PL<sub>exm</sub>.

		abs [eV] (f <sub>osc</sub> )	em [eV] (f <sub>osc</sub> )
monomer	<i>cis</i>	3.198 (0.435)	2.899 (0.558)
	<i>trans</i>	3.130 (0.474)	2.866 (0.563)
trimer	<i>cis</i>	2.914 (0.117)	2.464 (0.043)
	<i>trans</i>	2.943 (0.009)	2.444 (0.005)
tetramer	<i>cis</i>	2.893 (0.148)	2.528 (0.051)
	<i>trans</i>	2.903 (0.003)	-
experiment	PL <sub>mon</sub>	3.25	2.81
	PL <sub>exm</sub>		2.58

The transition density of the absorption is distributed over all monomer units. Interestingly, the transition density of the emission is distributed over two ADB units only independent of the oligomer size. This could suggest a delocalization of the S<sub>1</sub> state on these two monomers. The statement is supported by comparison of the respective bond lengths (*Appendix A1.3*), indicating a quinoid-like structure for only two monomers in the oligomers. Such a delocalization of the emission hints towards orbital overlap and possible Dexter energy transfer. Moreover, the picture of monomer based Förster resonance energy transfer breaks down.

To further investigate the interaction between the ADB linkers, oligomers consisting of up to 8 *cis*-monomers in S<sub>0</sub> geometry were built along the perp-, hori- and para-direction. This

should simulate the periodic MOF along the a-, b- and c-axis, respectively. To reduce the computational cost, the calculations of these oligomers were done on a semiempirical level with ZINDO/S as implemented in ORCA.

With increasing number of monomer units in the oligomers, the number of linear combinations of the monomer HOMOs (and LUMOs) increases as well. An oligomer consisting of  $n$  monomers has  $n$  linear combination of the HOMOs (or LUMOs) of its monomers. In the present case, the symmetric linear combination of the HOMOs of the monomers is the energetically lowest one and will be called HOMO( $n$ ) (usually named HOMO-( $n+1$ )). The anti-symmetric linear combination of the HOMOs of the monomers is the energetically highest one and will be called HOMO. The two cases are shown in Figure 45 based on the *cis*-tetramer along the para-direction.

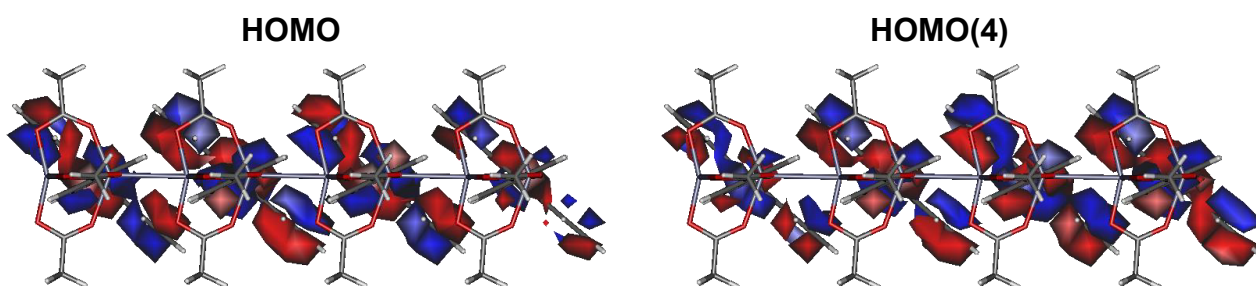


Figure 45: HOMO (left) and HOMO(4) (right) of the *cis*-tetramer along the para-direction calculated with ZINDO/S.

The energetic splitting of the HOMOs and LUMOs, respectively, was extracted from the calculations as a measure for the orbital interaction in the oligomers.<sup>66</sup> Figure 46 shows the splitting in dependence of the number of monomers in the oligomer. The splitting along the inter-sheet direction (para) is significantly larger than the splitting along the intra-sheet directions (perp and hori), as expected. This could hint towards orbital interactions along the inter-sheet direction and would lead to a breakdown of the picture of orbital interaction-free Förster transfer.

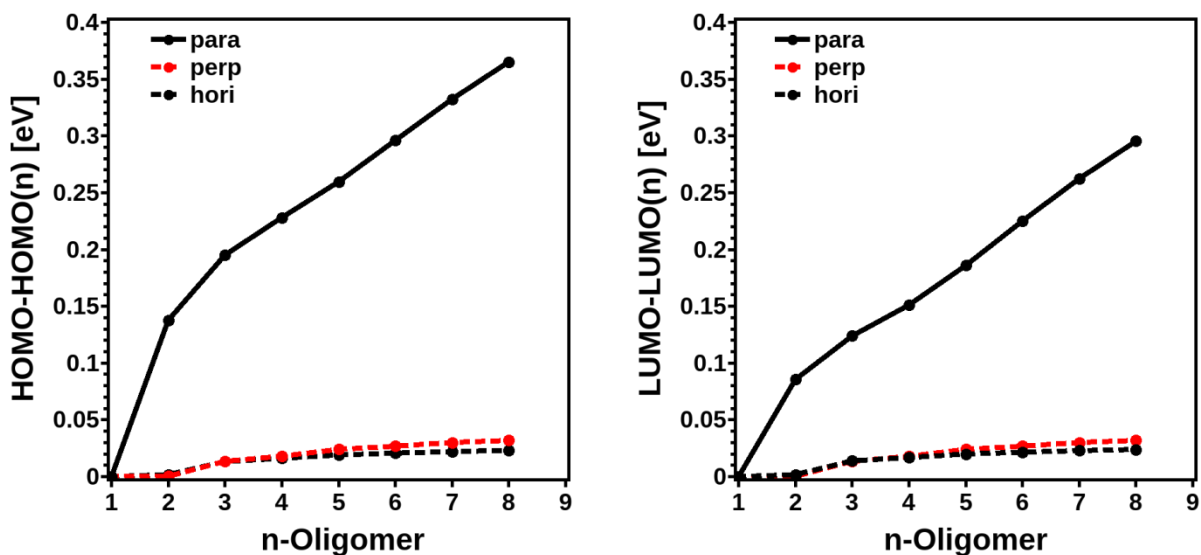


Figure 46: Energetic splitting of the HOMO (left) and LUMO (right) in dependence of the number,  $n$ , of monomers in an oligomer along the para-, perp- and hori-direction; calculated with ZINDO/S.

Based on the described calculations, factors beyond Förster theory like orbital overlap and Dexter transfer would lead to a more efficient transport of the exciton along the inter-sheet direction.

### Scenario 3 – Domains

Another possible explanation for the two different experimental lifetimes (1.5 and 4 ns) is based upon the assembling of the isomers in distinct domains. In general, these can be regions with ordered and less ordered arrangement of the linkers. In context of the two-phase approach, these regions could be domains with linkers mostly in *cis* or mostly in *trans*-conformation.

Considering the more general approach, the energy transport process in less ordered regions shows isotropic character due to monomer hopping. It takes the exciton about 4 ns to travel to ordered regions. These regions then show anisotropic character of the transport, for instance, due to the formation of more delocalized excited states. Another possibility is that the excitation (3.3 eV) provides the energy to heal defects leading to more ordered arrangements.

A schematic drawing of the idea is shown in Figure 47, the arrows represent the anisotropy of the energy transfer rates in the different domains. Broader arrows mean a faster energy transport along the inter-sheet direction.

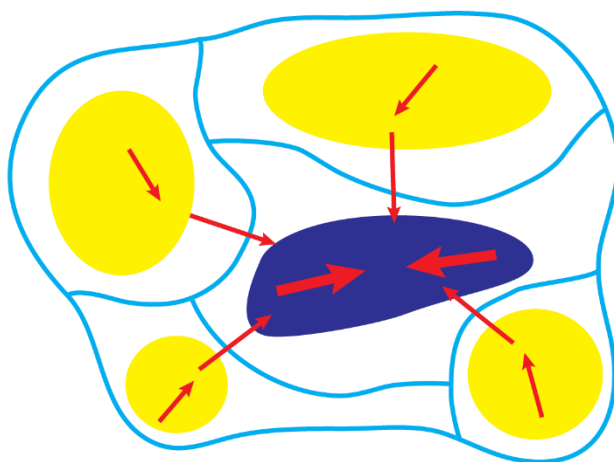


Figure 47: Schematic representation of the assembling of the isomers in two different domains (yellow and blue); arrows proportional to the anisotropy of the hopping.

#### Scenario 4 – Photoisomerization

The idea of photoisomerization is based upon the structural change of the isomers after irradiation. A 1:1 ratio of the isomers in solution (reasoned by the same relative energy of the conformers) may result in a random incorporation into the MOF. In the periodic case, a phase consisting only of *cis*-conformers is 61 kJ/mol more stable than the corresponding *trans*-phase and 30.5 kJ/mol more stable than a mixed phase consisting of one conformer each in the unit cell. Upon excitation some molecules could switch to the more stable phase forming domains as shown in Figure 48.

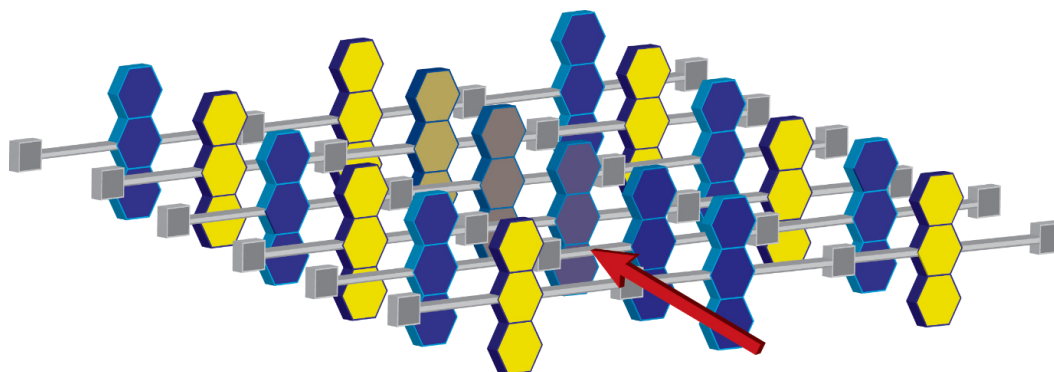


Figure 48: Schematic representation of a random assembling of the isomers in the MOF  
yellow = *trans*, blue = *cis*; colour gradient indicates phase transition.

A linear reaction path was calculated periodically to simulate the rotation of one linker in the unit cell from *trans* to *cis*-conformation. This corresponds to the change from the mixed to the more stable all-*cis* phase. The conformational change was represented by nine structures along the reaction coordinate as shown on the left side of Figure 49. The corresponding points on the reaction coordinate are shown on the right side of Figure 49, where the energy of the *cis*-phase is set to zero. According to this crude model, the transition from the unfavourable to the favourable phase needs to overcome a barrier of about 28 kJ/mol (= 0.29 eV). This energy could easily be provided by visible light during excitation of the MOF (= 380 nm).

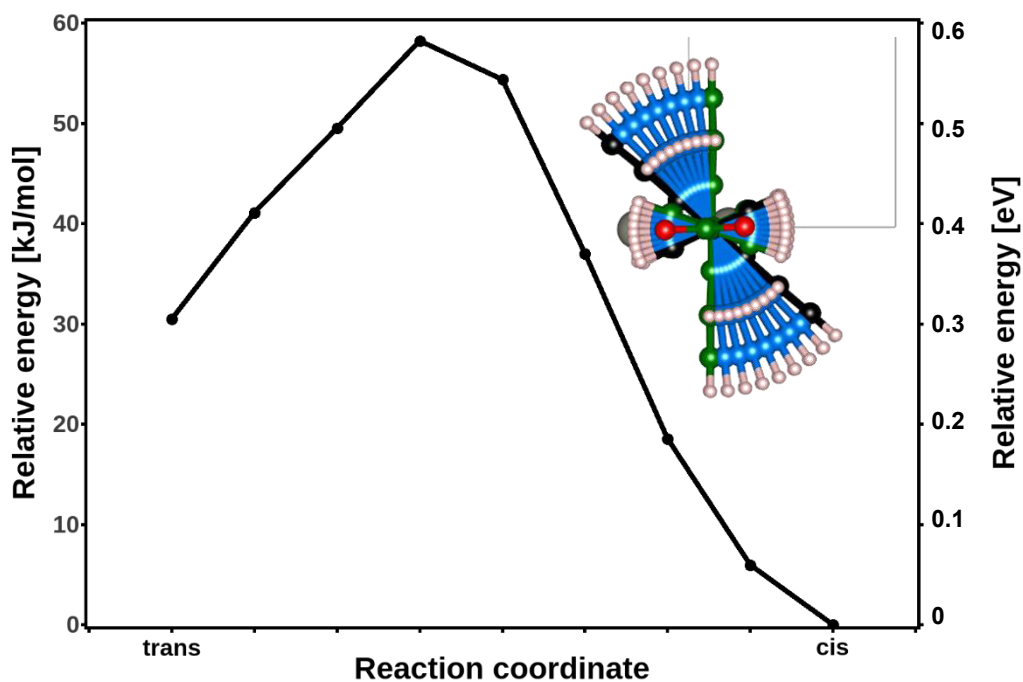


Figure 49: The conformational change inside the unit cell and the corresponding linear reaction path of the rotation of a linker from *trans* to *cis* configuration from periodic PBE+TS/tight calculations.

To simulate the interface between both phases along the inter-sheet direction, two tetramers were built consisting of two molecules of each isomer. In the first one the isomers were arranged ordered (domain-like), in the other one alternately (herringbone-like) as shown in Figure 50. Both tetramers optimized to an all *cis*-tetramer. It seems that in the presence of *cis*-units adjacent *trans*-molecules are favouring an interchange of the phases. Thus, randomly occurring higher concentration of *cis* molecules would lead especially to the formation of linear rod-like domains of the *cis*-phase.

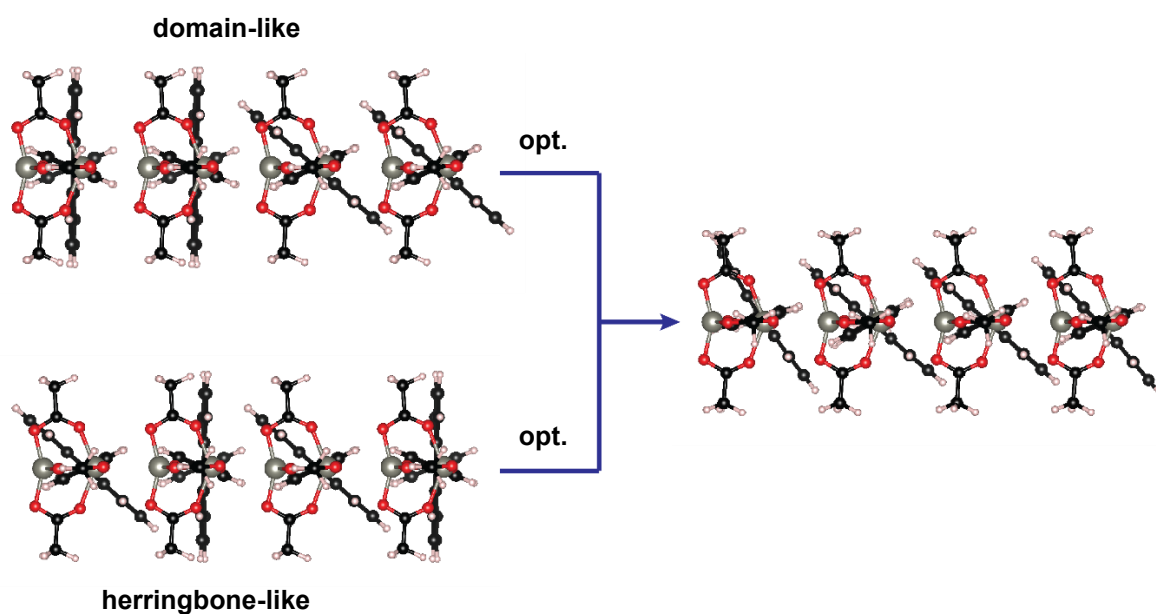


Figure 50: PBE0+D3 optimization of a tetramer consisting of two molecules of each conformation; start geometries (left) and optimized geometries (right).

To sum up, radiation could lead to the transition of a randomly mixed phase to partially ordered *cis*-domains. The rise time of 80 ps could then be attributed to the transition of *trans* to *cis*-isomers. While energy transport in the mixed phase may be due to simple hopping between adjacent organic linkers, more evolved mechanisms as already described in the other scenarios could be at work in the ordered *cis*-phase.

However, as both optimizations of mixed tetramers resulted in an all *cis*-tetramer, a mixed phase and the need for photoisomerization seem unlikely. Instead, it is more plausible that the *trans*-isomers already switch to the *cis*-isomers during the growing process and avoid the energetically unfavourable *trans*-phase.



### Scenario 5 – Fog of Unknown

First tests of the acceptor molecule DPP in the experimental unit cell suggests that it does not perfectly fit into the cell. Periodic optimization shows an avoiding of the suggested paddle wheel coordination, as depicted in Figure 51.

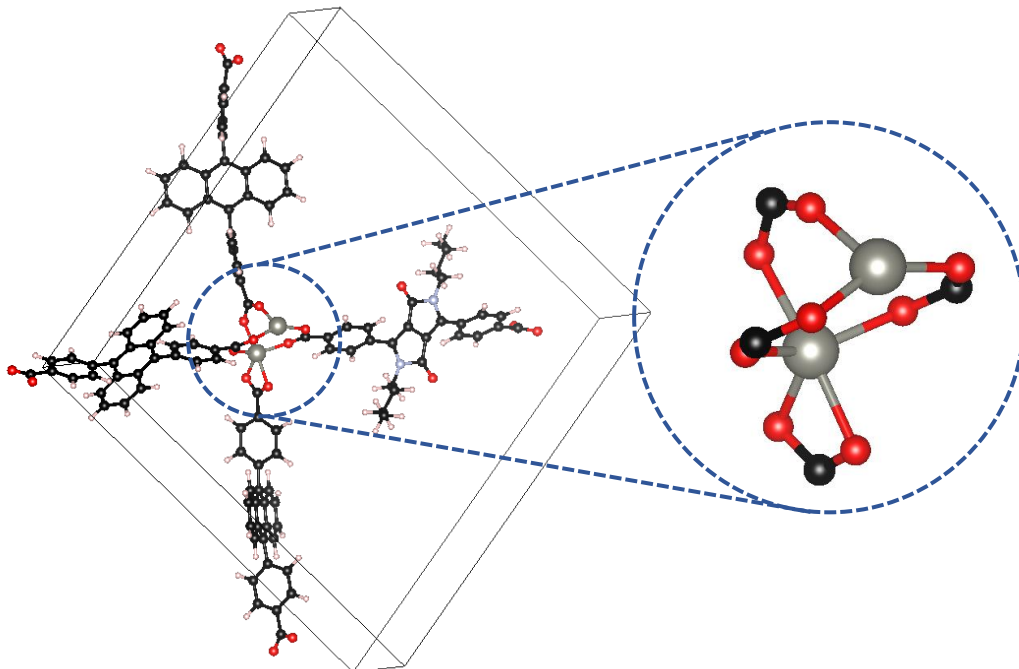


Figure 51: Detail of the optimization (PBE+TS) of a mixed unit cell with an ADB in the presence of DPP showing the destruction of the paddle wheel; right: linkers are omitted for clarity.

This may cause defects in the MOF upon incorporation of DPP and thus, more possible origins for the measured anisotropy. Moreover, the formation of one of the two ADB phases is maybe preferred due to the incorporation of the acceptor. However, deeper insight into these mechanisms has not yet been gained.

## 7 Conclusion

This thesis aims to characterize different metal organic frameworks at a DFT level of theory with a combination of periodic and molecular calculations. It provides a first overview of structural as well as electronic properties of these materials and can be seen as a starting point for further studies. The structures in question are a Cu(BDC) MOF, where BDC is benzenedicarboxylic acid and a Zn(ADB) MOF, where ADB is anthracene-dibenzoic acid. Both frameworks share common structural elements like the paddle-wheel secondary building unit or two-dimensional stacked arrays of MOF-layers, however, in this thesis they were investigated for very different reasons.

The divalent ion of Cu is complex to describe computationally due to its electron configuration. Molecular calculations of a Cu-paddle wheel with BDC as organic linker have shown its triplet state to be energetically very close to the broken-symmetry singlet ground state. This knowledge was further used for the periodic calculations of the Cu-MOF. The optimized unit cell of the MOF did not match the one found in experiments. In the bulk calculations, Cu tends to interact with an O atom of the next nearest secondary building unit instead of forming independently stacked arrays. This difference suggests either strong surface effects which enforce epitaxy or structural changes during synthesis, which were not considered, e.g. solvent coordination. Thus, the exact coordination environment of the Cu-paddle wheels could not be explained, but an attempt was made to simulate the docking of the first layer of organic linkers on the substrate. The most favourable arrangement of BDC on  $\text{Cu}(\text{OH})_2$  was found to be alternating OH functionalities on the surface with parallel or shifted arrays of terephthalic acid. The rigid arrangements with upright pointing carboxylic groups are possible anchors to enforce the experimentally found framework. However, further investigations are needed to clarify the growth process.

The Zn-MOF was studied with a focus on the energy transfer between its chromophoric ADB linkers. Molecular simulations in ethanol showed two different conformations of ADB (*cis* and *trans* respectively), which resulted in two different solid state structures. To gain excited state information about the MOF, a three-step approach was developed. After periodic calculations to get the bulk structure of the MOF, suitable oligomer and monomer units were chosen to get the transition density between the ground and first excited state applying TDDFT calculations. The Coulomb coupling as a measure for the Förster resonance energy transfer was then computed between the nearest neighbours in four directions with the TDC method. In both phases, the coupling along the parallel stacking direction is highly favourable. The coupling in the *trans*-phase is in general higher than in

the *cis*-phase, but the latter is energetically more stable in the MOF. Calculations on the test system anthracene revealed that the coupling is bigger, the smaller the displacement of adjacent anthracene moieties in the phase is.

Further, the thesis tries to connect the calculated Coulomb coupling with the experimentally observed transfer rates. In this context, it gives an outlook on several, more complex ideas beyond Förster theory. Calculations suggest strong interaction between adjacent linkers in the *cis*-phase, pointing towards short-range contributions and excimer formation. The experimentally found emission energy of the Zn-ADB-MOF can be explained by an  $S_1$  state of the *cis*-conformer, which is localized on two ADB linkers. Moreover, oligomer calculations suggest that the picture of excitation of only a single linker does not seem to be valid in general. Additionally, mixed incorporation of the two phases into the bulk could lead to differently ordered domains with different excitation properties. To clarify the energy transfer mechanism in this MOF system, further studies have to be made.

Altogether the thesis presents a variety of different approaches to deal with the theoretical description of metal organic frameworks.

## 8 Appendix

### A1 Excitation Analysis

#### A1.1 Benchmarking

Table 22 lists the energies and oscillator strengths of the first five singlet excitation of the ADB and DPP molecules calculated with PBE0/def2-TZVP and CAM-B3LYP/def2-TZVP in ethanol (SMD) as used in *Benchmarking of the functional* in chapter 6.2.6.

Table 22: First five singlets of absorption and emission of ADB in cis-conformation and DPP calculated with PBE0/def2-TZVP and CAM-B3LYP/def2-TZVP in ethanol as used in benchmarking.

PBE0	state	excitation energy [eV]	$f_{\text{osc}}$	transition	%	c
ADB abs	1	3.365	0.255	HOMO/LUMO	90.0	0.949
	2	3.528	0.000	HOMO/LUMO+1	99.1	-0.996
	3	3.564	0.003	HOMO/LUMO+2	95.3	-0.976
	4	3.883	0.002	HOMO/LUMO+3	53.1	-0.729
	5	4.209	0.000	HOMO/LUMO+4	93.0	-0.964
ADB em	1	2.739	0.538	HOMO/LUMO	92.8	0.963
	2	3.013	0.000	HOMO/LUMO+1	97.9	-0.990
	3	3.298	0.001	HOMO/LUMO+2	93.5	0.967
	4	3.746	0.001	HOMO/LUMO+3	48.3	0.695
	5	4.065	0.000	HOMO/LUMO+4	64.6	-0.804
DPP abs	1	2.791	0.635	HOMO/LUMO	92.2	-0.960
	2	3.146	0.000	HOMO-1/LUMO	95.3	-0.976
	3	3.356	0.000	HOMO/LUMO+1	93.2	0.965
	4	3.613	0.004	HOMO-2/LUMO	49.3	-0.702
	5	4.015	0.000	HOMO-3/LUMO	69.4	-0.833
DPP em	1	2.412	0.872	HOMO/LUMO	93.7	-0.968
	2	2.989	0.000	HOMO-1/LUMO	91.5	0.956
	3	3.172	0.000	HOMO/LUMO+1	86.4	0.929
	4	3.500	0.006	HOMO-6/LUMO	50.7	0.712
	5	3.844	0.000	HOMO-3/LUMO	71.9	-0.848
CAM-B3LYP	state	excitation energy [eV]	$f_{\text{osc}}$	transition	%	c
ADB abs	1	3.715	0.314	HOMO/LUMO	92.4	0.961
	2	4.091	0.001	HOMO/LUMO+3	46.3	-0.681
	3	4.109	0.000	HOMO/LUMO+1	95.5	-0.977
	4	4.137	0.002	HOMO/LUMO+2	95.5	0.977
	5	4.990	0.000	HOMO/LUMO+4	89.1	0.944
ADB em	1	3.077	0.531	HOMO/LUMO	94.3	-0.971
	2	3.892	0.002	HOMO/LUMO+3	48.0	0.693
	3	3.845	0.070	HOMO/LUMO+2	93.6	0.967
	4	3.816	0.000	HOMO/LUMO+1	95.2	-0.976
	5	4.645	0.000	HOMO/LUMO+4	82.9	-0.911
DPP abs	1	3.219	0.670	HOMO/LUMO	94.2	0.971
	2	3.495	0.000	HOMO-1/LUMO	90.0	0.949
	3	4.137	0.004	HOMO-6/LUMO	65.9	0.812
	4	4.245	0.000	HOMO/LUMO+1	91.8	0.958
	5	4.591	0.000	HOMO-3/LUMO	41.2	-0.642
DPP em	1	2.607	0.918	HOMO/LUMO	94.9	-0.974
	2	3.334	0.000	HOMO-1/LUMO	90.7	-0.952
	3	3.795	0.000	HOMO/LUMO+1	92.6	0.963
	4	4.003	0.008	HOMO-6/LUMO	64.7	-0.805
	5	4.328	0.000	HOMO-3/LUMO	60.4	0.777

Table 23 lists the energies and oscillator strengths of the first five singlet excitation of the ADB monomer calculated with PBE0//PBE, TZVP//TZVP, TZVP//SVP and SVP//SVP as used in *Benchmarking of the basis set* in chapter 6.2.7. The abbreviation reads as follows: excited state calculation//geometry optimization, where PBE0 is PBE0/def2-TZVP, PBE is PBE/def2-TZVP, TZVP is PBE0/def2-TZVP and SVP is PBE0/def2-SVP.

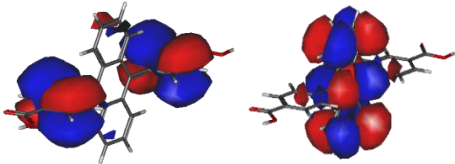
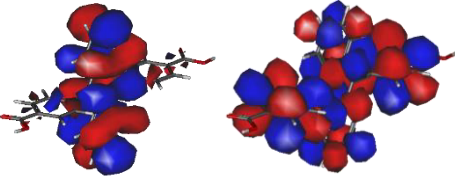
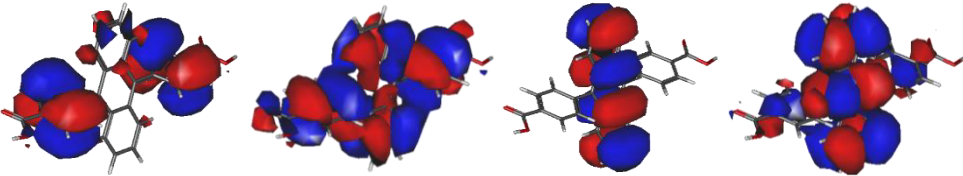
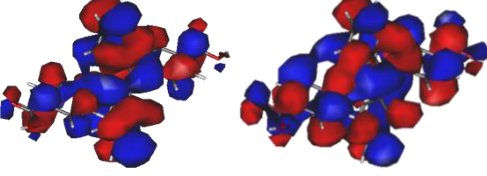
Table 23: First five singlets of absorption of ADB monomer calculated with PBE0//PBE, TZVP//TZVP, TZVP//SVP and SVP//SVP as used in benchmarking of the basis set.

PBE	state	excitation energy [eV]	$f_{osc}$	transition	%	c
PBE0//PBE	1	3.230	0.374	HOMO/LUMO	90.2	0.950
	2	3.516	0.000	HOMO/LUMO+1	96.1	-0.981
	3	3.566	0.000	HOMO/LUMO+2	92.8	0.963
	4	3.792	0.000	HOMO/LUMO+3	49.7	0.705
	5	4.296	0.000	HOMO/LUMO+4	90.6	0.952
PBE0	state	excitation energy [eV]	$f_{osc}$	transition	%	c
TZVP//TZVP	1	3.375	0.314	HOMO/LUMO	91.7	0.958
	2	3.650	0.000	HOMO/LUMO+1	97.3	-0.986
	3	3.687	0.000	HOMO/LUMO+2	96.3	-0.981
	4	3.870	0.001	HOMO/LUMO+3	50.3	-0.709
	5	4.386	0.000	HOMO/LUMO+4	91.4	-0.956
TZVP//SVP	1	3.353	0.296	HOMO/LUMO	92.1	0.960
	2	3.607	0.000	HOMO/LUMO+1	98.1	0.991
	3	3.639	0.000	HOMO/LUMO+2	97.6	0.988
	4	3.830	0.001	HOMO/LUMO+3	50.5	-0.710
	5	4.343	0.000	HOMO/LUMO+4	90.5	-0.951
SVP//SVP	1	3.436	0.320	HOMO/LUMO	91.4	0.956
	2	3.683	0.000	HOMO/LUMO+1	97.4	0.987
	3	3.710	0.000	HOMO/LUMO+2	96.6	0.983
	4	3.891	0.000	HOMO/LUMO+3	48.8	-0.699
	5	4.474	0.000	HOMO/LUMO+4	77.3	-0.879

## A1.2 Molecular excitation properties

Table 24 lists the energies and oscillator strengths of the singlets, which contribute most to the excitation spectra presented in the chapter “Absorption and emission of ADB molecule”. The involved molecular orbitals are shown as well.

Table 24: Prominent singlets of absorption and emission with oscillator strength  $f_{osc} > 0,01$  of both conformers of ADB and molecular orbitals (Gabedit, ISO=0.01 e<sup>2</sup>/Å<sup>3</sup>); PBE0/def2-TZVP.

	state	excitation energy [eV]	$f_{osc}$	transition	%	c	
abs.	1	3.365	0.255	HOMO/LUMO	90.0	0.949	
	2	3.528	0.000	HOMO/LUMO+1	99.1	-0.996	
	3	3.564	0.003	HOMO/LUMO+2	95.3	-0.976	
	4	3.883	0.002	HOMO/LUMO+3	53.1	-0.729	
	5	4.209	0.000	HOMO/LUMO+4	93.0	-0.964	
	6	4.337	0.038	HOMO/LUMO+5	72.5	-0.852	
	10	4.545	0.016	HOMO-5/LUMO	88.7	-0.942	
							
							
cis	em.	1	2.739	0.538	HOMO / LUMO	92.8	0.963
		8	4.275	0.234	HOMO-3 / LUMO	94.8	-0.974
		10	4.409	0.022	HOMO-5 / LUMO	76.7	-0.876
		13	4.574	0.264	HOMO-1 / LUMO+2	52.2	-0.723
							
							

<i>abs.</i>	1	3.347	0.250	HOMO/LUMO	87.8	0.937	
	2	3.546	0.009	HOMO/LUMO+1	92.0	0.959	
	3	3.554	0.000	HOMO/LUMO+2	98.6	0.993	
	4	3.882	0.002	HOMO/LUMO+3	53.0	-0.728	
	5	4.208	0.000	HOMO/LUMO+4	93.0	0.964	
	6	4.334	0.038	HOMO/LUMO+5	72.6	-0.852	
	9	4.474	0.014	HOMO-4/LUMO	98.0	-0.990	
	10	4.572	0.015	HOMO-5/LUMO	86.6	-0.931	
	<i>trans</i>						
<i>em.</i>	1	2.738	0.526	HOMO / LUMO	93.3	0.966	
	9	4.418	0.306	HOMO-4 / LUMO	95.0	-0.975	
	10	4.534	0,023	HOMO-5 / LUMO	83.0	-0.911	
	14	4.807	0,320	HOMO-1 / LUMO+2	46.7	-0.683	

### A1.3 Quinoid structure

Relaxation of the first excited state leads to a change in geometry away from the aromatic systems toward a quinoid-like structure. As shown in Figure 52 five bond lengths are chosen to distinguish between the  $S_0$  and  $S_1$  geometry. In the excited state geometry the bonds between the aromatic moieties (phenyl-anthracene) are expected to be shortened, as they get double-bond character.

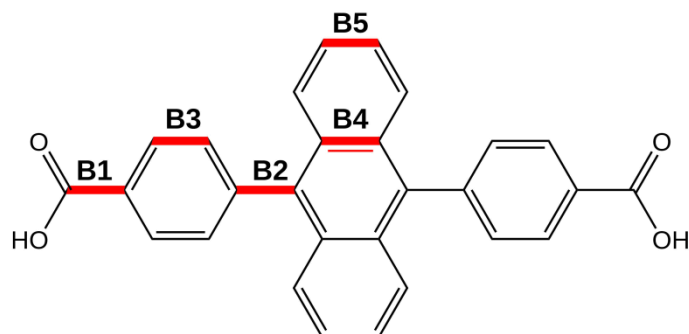


Figure 52: Skeletal formula of ADB with bonds B1-B5 shown in red; Figure 24 extended.

Table 25: Bond lengths of the cis- and trans-molecule compared to the cis-molecule in ground state (PBE0+D3/def2-TZVP) as well as the corresponding oligomers (PBE0+D3/def2-SVP) in  $S_1$  state compared to the monomer in ground state (PBE0+D3/def2-SVP); labelling of oligomers: according to Figure 33 from left to right.

molecules		Bond length [Å]				
		B1	B2	B3	B4	B5
cis $S_0$		1.479	1.485	1.383	1.436	1.416
cis $S_1$		1.469	1.462	1.376	1.431	1.388
trans $S_1$		1.469	1.460	1.378	1.434	1.390
oligomers		B1	B2	B3	B4	B5
monomer		1.511	1.508	1.396	1.450	1.420
trimer cis $S_1$	m0	1.497	1.497	1.394	1.451	1.400
	m1	1.520	1.506	1.397	1.449	1.400
	m2	1.514	1.510	1.394	1.452	1.418
trimer trans $S_1$	m0	1.509	1.510	1.396	1.452	1.418
	m1	1.499	1.490	1.393	1.454	1.401
	m2	1.521	1.500	1.395	1.450	1.398
tetramer cis $S_1$	m0	1.511	1.512	1.396	1.452	1.418
	m1	1.499	1.497	1.393	1.451	1.400
	m2	1.519	1.505	1.396	1.449	1.400
	m3	1.514	1.510	1.394	1.453	1.419



## A2 FRET Code

### A2.1 The input file

The script for calculating the Coulomb coupling is written in Fortran 95. This section describes a typical input of the program and provides further details about its variables and optional features. The input has to be named “inputfret” and should be constructed like the example in Figure 53. In general keywords start with “%”, whereas comment lines must be marked with “#”. Input variables must be preceded by an equal sign, “=”. The file has to end with the word “end” in the last line.

```
%file donor=em.cube acceptor=abs.cube
# parallel displacement
%vect x=0.0000 y=0.0000 z=5.81
%orig mon1=51 mon2=51
%dist dist=6.0
%dido x=-1.42679 y=-1.41804 z=-0.00098
%diac x=-1.42679 y=-1.41804 z=-0.00098
# more options
%rate overlap=1234 ref=1.24
# default treshold is 0.00001, optional
%tres treshold=0.001
end
```

Figure 53: Example of an input file for the calculation of the Coulomb coupling.

The input file consists of six mandatory keywords and two optional keywords. The mandatory keywords are:

**%file :** This line must contain the names of the cube-files of the donor and the acceptor in this order, which should be used for the calculation.

**%orig :** This line must contain the number of an atom of the donor and one of the acceptor in this order. Counting starts with 1. The donor molecule will be translated in such a way that the given atom will sit in the coordinate origin. The acceptor molecule will first be translated so that the given atom will sit in the coordinate origin, in the second step the molecule will be translated along the given vector at %vec with the distance of %dist.

**%vect :** This line must contain three coordinates of a vector in order of x, y and z. The acceptor will be translated along this vector.

%dist : This line must contain the translation distance of the acceptor molecule in Ångström.

%dido : This line must contain the dipole moment of the donor according to the quantumchemical calculation in order of x, y and z in atomic units.

%diac : This file must contain the dipole moment of the acceptor according to the quantumchemical calculation in order of x, y and z in atomic units.

The optional keywords are:

%tres : This line may contain a threshold, which is used to specify the amount of considered TDC-elements. The default value is set to  $10^{-5}$ . For detailed information see below.

%rate : This line may contain the spectral overlap and the refractive index of the medium. If this keyword is stated, the code computes the energy transfer rate according to Eq.11. The spectral overlap in cm may best be obtained through an experiment.

The output is saved in a file called "info.txt". To check for the meaningfulness of the molecular cluster, its structure is written in a file called "komplex.xyz" and can be viewed with any conventional visualization program of molecular structure. Already existing files will be overwritten.

Up to now the program can handle structures containing the first 86 elements of the periodic table. The atomic masses are taken from ref.67.

## A2.2 Convergence testing

Required for the TDC-method is that the volumetric data of the transition density is stored in the Gaussian Cube File Format. This file format consists of a three-dimensional grid dividing the molecule into cuboidal elements and assigning a proper value of the transition density to each segment. To get a better idea Figure 54 shows a schematic representation of such a Cube File.



Figure 54: Schematic representation of a Cube File; each small cube represents one (x,y,z)-element.

Taking the accuracy of the wavefunctions aside, the TDC-method is exact when taking the exact transition densities, which would correspond to the multiplication over all infinitesimal small volumetric elements according to Eq.11. In practice this is not feasible as it would be devastatingly time consuming. Therefore, two obviously adjustable parameters arise, which influence the quality and practicality of the calculation: On the one hand, the grid size is responsible for the correct description of the transition density. On the other hand, the amount of cube elements, which are considered for multiplication, determines the correct numerical value of the coupling. To find a compromise between the accuracy of the data and the time consumed, convergence tests were done on both parameters.

### Grid size

The transition dipole moment is a convenient value for converging the grid size as it is already given in the output file of a TDDFT-calculation and can be calculated from the Cube File via Eq.5. Converging the grid size ultimately means changing the edge lengths of the cuboidal elements. Figure 55 shows the transition dipoles of a monomer unit and of anthracene with seven different grid sizes. As can be seen from the figure a grid size bigger than 80 has negligible improvement on the accuracy of the value. Therefore, the transition density cube files in this thesis were constructed with a grid size of 80.

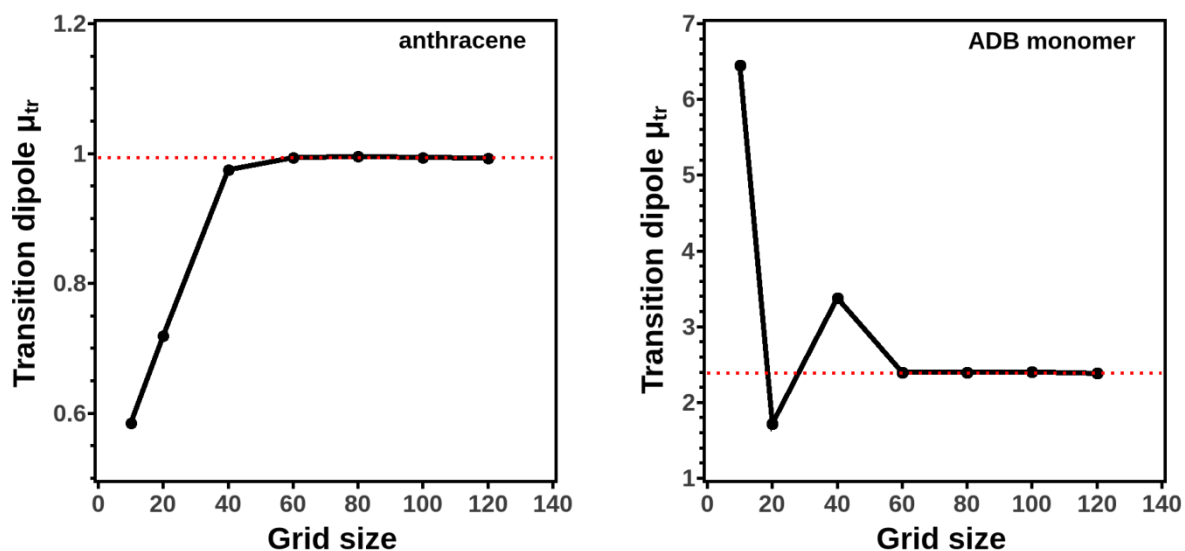


Figure 55: Transition dipole moment of anthracene (left) and of a monomer unit (right) in dependence of the grid size. The dotted red line indicates the transition dipole according to the ORCA output.

## Threshold

To limit the amount of cube elements used in the calculation, a threshold criterion was introduced inspired by the FRETYY-program by ref.68. For this, the absolute value of each cube element in a Cube file is compared to the biggest absolute value of this Cube file according to Eq.34. Then it is either considered if within a certain threshold, or it is set to zero.

$$|M_i| \geq |M_{max}| * threshold \quad \text{Eq.34}$$

To determine the influence of the threshold on the Coulombic coupling of different systems, the coupling between two monomer units as well as between two anthracenes was calculated using seven different thresholds. As can be seen in Figure 56, the threshold depends on the size of the system. The default value of  $10^{-5}$  is adapted to bigger systems, but it has to be noted that for smaller systems a smaller threshold could be time-saving.

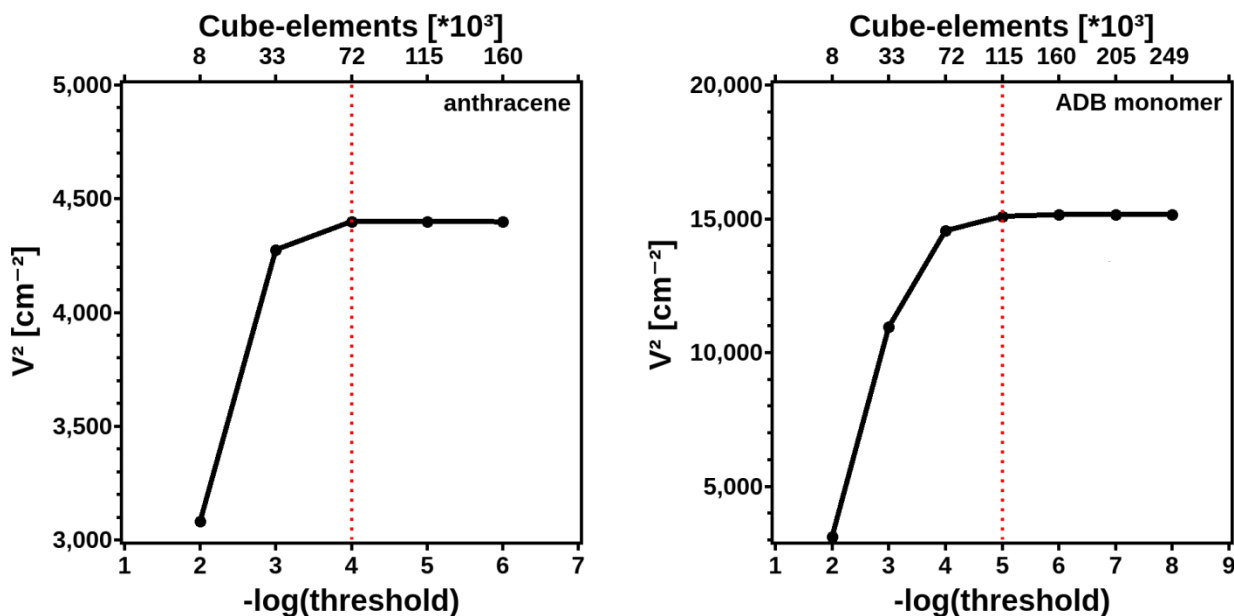


Figure 56: Coulombic coupling between two anthracenes (left) as well as between two monomer units (right) with different thresholds applying the TDC-method. The red line indicates the threshold chosen for the calculations.

A general hint towards the numerical accuracy of the transition density is the integration over all cube elements, as this integral must be zero by definition. In the present study the integrals of all cube files were in the order of  $10^{-3}$  or smaller.

### A2.3 TDC vs. IDA

The Dipole-Dipole model as described in *Förster Theory* (vide supra) would be a much faster method to calculate the Coulombic coupling. However, the ideal dipole approximation (IDA) holds only true if the distance between the involved molecules is much greater than their sizes. The specific geometry of the present MOF causes difficulties in the application of this method. At small distances like the inter-sheet distance the molecular transition moments no longer appear point-sized and the definition of  $R_{DA}$  is no longer justified. The breakdown of the Dipole-Dipole approximation can be seen in Figure 57, where the Coulombic coupling between two parallel ADB monomer units with increasing distance is shown. With increasing distance both methods compute the same coupling, but at the distance in the MOF (5 – 20 Å), traditional Förster theory (IDA) leads to a strong overestimation of the coupling. According to literature, this over- or underestimation of the coupling due to IDA is dependent on the arrangement of the chromophores, but is always significant as soon as the size of the chromophores is close to the distance between them.<sup>69</sup>

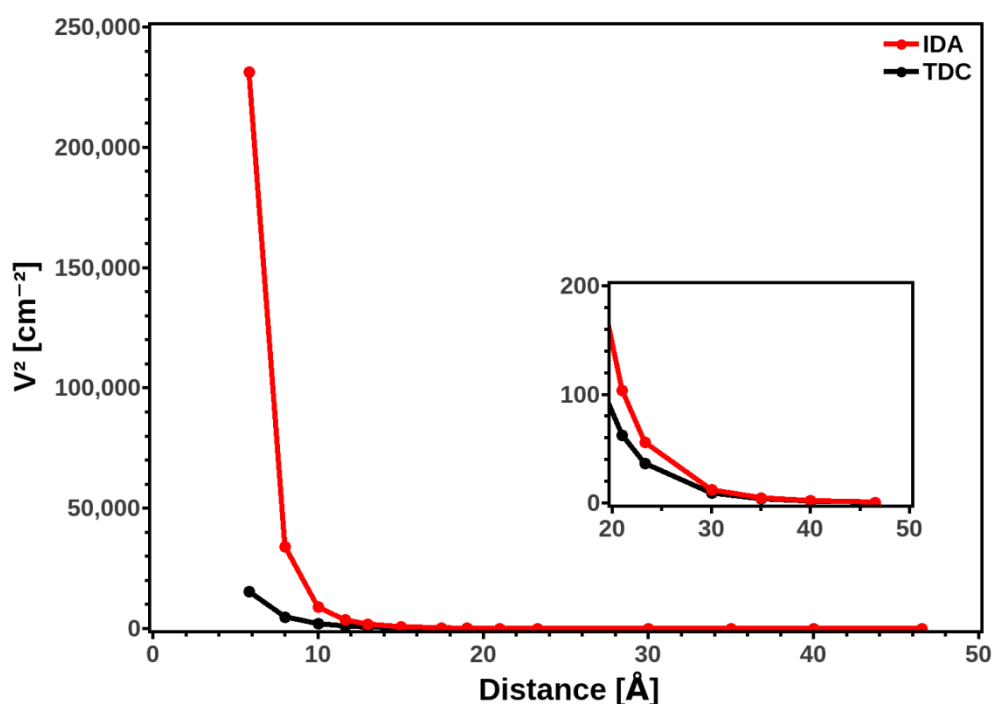


Figure 57: Calculated Coulombic coupling between two parallel monomer units with increasing distance applying the TDC-method and the Dipole-Dipole model. The inset shows the functions at bigger distances.

### A3 FHI-Aims basis set

Table 26 lists the basis functions that build up the *tight* basis set of FHI-Aims used in the calculations of the Cu-MOF and Zn-MOF, respectively. The abbreviations read as follows:  $X(n,l,z)$ , where  $X$  can either be H for hydrogen-like type function or I for ionic-like type function,  $n$  is the main quantum number,  $l$  is the angular momentum quantum number and  $z$  is an effective nuclear charge.

Table 26: Basis functions that build up the tight basis set of FHI-Aims used in the periodic calculations.

	H	C	O	Cu	Zn
Minimal	1s	[He] 2s2p	[He] 2s2p	[Ar] 3d4s	[Ar] 3d4s
Tier 1	H(2s,2.1)	H(2p,1.7)	H(2p,1.8)	I(4p,auto)	H(2p,1.7)
	H(2p,3.5)	H(3d,6)	H(3d,7.6)	H(4f,7.4)	H(3s,2.9)
		H(2s,4.9)	H(3s,6.4)	H(3s,2.6)	H(4p,5.4)
			H(3d,5)	H(4f,7.8)	
			H(5g,10.4)	H(3d,4.5)	
Tier 2	H(1s,0.85)	H(4f,9.8)	H(4f,11.6)		
	H(2p,3.7)	H(3p,5.2)	H(3p,6.2)		
	H(2s,1.2)	H(3s,4.3)	H(3d,5.6)	-	-
	H(3d,7)	H(5g,14.4)	H(5g,17.6)		
		H(3d,6.2)	H(1s,0.75)		

## Bibliography

### MOF:

- [1] H. Furukawa, K.E. Cordova, M. O’Keeffe, O.M. Yaghi. The chemistry and applications of metal-organic frameworks. *Science* **2013**, 341(6149), 1230444.
- [2] M.J. Kalmutzki, N. Hanikel, O.M. Yaghi. Secondary building units as the turning point in the development of reticular chemistry of MOFs. *Sci. Adv.* **2018**, 4(10).
- [3] S.T. Meek, J.A. Greathouse, M.D. Allendorf. Metal-Organic Frameworks: A Rapidly Growing Class of Versatile Nanoporous Materials. *Adv. Mater.* **2011**, 23, 249-267.
- [4] M. Eddaoudi, J. Kim, N. Rosi, D. Vodak, J. Wachter, M. O’Keeffe, O.M. Yaghi. Systematic design of pore size and functionality in isorecticular MOFs and their application in methane storage. *Science* **2002**, 295(5554), 496-472.
- [5] J.L.C. Rowsell, O.M. Yaghi. Effects of Functionalization, Catenation, and Variation of the Metal Oxide and Organic Linking Units on the Low-Pressure Hydrogen Adsorption Properties of Metal-Organic Frameworks. *J. Am. Chem. Soc.* **2006**, 128(4), 1304-1315.
- [6] P. Horcajada, C. Serre, M. Vallet-Regí, M. Sebhan, F. Taulelle, G. Férey. Metal-organic frameworks as efficient materials for drug delivery. *Angew. Chem. Int. Ed.* **2006**, 45(36), 5974-5978.
- [7] I. Imaz, M. Rubio-Martínez, L. García-Fernández, F. García, D. Ruiz-Molina, J. Hernando, V. Puentes, D. Maspoch. Coordination polymer particles as potential drug delivery system. *Chem. Commun.* **2010**, 46, 4737-4739.
- [8] U. Ravon, M. Savonnet, S. Aguado, M.E. Domine, E. Janneau, D. Farrusseng. Engineering of coordination polymers for shape selective alkylation of large aromatics and the role of defects. *Microporous Mesoporous Mater.* **2010**, 129, 319-329.
- [9] W. Kleist, F. Jutz, M. Maciejewski, A. Baiker. Mixed-Linker Metal-Organic Frameworks as Catalysts for the Synthesis of Propylene Carbonate from Propylene Oxide and CO<sub>2</sub>. *Eur. J. Inorg. Chem.* **2009**, 3552-3561.
- [10] H.-J. Son, S. Jin, S. Patwardhan, S.J. Wezenberg, N.C. Jeong, M. So, C.E. Wilmer, A.A. Sarjeant, G.C. Schatz, R.Q. Snurr, O.K. Farha, G.P. Wiederrecht, J.T. Hupp. Light-Harvesting and Ultrafast Energy Migration in Protoporphyrin-Based Metal-Organic Frameworks. *J. Am. Chem. Soc.* **2013**, 135, 862-869.
- [11] T. Zhang, W. Lin; Metal-organic frameworks for artificial photosynthesis and photocatalysis. *Chem. Soc. Rev.* **2014**, 43, 5982-5993.
- [12] J. Liu, W. Zhou, J. Liu, I. Howard, G. Kilbarda, S. Schlabach, D. Coupry, M. Addicoat, S. Yoneda, Y. Tsutsui, T. Sakurai, S. Seki, Z. Wang, P. Lindemann, E. Redel, T. Heine, C. Wöll. Photoinduced Charge-Carrier Generation in Epitaxial MOF Thin Films: High Efficiency as a Result of an Indirect Electronic Band Gap? *Angew. Chem. Int. Ed.* **2015**, 54, 7441-7445.
- [13] F.P. Doty, C.A. Bauer, A.J. Skulan, P.G. Grant, M.D. Allendorf. Scintillating Metal-Organic Frameworks: A New Class of Radiation Detection Materials. *Adv. Mater.* **2009**, 21, 95-101.
- [14] A. Lan, K. Li, H. Wu, D.H. Olson, T.J. Emge, W. Ki, M. Hong, J. Li. A Luminescent Microporous Metal-Organic Framework for the Fast and Reversible Detection of High Explosives. *Angew. Chem. Int. Ed.* **2009**, 48, 2334-2338.

- [15] S. Yuan, L. Feng, K. Wang, J. Pang, M. Bosch, C. Lollar, Y. Sun, J. Qin, X. Yang, P. Zhang, Q. Wang, L. Zou, Y. Zhang, L. Zhang, Y. Fang, J. Li, H.-C. Zhou. Stable Metal-Organic Frameworks: Design, Synthesis, and Applications. *Adv. Mater.* **2018**, 30, 1704303.
- [16] D.J. Tranchemontagne, J.L. Mendoza-Cortés, M. O’Keeffe, O.M. Yaghi. Secondary building units, nets and bonding in the chemistry of metal-organic frameworks. *Chem. Soc. Rev.* **2009**, 38, 1257-1283.
- [17] M.K. Bhunia, J.T. Hughes, J.C. Fettinger, A. Navrotsky. Thermochemistry of paddle wheel MOFs: Cu-HKUST-1 and Zn-HKUST-1. *Langmuir* **2013**, 29, 8140-8145.
- [18] J.J. Zuckerman. Crystal field splitting diagrams. *J. Chem. Educ.* **1965**, 42(6), 315-317.
- [19] B. Morosin. The crystal structures of copper tetrammine complexes. A.  $\text{Cu}(\text{NH}_3)_4\text{SO}_2 \cdot \text{H}_2\text{O}$  and  $\text{Cu}(\text{NH}_3)_4\text{SeO}_4$ . *Acta Crystallogr.* **1969**, B25, 19-30.
- [20] C.G. Carson, G. Brunello, S.G. Lee, S.S. Jang, R.A. Gerhardt, R. Tannenbaum. Structure Solution from Powder Diffraction of Copper 1,4-Benzenedicarboxylate. *Eur. J. Inorg. Chem.* **2014**, 2140-2145.
- [21] J. Liu, B. Lukose, O. Shekhah, H.K. Arslan, P. Weidler, H. Gliemann, S. Bräse, S. Grosjean, A. Godt, X. Feng, K. Müllen, I.-B. Magdau, T. Heine, C. Wöll. A novel series of isorecticular metal organic frameworks: realizing metastable structures by liquid phase epitaxy. *Sci. Rep.* **2012**, 2(921).
- [22] H. Walch, T. Leoni, O. Guillermet, V. Langlais, A. Scheuermann, J. Bonvoisin, S. Gauthier. Electromechanical switching behaviour of individual molecular complexes of Cu and Ni on NaCl-covered Cu(111) and Ag(111). *Phys. Rev. B* **2012**, 86(7), 075423.
- [23] S. Bureekaew, S. Amirjalayer, R. Schmid. Orbital directing effects in copper and zinc based paddle-wheel metal organic frameworks: the origin of flexibility. *J. Mater. Chem* **2012**, 22, 10249-10254.
- [24] P.J. Hay, J.C. Thibeault, R. Hoffmann. Orbital interactions in metal dimer complexes. *J. Am. Chem. Soc.* **1975**, 97, 4884-4899.
- [25] O. Shekhah, J. Liu, R.A. Fischer, C. Wöll. MOF thin films: existing and future applications. *Chem. Soc. Rev.* **2011**, 40, 1081-1106.
- [26] O. Shekhah, H. Wang, S. Kowarik, F. Schreiber, M. Paulus, M. Tolan, C. Sternemann, F. Evers, D. Zacher, R.A. Fischer, C. Wöll. Step-by-Step Route for the Synthesis of Metal-Organic Frameworks. *J. Am. Chem. Soc.* **2007**, 129, 15118-15119.

### **FRET:**

- [27] G.D. Scholes. Long-range resonance energy transfer in molecular systems. *Annu. Rev. Phys. Chem.* **2003**, 54, 57-87.
- [28] V. May, O. Kühn; *Charge and Energy Transfer Dynamics in Molecular Systems*, Wiley-vch: Weinheim, **2011**.
- [29] R. van Grondelle. Excitation energy transfer, trapping and annihilation in photosynthetic systems. *Biochem. Biophys. Acta* **1985**, 811, 147-195.
- [30] V. Raicu, D.R. Singh. FRET Spectrometry: A New Tool for the Determination of Protein Quaternary Structure in Living Cells. *Biophys. J.* **2013**, 105, 1937-1945.
- [31] J. Ma, I.S. Yanez-Orozco, S.R. Adariani, D. Dolino, V. Jayaraman, H. Sanabria. High Precision FRET at Single-molecule Level for Biomolecule Structure Determination. *J. Vis. Exp.* **2017**, 123, 55623.



- [32] H.H. Pham, J.P.S. Farinha, M.A. Winnik. Cross-Linking, Miscibility, and Interface Structure in Blends of Poly(2-ethylhexyl methacrylate) Copolymers. An Energy Transfer Study. *Macromolecules* **2000**, 33, 5850-5862.
- [33] P. Rajdev, S. Ghosh. Fluorescence Resonance Energy Transfer (FRET): A Powerful Tool for Probing Amphiphilic Polymer Aggregates and Supramolecular Polymers. *J. Phys. Chem. B* **2019**, 123, 327-342.
- [34] T. Förster. Zwischenmolekulare Energiewanderung und Fluoreszenz. *Ann. Physik* **1948**, 2, 55-75.
- [35] B.P. Krueger, G.D. Scholes, G.R. Fleming. Calculation of Couplings and Energy-Transfer Pathways between the Pigments of LH2 by the ab Initio Transition Density Cube Method. *J. Phys. Chem.* **1998**, 102, 5378-5386.

### **DFT:**

- [36] A. Szabo, N.S. Ostlund; *Modern Quantum Chemistry – Introduction to Advanced Electronic Structure Theory*, Dover Publications: Mineola, **1996**.
- [37] I.N. Levine; *Quantum Chemistry*, Prentice-Hall: Upper Saddle River, **2000**.
- [38] C.J. Cramer; *Essentials of computational chemistry*, John Wiley & Sons: Chichester, **2004**.
- [39] P. Hohenberg, W. Kohn. Inhomogeneous Electron Gas. *Phys. Rev.* **1964**, 136, B864-B871.
- [40] W. Kohn, L.J. Sham. Self-Consistent Equations Including Exchange and Correlation Effects. *Phys. Rev.* **1965**, 140, A1133-A1138.
- [41] J.P. Perdew, K. Burke, and M. Ernzerhof. Generalized Gradient Approximation Made Simple. *Phys. Rev. Lett.* **1996**, 77, 3865-3868.
- [42] G.I. Csonka, J.P. Perdew, A. Ruzsinszky, P.H.T. Philipsen, S. Lebègue, J. Paier, O.A. Vydrov, J.G. Ángyán. Assessing the performance of recent density functionals for bulk solids. *Phys. Rev. B* **2009**, 79(155107).
- [43] M. Ernzerhof, G.E. Scuseria. Assessment of the Perdew-Burke-Ernzerhof exchange-correlation functional. *J. Chem. Phys.* **1999**, 110(11), 5029-5036.
- [44] C. Adamo, V. Barone. Toward reliable density functional methods without adjustable parameters: The PBE0 model. *J. Chem. Phys.* **1999**, 110, 6158-6170.
- [45] A.D. Laurent, D. Jacquemin. TD-DFT benchmarks: A review. *Int. J. Quantum. Chem.* **2013**, 113, 2019-2039.
- [46] E. Runge, E.K.U. Gross. Density-Functional Theory for Time-Dependent Systems. *Phys. Rev. Lett.* **1984**, 52(12), 997-1000.
- [47] F. Weigend, R. Ahlrichs. Balanced basis set of split valence, triple zeta valence and quadruple zeta valence quality for H to Rn: Design and assessment of accuracy. *Phys. Chem. Chem. Phys.* **2005**, 7, 3297-3305.
- [48] P.Hobza, J. Sponer, T.J. Reschel. Density functional theory and molecular clusters. *Comput. Chem.* **1995**, 11, 1315-1325.
- [49] S. Kristyan, P. Pulay. Can (semi)local density functional theory account for the London dispersion forces? *Chem. Phys. Lett.* **1994**, 229(3), 175-180.
- [50] A. Tkatchenko, M. Scheffler. Accurate Molecular Van Der Waals Interactions from Ground-State Electron Density and Free-Atom Reference Data. *Phys. Rev. Lett.* **2009**, 102, 073005.

[51] S. Grimme, J. Antony, S. Ehrlich, H. Krieg. A consistent and accurate *ab initio* parametrization of density functional dispersion correction (DFT-D) for the 94 elements H-Pu. *J.Chem.Phys.* **2010**, 132, 154104.

### **Cu-MOF:**

[52] P. Falcaro, K. Okada, T. Hara, K. Ikigaki, Y. Tokudome, A.W. Thornton, A.J. Hill, T. Williams, C. Doonan, M. Takahashi. Centimetre-scale micropore alignment in oriented polycrystalline metal-organic framework films via heteroepitaxial growth. *Nat. Mater.* **2017**, 16, 342-349.

[53] K.A.H. Alzahrani, R.J. Deeth. Density functional calculations reveal a flexible version of the copper paddlewheel unit: implications for metal organic frameworks. *Dalton Trans.* **2016**, 45, 11944-11948.

[54] M. Tafipolsky, S. Amirjalayer, R. Schmid. First-Principles-Derived Force Field for Copper Paddle-Wheel-Based Metal-Organic Frameworks. *J. Phys. Chem. C* **2010**, 114, 14402–14409.

[55] A. Elmali. The Magnetic Super-Exchange Coupling in Copper(II) Acetate Monohydrate and a Redetermination of the Crystal Structure. *Turk. J. Phys.* **2000**, 24, 667.

[56] H.R. Oswald, A. Reller, H.W. Schmalke, E. Dubler. Structure of copper(II) hydroxide, Cu(OH)<sub>2</sub>. *Acta Crystallogr. Sect. C Cryst. Struct. Commun.* **1990**, 46, 2279-2284.

### **Zn-MOF:**

[57] R. Haldar, M. Jakoby, A. Mazel, Q. Zhang, A. Welle, T. Mohamed, P. Krolla, W. Wenzel, S. Diring, F. Odobel, B.S. Richards, I.A. Howard, C. Wöll. Anisotropic energy transfer in crystalline chromophore assemblies. *Nat. Commun.* **2018**, 9(4332).

[58] F. Neese. The ORCA program system. *Wiley Interdiscip. Rev.: Comput. Mol. Sci.* **2012**, 2, 73–78.

[59] T. Yanai, D.P. Tew, N.C. Handy. A new hybrid exchange-correlation functional using the Coulomb-attenuating method (CAM-B3LYP). *Chem. Phys. Lett.* **2004**, 393, 51-57.

[60] A.V. Marenich, C.J. Cramer, D.G. Truhlar. Universal solvation model based on solute electron density and on a continuum model of the solvent defined by the bulk dielectric constant and atomic surface tensions. *J. Phys. Chem. B* **2009**, 113, 6378-6396.

[61] V. Blum, R. Gehrke, F. Hanke, P. Havu, V Havu, X. Ren, K. Reuter, and M. Scheffler. *Ab initio* molecular simulations with numeric atom-centered orbitals. *Comput. Phys. Commun.* **2009**, 180, 2175-2196.

[62] E. Juaristi; *Introduction to Stereochemistry and Conformational Analysis*, Wiley: New York, **1991**.

[63] F.J. Lederer, F.F. Graupner, B. Maerz, M. Braun, W. Zinth. Excimer formation in 9,10-dichloroanthracene – Solutions and crystals. *Chem. Phys.* **2014**, 428, 82-89.

[64] M. Sugino, Y. Araki, K. Hatanaka, I. Hisaki, M. Miyata, N. Tohnai. Elucidation of Anthracene Arrangement for Excimer Emission at Ambient Conditions. *Cryst. Growth Des.* **2013**, 13, 4986-4992.

[65] W. Heringer, A. Görling. Failure of time-dependent density functional methods for excitations in spatially separated systems. *Chem. Phys. Lett.* **2006**, 419, 557-562.

[66] J.L. Brédas, J.P. Calbert, D.A. da Silva Filho, J. Cornil; Organic semiconductors: A theoretical characterization of the basic parameters governing charge transport; *Proc. Natl. Acad. Sci. U S A* **2002**, 99(9), 5804-5809.

**Appendix:**

- [67] J. Meija, T.B. Coplen, M. Berglund, W.A. Brand, P. De Bièvre, M. Gröning, N.E. Holden, J. Irrgeher, R.D. Loss, T. Walczyk, T. Prohaska. Atomic weights of the elements 2013 (IUPAC Technical Report). *Pure Appl. Chem.* **2016**, 88(3), 265-291.
- [68] I. Tosi, M.S. Centellas, E. Campioli, A. Iagatti, A. Lapini, C. Sissa, L. Baldini, C. Cappelli, M. Di Donato, F. Sansone, F. Santoro, F. Terenziani. Excitation Dynamics in Hetero-bichromophoric Calixarene Systems. *ChemPhysChem* **2016**, 17, 1686-1706.
- [69] H. Wiesenhofer, D. Beljonne, G.D. Scholes, E. Hennebicq, J-L. Brédas, E. Zojer. Limitations of the Förster Description of Singlet Exciton Migration: The Illustrative Example of Energy Transfer to Ketonic Defects in Ladder-type Poly(*para*-phenylenes). *Adv. Funct. Mater.* **2005**, 15, 155-160.